A Theoretical Study of Metal-Organic Frameworks

SUBMITTED TO THE UNIVERSITY OF CAPE TOWN

In fulfilment of the requirements for the degree of

MASTER OF SCIENCE

By

Reabetswe Robin Zwane (DBXREA001)

Supervisor: Gerhard Venter; Co-supervisor: Clive Oliver; Co-supervisor: Karl Wilkinson (posthumous)

November 2018

Abstract

Among the options for carbon sequestration, the development of CO_2 capture materials has gained momentum over the past two decades. The design and construction of chemical and physical absorbents for the capture of CO_2 and clean energy storage are a crucial technology for a sustainable low-carbon future. Metal-organic frameworks (MOFs) provide a new vision for the adsorption of molecules on solid surfaces. The interest in MOFs is owed to their ultrahigh porosity, high surface areas and tuneable pore sizes and shapes.

The main objective of this thesis was to adopt a rational predictive capacity used in MOF design to control properties such as framework porosity and flexibility on a molecular scale. The *in-silico* studies were carried out by using *ab initio* quantum mechanical approaches such as density functional theory and perturbation theory. In addition, semi-classical methods like the Grand Canonical Monte Carlo (GCMC) approach was also used. A structural motif called *vicinal* fluorination was adopted to study MOF linkers in isolation and in a framework. An extensive conformational study, in various solvents, was carried out to investigate the effect of *vicinal* fluorination on the isolated MOF linkers and therefore elucidate their conformational stability. The effect of fluorination on adsorption isotherms was also investigated. Moreover, various fluorination patterns were explored. Adsorption isotherms of a non-fluorinated copper-based MOF based on experimental work, and its various fluorinated analogues were predicted using the GCMC method.

It was found that *vicinal* fluorination is not dominant in controlling conformations of some MOF linkers. Rather, an interplay of interactions, including solute and steric interactions, influence the conformational stability on rotational profiles. However, *vicinal* fluorination was shown to control the flexibility of the linkers used in MOFs as it controls the force constants around the minima of rotational profiles of isolated MOF linkers. The study also highlighted the importance of the solvent on the relative energies of the linker conformations – this has a potential impact on the synthesis of MOFs. With the help of computational methods and validation from experimental data, the structural and sorption properties of the framework, upon fluorination, were shown to have consequences on the adsorption properties of the MOF. *Vicinally* fluorinated frameworks were shown to have higher uptakes at a low temperature and low pressures.

Acknowledgements

This thesis is a special dedication to the late Karl Wilkinson. His memory remains. May his soul continue to rest in peace.

First and above, I praise God for granting me the strength to come and go. This thesis appears in its current form due to the continued assistance and guidance of several people. I would therefore like to extend my sincerest gratitude and appreciation to them all. Gerhard Venter, my esteemed supervisor, I express my deepest thanks for your office door that remained open. Your patience and critical comments on my thesis did not go unnoticed. Clive Oliver, thank you for your continued support and willingness to help where you could. I would like to thank the members of the SCRU for their valuable support during the whole period of the project. Among others, I thank Monde Sinxi, Jess Nel and Chris Barnett. A special mention of Bernard Dippenaar, who assisted me with Materials Studio calculations and also offered critical comments on my work. Lastly, before we are scientists, we belong to a family and a community. A special thanks to family and close friends for their support. My husband, for your patience and care. My mom, for your continued effort of ensuring I am healthy, both mentally and physically.

Contents

List of abbreviations

CO_2	Carbon dioxide
CSP	Crystal Structure Prediction
DFT	Density functional theory
GCMC	Grand Canonical Monte Carlo
GHG	Greenhouse gas
H_2	Hydrogen gas
LDA	Localized Gradient Approximation
MC	Monte Carlo
MOFs	Metal-Organic Frameworks
MOPs	Metal-organic polyhedra
N_2	Nitrogen gas
NBO	Natural bond orbital
PES	Potential energy surface
PW	Planewave
QM	Quantum mechanics/mechanical
Q_{st}	Adsorption enthalpy
q_{st}	Isosteric heats of adsorption
Ref.	Reference
SAPT	Symmetry Adapted Perturbation Theory
SBUs	Secondary building units

SE	Schrödinger Equation
SMD	Solvation Model based on Density
vdW	van der Waals

1

Introduction

1.1 Problem statement and research motivation

The emission of carbon dioxide gas (CO_2) through anthropogenic activities is a global phenomenon. Moreover, CO_2 is the primary greenhouse gas emitted, followed by methane (CH_4). In 2016, the global carbon budget reported that despite a three-year long intentional reduction of fossil fuel carbon emissions into the atmosphere, South Africa still has CO_2 emission that are above the global average per person.[1] The *World Resources Institute Climate Analysis Indicator Tool* (WRI CAT) has reported that greenhouse gas emissions in South Africa are dominated by the energy sector, accounting for 84% of greenhouse gas emissions by all the other sectors (agriculture, industrial processes, waste and land-use change and forestry).[2] In response, the shunning of the combustion of fossil fuels as an alternative approach for tackling the CO_2 emission problem has been a subject of intense research. Carbon capture and sequestration technologies continues to prevent large quantities of CO_2 being released into the atmosphere until there are significant modifications to the existing infrastructure in South Africa and the world at large.

Among the options for carbon sequestration, the development of CO_2 capture materials has gained momentum over the past twenty years. The design and synthesis of absorbents for the capture of CO_2 and the clean alternative storage for energy are a crucial technology for a sustainable low-carbon future. In the past decades, metal-organic frameworks (MOFs) have been extensively investigated as they provide a new vision for applications in gas storage, gas separation and molecular recognition, in heterogeneous catalysis and in biomedicine.[3–6] Early research of MOFs was largely focused on the use of MOFs for storage of gases such as methane and hydrogen.[7] Carbon sequestration is currently undergoing intense research due to its pressing motivations.

The interest that researchers have in MOFs for these 'classical' applications is owed to their ultrahigh porosity, high surface areas and tuneable pore sizes and shapes.[8] MOFs are typically constructed by a self-assembly process called reticular synthesis, which involves linking bridging organic ligands with metal ions.[9,10] MOFs show a superior performance over inorganic porous materials such as zeolites, or activated porous carbons, because of a vast number of organic linkers coupled with vacant or labile sites of metal ions affording them chemical versatility. In addition, they can be tailor-made by judiciously combining building blocks for desired applications. In principle, the judicious incorporation of accessible donor groups into the pore walls can dramatically affect the dynamic behaviour of the framework which includes adsorption capacity and selectivity.[11–13] Dynamic behaviour of MOFs can exhibit remarkable flexibility, an asset for designing responsive materials and propensity to undergo chemical changes that enable new functionality and properties to be introduced. Hence much effort is being made through the rational design of MOFs to understand the structure-property relationships.

1.2 Research objectives

The main aim of this thesis is to adopt the rational predictive capacity present in MOF design that allows the synthesis of novel frameworks with expected properties. The control of framework porosity and flexibility will be achieved from a molecular level. This will be achieved by ligand functionalization of MOF linkers, thereby biasing populations of isolated MOF linker conformations.

The first results chapter will focus on a comprehensive study of ligands of a new family of metal-organic frameworks which have had a degree of conformational flexibility introduced into them via *vicinal* or *n,n+1* fluorination. The role of *vicinal* fluorination on the conformational flexibility of MOF linkers will be investigated. The conformational control rests on fluorinated ligands having less flexibility than the C-C single bond equivalent of the non-fluorinated linker but more flexibility than the C-C double bond equivalent. The objectives include:

1) Study the effect of *n,n+1* fluorination on conformations adopted by the isolated MOF linkers, *in vacuo* and in solvent, using quantum mechanical calculations. Conformational analysis will be done on the linkers of 1,2-di(4-pyridyl)ethane, succinic acid, and their relevant analogues, as shown in Table (1-1). A more widely available and easily synthesized 2,2,3,3-succinic acid was included in the study. Moreover, its perfluorinated pattern of fluorine atoms adds to the fluorination patterns explored.
2) Investigate the conformational and dynamic behaviour of the isolated MOF linkers by the identification of minima and the calculation of rotational force constants of the linkers respectively.
3) Investigate the influence of the dielectric constant on potential energy surfaces of the isolated MOF linkers.
4) As a prerequisite study, benchmark various levels of theory to test their suitability for larger scale calculations. This study will be carried out using reference structures of butane and 2,3-difluorobutane.
5) Supplement the study of the effect of fluorination with Natural Bond Orbital (NBO) analysis, which allows the quantification of intramolecular interactions. Moreover, it allows the decomposition of energy into Lewis-type interactions, which include electrostatic and steric effects, and the non-Lewis interactions, which includes the energy of delocalization. The evaluation of the strength of hyperconjugation will particularly be looked into.[14] NBO analysis will therefore be performed on 2,3-difluorobutane and on the MOF linkers to gain more insight on the extent of the fluorine *gauche effect* on conformational control.

Table 1-1 *A table showing the isolated MOF linkers on which conformational analysis will be performed*

	Non-fluorinated MOF linker structure	**Fluorinated analogue** (***threo*** conformer)	**Fluorinated analogue** (***erythro*** conformer)
1,2-di(4-pyridyl)ethane	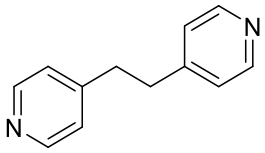	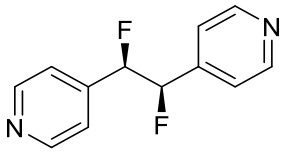	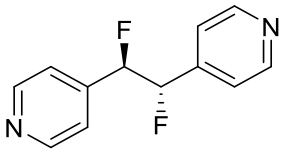
Succinic acid	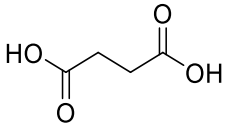	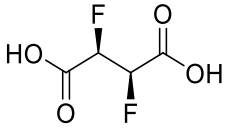	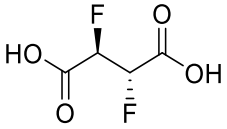

The aim of the second results chapter is to focus on the effect of fluorination on the adsorption properties of the frameworks containing these ligands. Furthermore, different fluorination patterns and their effect on the adsorption capacity will be explored. The main objectives of this chapter include:

1) Study the gas adsorption behaviour of an experimentally determined MOF containing at least one of the ligands in the previous study by using Grand Canonical Monte-Carlo (GCMC) simulation. Furthermore, carry out a comparative study of the adsorption behaviour of non-fluorinated and various fluorinated MOFs.
2) Explore the effect of different fluorination patterns on the adsorption behaviour of the resultant framework.
3) Comprehensively study the interactions of gas molecules with the fluorine atoms installed on the MOF surface channels. This will be done by calculating binding energies of isolated MOF linkers with a gas molecule. In addition, use an energy decomposition tool called SAPT to complement the studies.

1.3 Overview

The first chapter of this thesis is a literature review outlining topics in MOF literature that are relevant in this thesis. Most importantly, the computational characterization of porous materials is

discussed in length. Chapter two goes over the theoretical background of the computational approaches used in this *in-silico* study. More specifically, HF theory, DFT and planewave DFT is introduced. An extensive conformational analysis study is carried out by studying rotational energy profiles in chapter three. NBO analysis complements the conformational analysis by investigating the effect of *vicinal* or *n,n+1* fluorination. Chapter three is only concerned with the isolated MOF linkers (not part of a framework). Chapter four looks at the MOF linkers in the framework. More importantly, the fluorination of the linkers in the framework is addressed by studying the adsorption properties. Various fluorination patterns are also explored in this chapter. Adsorption isotherms are simulated using GCMC. The last chapter, chapter 5, concludes this thesis.

1.4 Metal-organic frameworks

Many solids that contain metal ions linked by organic molecular units have emerged over the past decades. This collection of materials has been variously termed metal-organic frameworks, coordination polymers and hierarchical zeolite analogues with overlapping descriptions of each. There exists literature that attempts to elucidate the definitions of each.[15,16] A coordination polymer is a compound that continuously extends in one, two or three dimensions via coordination bonds. A coordination polymer with an open framework that containing potential voids is referred to as a metal-organic framework.

A solid is referred to as a *metal-organic framework* if it possesses certain inherent attributes: classical covalent and coordinating bonds that provide robustness, structural units that can be modified by organic synthesis and high crystallinity. High crystallinity is an important attribute as it indicates high-quality MOFs, that can in turn establish structure-property relationships that rational design of MOFs aims for. MOF literature is an increasingly growing subject; currently, there are principles for designing and assembling target frameworks, collectively termed *reticular synthesis*. In this section, structure, properties and the rational design of MOFs is presented, outlining the MOF topics that are relevant in this work.

1.4.1 General properties

The properties of MOFs are characterized by robustness resulting from linking via strong bonds and considerable pore volume (50 % of the total volume and more). The freedom to vary the initial structural units provides the ability to tune parameters, such increasing pore diameters, decreasing density, as well as obtaining a specific surface area. The structure-property relationships of MOFs are derived from their structural features and the manipulation thereof. Understanding the structural features of the MOFs provides insight into their properties. Two building blocks are distinguished in MOFs: secondary building units (metal ions or clusters, Figure (1.1a)) and organic linkers (Figure (1.1b)) which are linked together via strong bonds to give 3D periodic porous structures.[17] Secondary building units can be combined into a framework structure through different linkers. It is these different combinations of structural units that lead to a myriad of MOFs with diverse structures, different symmetries and pore sizes, and hence, different characteristics. The pore size can be tuned by, for example, controlling the length of the carbon chain or the number of ring structures in it. Furthermore, unique chemical properties of the MOFs can be achieved by the incorporation of different substituents and functional groups in the linker.

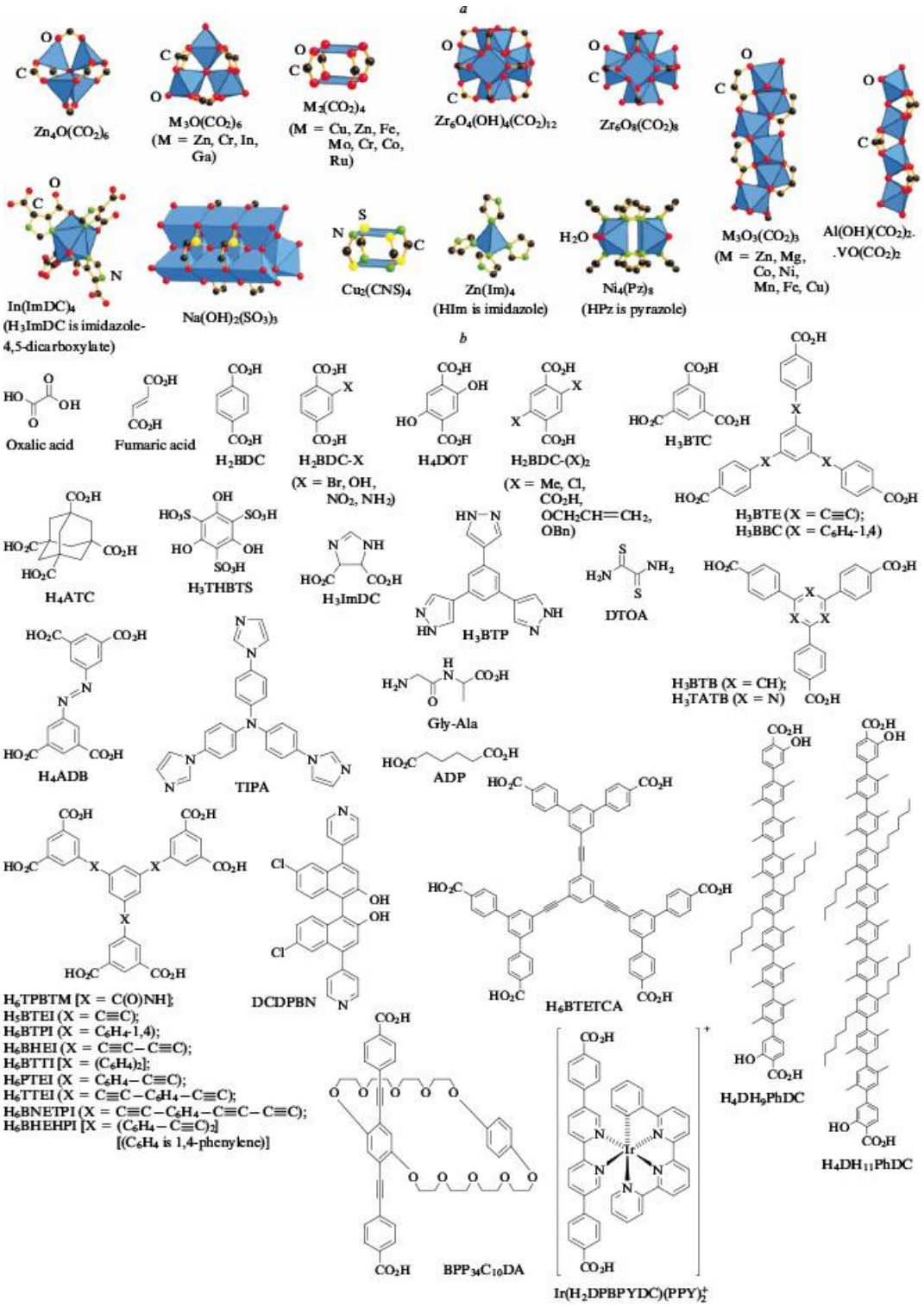

Figure 1.1 *Building blocks of metal-organic frameworks. (a) Metal clusters; (b) organic ligands with which linkers are formed. Figure reproduced from ref. 18.*

1.4.2 Synthesis of MOFs

The knowledge of possible topologies and functionalities of linkers, as well as the understanding of the smallest building blocks is often involved in the understanding of MOF synthesis efforts. A large variety of structures can be synthesized and could have applications in several fields related to porous materials. The term design has often been used regarding the synthesis of MOFs. This term is controversial when regarding synthesis of MOFs and the more stringent definition of design that implies creating, fashioning, executing or constructing per plan is not referred to.

The primary goal in the preparation of MOFs is to set up synthesis conditions that are favourable for the organic linkers used, that do not lead to the decomposition of the organic linker. The kinetics governing the crystallization must also be appropriate for the nucleation and growth of the desired phase. The most frequent method of MOF synthesis involves the mixing of separate metal salts and organic ligand solutions or addition of the solvent to a mixture of solid salt and ligand in a reaction vial. Solvent plays an important role in the thermodynamics and activation energy for a reaction. Solvothermal and hydrothermal crystallizations of dissolved reactants in suitable solvents are the general synthesis methodologies while alternative methods include the use of microwave, sonication and mechano-chemical and electrochemical synthesis methods. However, these alternative methods have issues with scalability, consistency, and cost that limits their use in practical applications.

1.5 The rational design of MOFs

The considerable variability of both the metal clusters and organic ligands available can lead to the design and synthesis of novel families. The inexhaustible amount of MOFs that could rationally be designed poses as a challenging task for researchers to find a suitable way of designing a framework with desired properties.[18,19] The aim of a material scientist is therefore to rationally design a novel framework that derives its properties from its structural units. Controlling the structure and functionality can be achieved from a molecular level by using both a theoretical and

a synthetic approach. A theoretical approach is not necessarily pre-synthetic; neither is a synthetic approach post-theoretical. Zhang *et al.*[20] categorized different approaches adopted to rationally design MOFs. The two main approaches being a structural approach and a functional approach as shown in Figure (1.2). The structural approach includes efforts to design frameworks with expected structures, porosities and topologies, while the functional approach includes efforts to design frameworks that possess desired functionalities for particular applications.

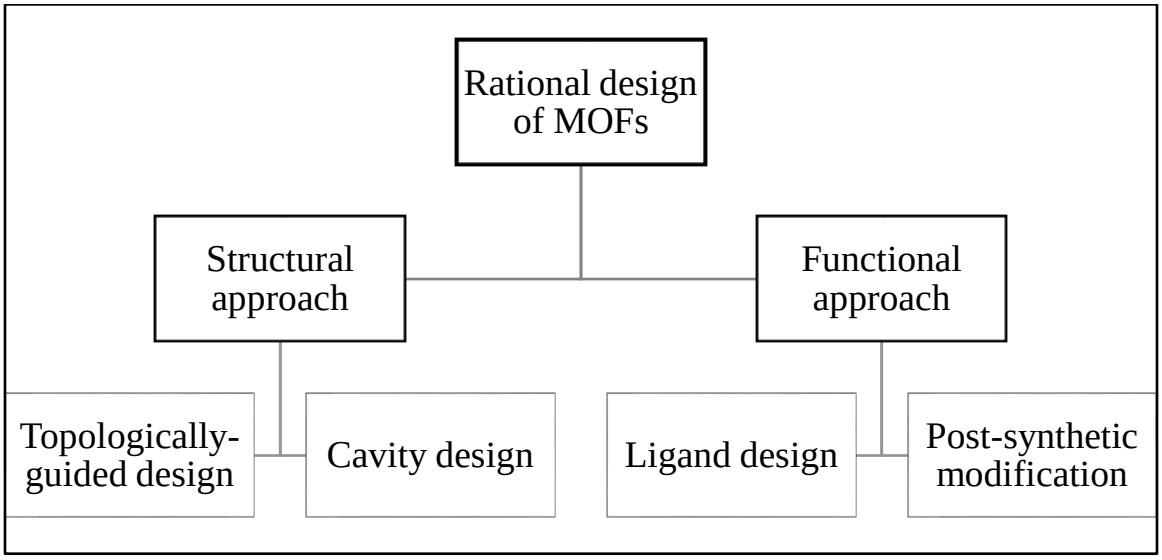

Figure 1.2 *Categorized rational MOF design approaches in recent efforts taken from ref. 20.*

1.5.1 The structural approach

Despite the wealth of building units, material scientists are still faced with a challenging task of predicting and harnessing the structure of desired features. The synthetic challenges stem from understanding and controlling both structural and compositional complexity. For example, the organic ligands in solution can adopt many different conformations during synthesis, which upon assembly of the framework, results in unexpected polymorphic MOFs with different structures and properties. Different metal clusters that can be formed from metal ions, can also result in different MOF structures. Another possible difficulty is undesired framework interpenetration. For MOFs with big enough pores, an identical second framework can grow in them causing an entwinning of

multiple lattices – a process called interpenetration.[21–23] These synthetic challenges pose as limitations to MOF design. Introducing a bottom-up design of topology and connectivity of the network prior to the synthesis of MOFs has provided novel insights into their rational design. The net topology of the MOF can be predicted from building units under given reaction conditions. The structure of the network is mainly dependant on the connectivity and the symmetry of the metal source and organic nodes. It is also affected by reaction conditions such as solvent, temperature and pH.

1.5.1.1 A topologically-guided design

A design of the desired topology is typically achieved by the use of fluorite topology.[24] MOFs with fluorite topology are advantageous because of their large cavities and non-interpenetrated nature. The large cavities result from the fact that the fluorite topology has two framework components that are symmetrically compatible: a 4-connected ligand (tetrahedral node) and an 8-connected metal cluster (octahedral node). Additionally, the fluorite topology usually exhibits high porosity. The structure of the fluorite is conceived as a cubic close packing of the calcium cations where all its tetrahedral interstitial cavities are filled by fluoride anions (Figure 1.3a), whereas the octahedral interstitial cavities remain unoccupied (Figure (1.3b)). To generate larger octahedral cavities, the 4-connected nodes should be augmented with a rigid tetrahedral ligand (Figure (1.3c)), which are connected by the 8-connected metal secondary building units. Using the same notion, the MOF has a close packing of metal clusters with its tetrahedral interstitial cavities occupied by ligands and its octahedral interstitial cavities vacant (Figure (1.3d)).

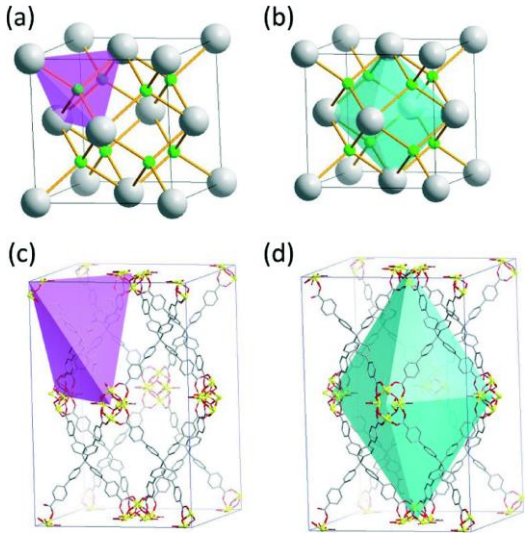

Figure 1.3 *(a, b) A fluorite-type structure showing tetrahedral and octahedral interstitial cavities from the cubic close packing of the calcium cation. (c, d) A fluorite topology where augmentation of the tetrahedral node occurred and therefore large pores resulted. Figure reproduced from ref. 21.*

1.5.1.2 Hierarchical-pore architectures

The use of fluorite topology in MOFs can only lead to a specific type of cavity, the octahedral interstitial cavity, with uniform size and shape. This is limiting since there exists other topologies that may give rise to more than one type of cavities. An example is the use of polyhedral building blocks, such as metal-organic polyhedral (MOPs) to make MOFs with hierarchical cavities.[25,26] Resulting frameworks are usually highly porous, with topologies of varying shapes and sizes. This is owed to the assemblies of discrete cages making up the MOPs, which contain high symmetries, and therefore leads to well-defined cavities and predictable structures. The utilization of MOPs is an example of a template directed strategy, which uses sacrificial templates such as surfactants, block polymers and metal-organic assemblies. In addition to MOPs, perturbation-assisted synthesis is another common approach to introduce hierarchical-pore architectures. The advantage of hierarchical porosity lies in the high degree of crystallinity and the simplicity of the one-step syntheses.[27] The creation of hierarchical porosity in MOFs has benefits in various applications of MOFs such as gas storage and separation.

1.5.1.3 Cavity design for particular applications

Customizing the cavity of MOFs is of paramount importance for separation processes, such as the separation of binary gas mixtures or different isomers. The cavity size and shape can influence the adsorptive behaviour to the MOF, wherein cavities with similar size and shape to a given molecule, and complementary polarity will likely retain it. Thus frameworks that contain these cavities will have higher affinity to this particular molecule.[28] The ideal case would be designing frameworks with adsorptive behaviours suited for a general type of species. Developments for CO_2 capture, separation of isomers and heterogeneous catalysis are examples of applications wherein customization of cavity size and shape exists.

CO_2 capture

Developments of single molecular traps are promising for applications in CO_2 capture.[29,30] Single molecular traps are made by coordinating metal clusters to organic linkers of suitable length and conformation to ensure a cavity of desired shape and size, and even polarity. The traps can be part of an extended network or exist in discreet cages. Moreover, single-molecule traps can be further functionalized by incorporating additional functional groups into framework structures with accessible traps. Li and co-workers[29] constructed a metal-organic polyhedral as a single-molecule trap using the ligand 3,3'-(naphthalene-2,7-diyl)dibenzoate connected by dicopper paddlewheels secondary building units. The cage consisted of two dicopper paddlewheels surrounded by the four ligands, making it a lantern-shape molecular cage with a 7.4 Å gap between the two adjacent metal units. Consequently, the cage was appropriate for one CO_2 molecule. A CO_2 molecule is linear and about 2.4 Å in length. It is positively charged at the carbon atom, and negatively charged at the oxygen ends. A typical M-O coordination bond length is about 2.0-2.8 Å, where M is a transition metal. As a result, two positively charged binding sites[31] separated by about 6.4-8.0 Å (2.4 + 2×M-O) can electrostatically hold a CO_2 molecule between them.

Separation of hydrocarbon isomers

The size and shape of a cavity can also be customized for separating liquid mixtures such as hexane isomers. The use of MOFs with triangular channels is of tremendous interest in both laboratory

and industrial scales for the separation of hexane isomers. Long[32] and co-workers developed a MOF that facilitated distinct types of shape-based molecular separations of hexane isomers. The crystal structure exhibited triangular channels.

Ligand design in heterogeneous catalysis

Another application that requires accurate cavity design is heterogeneous catalysis. Among other important factors that need to be considered, the size and pores of the MOFs should be conducive to the diffusion of reactants and products and the catalytic centres in the MOFs should be accessible.[20] The introduction of mesoporosity (defined as a material containing pores between 2 and 50 nm in diameter) into MOFs can be induced by ligand-fragment-co-assembly which includes introducing functional groups into the MOFs by functionalizing the original ligands.[33]

1.5.2 Functional approach

The introduction of functionalities into the MOFs expands the range of properties and applications. Various functional groups that can be incorporated enriches the usefulness of MOFs over other inorganic molecules. The functionality of a MOF is usually attributed to the two main interacting components, the metallic centres and the bridging organic ligands. It can either be derived from the individual components or the nature and type of connections between them. Pre-synthetic design is one of several ways in which expected functionalities can be introduced into a MOF. Other design strategies include network design of coordination architectures and secondary building units (SBU) design.

1.5.2.1 In applications of MOF adsorptivity

External stimuli can be used to control the adsorptivity of MOFs and this has applications in the capturing and releasing of substrates. This tuneable adsorptivity is possible via ligand manipulation. An example of such tuned adsorptivity can be found in a MOF developed by Park *et al.*[34] It was synthesized *via* a solvothermal reaction between $Zn(NO_3)_2 \cdot 6H_2O$ and H_2PDT (PDT = 2-(phenyldiazenyl)terephthalate. The organic ligand bears an optically sensitive diazo group and

can therefore undergo isomerization when irradiated by UV radiation or when exposed to heat as seen in Figure (1.4). The isomerization of the diazo group changes the shape, size and polarity of the pores and thus allows optical and thermal control of the adsorptive behaviour in the MOF. Park *et al*. showed that the use of radiation or heat improved the adsorptive behaviour. Furthermore, the MOF could go through multiple exposures to UV heat and still maintain its adsorptive integrity. The maintenance of its adsorptive behaviour proves it to be feasible for storage and release of gas.

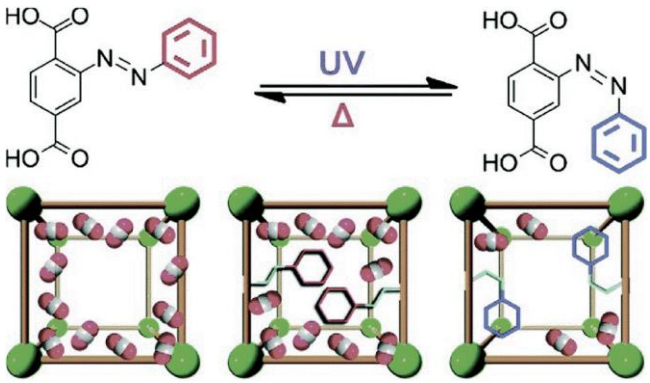

Figure 1.4 *Isomerization of the diazo groups induced by heat or UV radiation. Figure reproduced from ref. 35.*

1.5.2.2 MOFs in heterogeneous catalysis

Since it is convenient in MOF design to incorporate and distribute different catalytic centres, MOFs are viable candidates as catalysts. Heterogeneous catalysis is another application in which pre-synthetic ligand design is vital. Lewis acid and Lewis base moieties that can cooperatively catalyse a tandem reaction is just another example of a structural motif in a MOF that can be constructed from judiciously designed ligands.[35]

1.5.3 Post-synthetic modification

Instead of pre-synthetically designing the ligand to introduce functionalization into the MOF, one can modify the MOF post-synthesis. Post-synthetic modification involves the treatment of the MOF chemically without damaging or changing the infrastructure of the framework.

1.6 The dynamic behaviour of MOFs

In general, flexibility is perceived to be incompatible with robustness in MOFs. Robustness in this case refers to a feature of porous frameworks that are constructed from rigid components and that do not collapse upon guest removal. Structural dynamics such as the accommodative expansion and contraction of the framework upon inclusion of guest molecules have been studied and reported in third generation[9] coordination polymers. The flexible nature of MOFs originates from the ability to structurally transform its components when stimulated by heat, light or guest molecules. The structural transformation includes the environmental change of the secondary building blocks and the rotating, twisting, bending or tilting of organic linkers.[36–38] The environmental changes that can be undergone by the secondary building units include multiple reversible metal-ligand bond breaking. Furthermore, specialized coordination bond can transform a framework into a different one and sustain the porous framework. For example, hydrogen bonds and π-π stacking interactions introduce 'softness' in the porous framework of coordination polymers, where softness refers to compounds that exhibit non-porous to porous transformation upon inclusion of a gas molecule.[39] This is seen in the imidazole linker reorientations found in ZIF-8 which enable the discrimination of adsorbates by using molecular sizes.[40] Kitagawa and co-workers suggested a classification of flexible porous coordination polymers or flexible MOFs that form the basis for dynamic structural transformation resulting in three different subclasses as shown in Figure (1.5).[41,42]

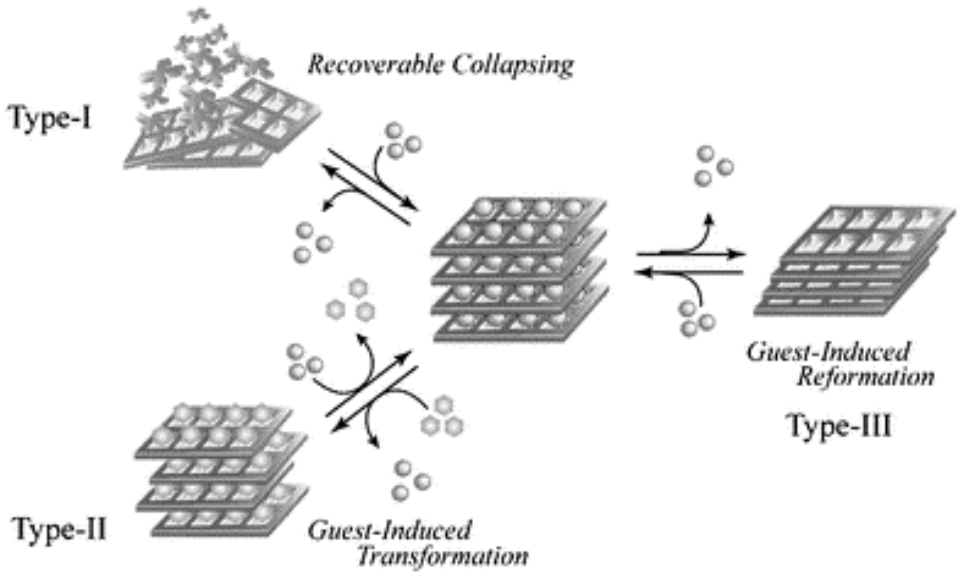

Figure 1.5 *A classification of flexible MOFs where three types of flexible MOFs can be distinguished. Figure reproduced from ref 79.*

This classification aims to describe the behaviour of flexible MOFs during the activation process, i.e. a post-synthesis treatment of MOFs involving the complete evacuation of adsorbed solvent molecules that might be remaining from synthesis. For type I of the flexible MOFs, the frameworks tend to collapse upon the removal of the guest molecule owing to the close-packing force. However, should initial conditions be restored, the crystalline nature is also restored. Unlike a crystal-to-amorphous transformation associated with Type I frameworks, Type II and Type III frameworks undergo crystal-to-crystal structural changes whereby the crystallinity of the network is maintained. Type II frameworks are associated with guest-induced transformations, whereas Type III frameworks are associated with guest-induced reformation. The structural changes of Type II and Type III frameworks can undergo an abrupt increase in the adsorption capacity. This behaviour shows up on adsorption isotherm curves as a stepwise adsorption-desorption isotherm.

1.6.1 Structural transformations

Dynamic structural changes in MOFs leads to features such as high selectivity for particular guests, hysteretic sorption and stepwise guest-uptake. These dynamic responses are introduced by various

structural motifs that can be placed into three main categories, the first category being chemical motifs such as interpenetration stacking. The second motif involves specialized coordination bonds that can be added to, reoriented, or cleaved. The last motif, which is not well-documented compared to the others, is the rotatable units incorporated on the bridging ligands.[43]

Ligands are defined as flexible once they have a rotating single bond in their structure. The rotatable region in the organic linker introduces the possibility of conformational changes of the flexible ligands which leads to different but often interesting frameworks. The flexibility of the ligand can play out both during the self-assembly process and in dynamic MOFs.[44] The difference between the two types of flexibility is that there is a conformational lock in the crystalline state of the former and the latter can be attributed to such properties as the *syn-anti* isomerism upon external stimulus. A solid-state transformation upon external stimulus can occur via, for example, cleavage of a coordination bond. [45]

The breathing phenomenon is an example of a dynamic property in soft porous materials where the transformation between large and narrow pore structures is evident in presence of guest molecules. The reversible changes (termed 'breathing') induce crystalline states with different pore volumes. A relatively small amount of adsorbed gas molecules is required to induce structural transitions. The breathing behaviour is common in the MIL-53 series such as the one prepared by Ferey *et al.*[46–48] Functionalisation of linker ligands can strongly impact the flexible breathing behaviour. Post synthetic modifications with functional groups such as linear alkyl anhydrides, nitrogen-containing bifunctional groups or alkoxy groups have been used to tune a material's ability to breathe.[49–51] The gate opening-and -closing behaviour is another prominent structural dynamic feature. Gate opening-and-closing refers to the transition from a closed and non-porous to an open and porous phase. This contrasts with the breathing behaviour, which involves a structural rearrangement of a unit cell.[52] Kitagawa *et al.*[53] reported a coordination polymer that had a rotable pillar incorporated into the framework with ethylene glycol side chains acting as molecular gates. The side chains lock and unlock as induced by guest molecules.[43] The rotation of the molecular gates is accompanied by the expansion of the cell dimensions.

In contrast, MOFs based on rigid units are able to retain porosity after the removal of guest solvent molecules from synthesis. However, some unique advantages can be realised in MOFs based on flexible units. For example, conformational freedom of organic linkers coupled with coordination preferences allows the construction of structurally diverse MOFs. Additionally, versatile conformational and coordination preferences allow the construction of polynuclear MOFs that can transmit magnetic exchanges.[54] Moreover, the use of flexible units in MOFs may endow dynamic behaviour as previously discussed. Indeed, it is a more challenging task to construct MOFs based on flexible ligands due to the possibility of the ligands adopting different conformations and therefore not leading to distinct symmetries during the self-assembly process.[44] In addition, some MOFs based on flexible ligands turn fragile and lose their porosity after removal of guest molecules as a result of flexible ligands not being able to sustain the framework.

It should be noted that the difference between flexible MOFs and MOFs based on flexible ligands is subtle. Flexible MOFs shows dynamic behaviour such as responding to external stimuli and this means the whole framework is dynamic, while the latter just implies that the building units are flexible. One cannot draw a direct link from flexibility/rigidity of the linker to the framework that results from it. Accordingly, flexible ligands can be incorporated into both rigid and flexible MOFs.

1.7 Gas sorption properties

The porosity of MOFs is frequently studied for applications in gas sorption.[55–58] In particular, surface area and gas adsorption affinity are features which require consideration in MOF designs and they are often considered together since they are dependent on each other.[59] Usually, MOFs exhibiting large surface areas also have large pore volumes. Their framework surfaces can further be functionalized to increase interactions with particular gas molecules. This functionalization can be achieved by constructing isoreticular MOFs by linking pre-designed isolated organic linkers with metal ions or using post-synthetic modifications.

The isoreticularity of a family of MOFs refers to the sharing of topology and metal centres, with variations in organic bridging ligands. The ligands can vary by length and functionalization

1.7.1 Design of ultrahigh porosity of MOFs

Permanent porosity in open MOFs was first established in 1998 through measurements of reversible gas sorption isotherms at low temperatures and pressures.[60] This major advancement has since been followed by preparation of MOFs with even higher surface areas (ultrahigh porosity) to increase the storage space per weight of the material. To achieve higher storage capacities, longer organic linkers are utilized. In addition to large voids due to the longer organic linkers, a substantial number of adsorption sites within the material is achieved. In principle, longer organic linkers lead to an increase in the number adsorption sites as there are more exposed faces and edges for gas adsorption. However, large void spaces make the framework susceptible to interpenetration and the subsequent clogging up during MOF synthesis. In addition, expansion of organic linkers often yields fragile frameworks.[61] To prevent interpenetration, topologically-guided synthesis of the framework is effective.[62] Even with an interest in large void spaces, it is vital to ensure that the micropore range is able to accommodate small molecules. this can be achieved by a judicious choice of organic linkers Exceptionally large pore apertures that can accommodate large molecules such as proteins are also possible.[63]

1.7.2 Functional groups

The modulation of guest-host interactions to improve adsorption can be done via judicious pre-selection of functional groups. Most MOF linkers bear functional groups such as carboxylate or azolate groups, that particularly bond to the metal ions in the framework. Thus, only relatively weak interactions with guest molecules are possible in the interior surfaces of most MOFs. Additional functional groups that provide the possibility of stronger and more directional interactions between the framework and the guest molecule can be incorporated.[64] Crystallographic studies can be used to reveal the role of available functional groups within MOF pores in forming interactions with adsorbed guest molecules. For example, *in situ* single-crystal

X-ray diffraction can be used to locate gas molecules inside a MOF.[13,65] Powder diffraction and inelastic neutron scattering can be used in combination to reveal binding sites of guest molecules within MOF pores as well.[66]

Many MOFs have been functionalized with -NO_2, -NH_2, -CONH-, -NO_2, -OH, -CN, -SO_3H or pyridine to enhance -CO_2 adsorption.[67–73] This is an attempt to increase electrostatic interactions between the surface of the framework and the large quadrupole moment of CO_2.[74] This interaction, between CO_2 and various functionalities incorporated on the MOF organic linkers, is addressed at a molecular level by theoretical calculations in combination with experiments.

1.7.3 Open metal sites

Increasing the surface area of a MOF is not the only tool for increasing the gas uptake capacity. Similar to the employed functional groups in linker ligands, MOFs with open metal coordination sites create access for direct interactions with gas molecules. [75–77] These interactions may assist in determining binding sites and quantifying the binding energy of the gas molecules.

1.8 Fluorine-functionalized MOFs

Porous materials which contain fluorinated links show interesting gas sorption properties due to surfaces with exposed fluorine atoms.[78–80] Fluorous MOFs (F-MOFs) result from the substitution of hydrogen atoms for fluorine atoms in linker ligands, either partially (not all hydrogen atoms are substituted) or extensively (forming perfluorinated ligands). The resulting channels and cavities are either fluoro-lined or fluoro-coated. Compared to their non-fluorinated equivalents, F-MOFs are expected to possess enhanced gas adsorptivities and selectivity, catalytic activity, and higher stability to oxidation, light and heat.[81,82] Several other functionalities can be introduced into a MOF by incorporating fluorination, including chemical and biological inertness, and excellent optical and electrical properties.[83]

1.8.1 Effect of fluorination

Organo-fluorine compounds are ubiquitous in many different applications (medicinal chemistry, speciality materials, fine chemicals). This widespread use of organo-fluorine compounds is owed to the fascinating chemistry associated with the C-F bond. The fluorine substitution introduces useful molecular properties as outlined before. In addition to this, the stereoselective fluorine substitution can be adopted as a tool for the synthesis of shape-controlled functional molecules. The size and the electronegativity of the fluorine atom has implications on the on the general aspects of the C-F bond in the organo-fluorine compound and on the conformational effects associated with the C-F bonds.

1.8.1.1 The highly polarized C-F bond

The small size of the fluorine atom, intermediate between hydrogen and oxygen in size and length, has implications on its type of chemistry. For example, it can be added into organic molecules as a substitution for hydrogen without a dramatic change in molecular size. However, the high electronegativity of the fluorine atom leads to polarization that imparts an electrostatic character to the C-F bond instead of a covalent one and in this sense, the C-F bond is a dramatic change from the C-H bond. The highly polarized C-F bond leads to a large dipole which can interact with other dipoles that come close. Preferred conformation of compounds with the C-F bond in them can thus be explained by electrostatic interactions. Another consequence of the polarized C-F bond is the low-lying σ* antibonding orbital, associated with the C-F bond and positioned behind the C atom in the C-F plane. This vacant orbital acts as an electron density acceptor from donors such as lone pairs and σ-bonds. The three lone pairs on fluorine are tightly bound to the nucleus due to the high electronegativity of the atom and are therefore reluctant to participate in resonance or interact as hydrogen bonding acceptors (i.e. fluorine is only a weak H-bond acceptor). However, the C-F bond typically interacts with its environment through electrostatic/dipole interactions.

1.8.1.2 Conformational effects of the C-F bond

Dipole-dipole interactions

The C-F bond chiefly interacts with its environment through electrostatics as a result of the partially negative fluorine. The electrostatic interactions can either be dipole-dipole or charge-dipole in nature. The substantial ionic character of the C-F bond gives rise to large dipole moments. The molecular dipole moment of fluoromethane is 1.85 D, which rises to 1.95 D in difluoromethane. The dipole of the C-F bond plays a significant role in understanding conformational behaviour in organo-fluorine compounds such as in fluorine-bearing drug molecules where the receptor can bind with the fluorine atom oriented towards a partial positive amide carbon atom or an acidic hydrogen in a protein receptor as seen in Figure (1.7).[84,85] Such intermolecular electrostatic interactions are relatively weak: for example, the C-F···H-O is approximately four times as weak as the normal hydrogen bond.[86] In contrast, the electrostatic interactions that can occur within the organo-fluorine molecule can be considerably stronger just as in the case of α-fluoroamides.[87]

Dipole-dipole interactions stabilize certain conformations as seen before. However, they can destabilize certain conformations such as in the case of 1,3-difluoroalkanes wherein is an energetic penalty which arises from two aligned parallel C-F bonds. Molecules that are 1,3-*syn* fluorinated prefer to twist in order to avoid the 1,3-C–F dipole repulsion.

a) dipole-dipole interactions

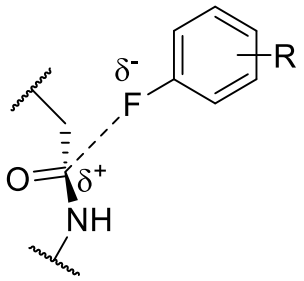

1

C--F = 2.9 Å

~0.2 kcal/mol

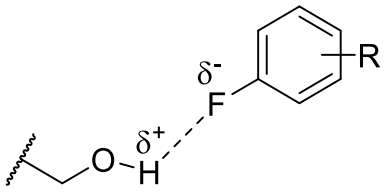

2

H--F = 2.5 - 3.0 Å

~2 kcal/mol

b) charge-dipole interactions

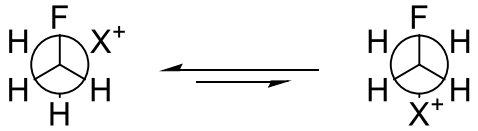

0.0 kcal/mol

3 (X^+ = -NH_3^+): -5.8 kcal/mol

4 (X^+ = -OH_2^+): -7.2 kcal/mol

5 (X^+ = 1-pyridyl): -3.7 kcal/mol

c) hyperconjugation effects

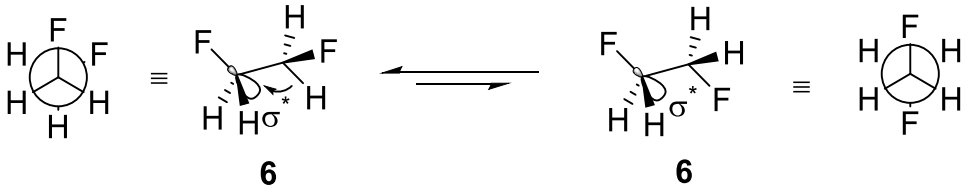

-0.8 kcal/mol

0.0 kcal/mol

Figure 1.6 *Conformational effects associated with the C-F bond. Figure reproduced from ref. 92.*

Charge dipole interactions

A charge-dipole interaction between the C-F bond and a formal charge is a much stronger interaction than the dipole-dipole interaction in energy terms. An example of a charge-dipole interaction is observed in 2-fluoroethylammonium ion **3** and protonated 2-fluoroethanol **4** in which the *gauche* conformers are strongly preferred as a result of the partially negative fluorine atoms being close to the formally positively-charged oxygen or nitrogen.[88] The charge-dipole interactions are more prominent than H-bonding that may exist in systems such as **5**. Having said that, it is possible to envisage an intramolecular hydrogen-bonding assisting stabilization of the *gauche* arrangements in **3** and **4**. However, the *gauche* arrangement is still maintained in **5**, wherein hydrogen bonding cannot be accommodated.

Hyperconjugation effects

Another consequence of the highly polarized C-F bond is the presence of a low lying σ* antibonding orbital associated with a C-F bond. This means electron density from electron rich bonds (such as C-H, C-C or π), lone pairs or nucleophiles can be donated into the $\sigma^*_{C\text{-}F}$ to stabilize conformations, provided they are aligned correctly stereoelectronically.[89]

NMR and theoretical studies have shown that 1,2-difluoroethane its *gauche* conformers have lower energy than the *anti* conformation. This is a surprising result since the fluorine atoms may reasonably be expected to have higher repulsive interactions in the *gauche* arrangement. The most widely employed and convincing argument for the fluorine *gauche* effect in 1,2-difluoroethane is hyperconjugation. In the hyperconjugation model, the *gauche* conformer stabilizes the $\sigma_{C\text{-}H}$ $\sigma^*_{C\text{-}F}$ interactions as a result of the adjacent bonds correctly aligned to donate electron density. In the case of the *anti* conformer, the highly polarized and electron deficient C-F bond is now *anti* to the $\sigma^*_{C\text{-}F}$ orbital and it not correctly aligned to receive electron density. The C-F bond is less electron releasing compared to the electron rich C-H/C-C bonds and therefore hyperconjugation does not occur.

Wilberg *et al.*[90] suggested a convincing alternative to hyperconjugation which argues for geometric changes instead. Wilberg argued that *σ* bonds (C-H or C-C) undergo geometric changes

due to the highly polarized C-F bond. The C-H and C-C bonds are electron rich whereas the C-F bond has electron density mostly at the fluorine atom. Thus, the carbon atoms bend towards the fluorine atom. It is in the *gauche* conformation where a good overlap exists in the C-C bond. The *anti* arrangement skews the electron density in different directions towards the fluorine atom with a resultant poorer overlap of the C-C bond as shown in Figure (1.8). This is referred to as the 'bent bond' analysis. However, the current consensus rates hyperconjugation as the greater contributor for rationalizing the *gauche* effect.[91]

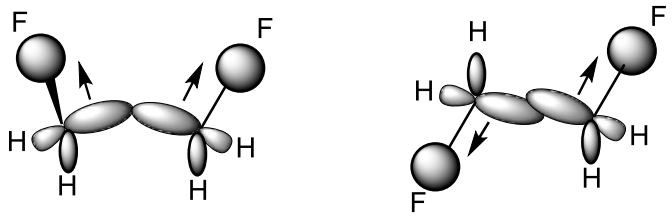

Figure 1.7 *Wilberg's bent bond analysis to rationalize the gauche (left) effect in 1,2-difluoroethane.*

1.8.2 Fluorination Patterning

The concept that *structure determines property* in chemistry is a powerful one because it provides insight into why particular drugs are effective, why a certain chemical is toxic, why certain materials work the way they do and so on. This applies to the fluorination of MOF linkers where the fluorination pattern matters. The fluorination pattern is guided by targeted topologies and ligands prior to experimental trials and/or desired chemical, physical and biological properties. For example, Hulvey *et al.*[80] particularly wanted to enhance H_2 adsorption enthalpies and therefore improve H_2 gravimetric and volumetric storage capacities in coordination polymers. They therefore chose to target structures containing fluorinated ligands. The fluorinated ligands, which allowed desired 'perfluorinated' surfaces, were used in combination with other small ligands.

Pachfule *et al.*[92] synthesized fluorinated MOFs (together with their non-fluorinated analogues) to improve H_2-storage properties by partial fluorination. In this case however, the partial fluorination was not introduced by the incorporation of the second ligand but rather by the substitution of some

hydrogen atoms with fluorine atoms. For Hulvey *et al.* and Pachfule *et al.*, the decision for a fluorination pattern was guided by targeted structure-property relationships, where the fluorinated frameworks were compared to their non-fluorinated analogues.

Another approach that can guide fluorination patterns in MOFs is the systematic investigation performed by Bu *et al.*[78] to elucidate the effect of fluorination by increasing the number of fluorine atoms on the linker and investigating the resulting effects as the degree of fluorination increases. This approach can help with the determination of the number and position of fluorine atoms required to achieve desired properties. The fluorine pattern can also come from the type of bridging ligand used in the framework - trimethyl groups (CF_3) can be incorporated into frameworks as terminal ligands to introduce CF_3-decorated walls. This incorporation can enhance properties such as selectivity for binary gas mixtures which can be attributed to the electrostatic interactions between the polar CF_3 and a polar guest molecule. The CF_3 group also introduces a hydrophobic character to the fluorinated pore surfaces which leads to selective adsorption and high capacity for hydrophobic guests. Likewise, perfluoroalkyl substituents, bearing polar adsorption sites, can be adopted into MOFs with two methods. They can be adopted as substituents on bridging ligands or using terminal ligands bearing them.[93]

Fluorinated anions as illustrated in Figure (1.6) are can also be used as building blocks for the construction of F-MOFs. Compared to organic fluorinated ligands, inorganic fluorinated ligands prove more difficult to be modified.

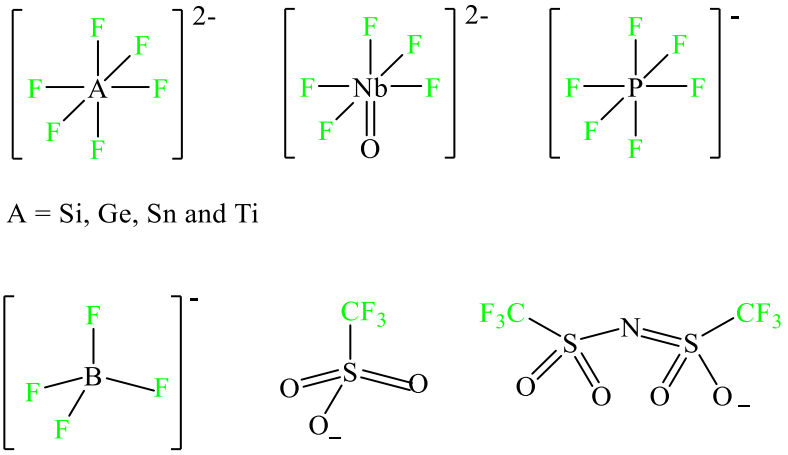

Figure 1.8 *Inorganic fluorinated anions incorporated into F-MOFs as building blocks.*

Vicinal fluorination or *n*, *n*+1 fluorination, a structural motif popular in drug design, is not widely explored in the synthesis of MOFs.[94] It is a form of fluorination patterning that can impact physicochemical properties of relevance to MOFs such as conformational flexibility. *Vicinal* fluorination can control acyclic conformation using stabilizing hyperconjugation and electrostatic interactions.[95] The control over acyclic conformation through design of compounds gives rise to predictable conformer populations. With this idea, this work aims to investigate what control *vicinal* fluorination has on MOF linkers with acyclic bridging chains in isolation and in the framework.

1.9 Computational characterization of MOFs

Computational approaches are a powerful tool for the discovery of novel families of MOFs, and they can help unpack their complex energy landscapes. They offer an additional perspective for the characterization of materials and are often used as complementary studies to experiments. The continued development of computational methods, with the enhancement of computational power and resources, has dramatically increased the range and sizes of problems that can be addressed through computer modelling. There are several computational chemistry methods commonly used in MOF literature, to describe their structure and characterize their various properties. These methods can range from a quantum mechanical (QM) level to classical molecular simulations.

1.9.1 Characterizing structural properties

1.9.1.1 Crystal structure prediction

Crystal structure prediction (CSP) involves the *in silico* search, screening and identification of a possible equilibrium crystal structure, starting from a compound's chemical diagram. It assumes that the crystal structure will be the thermodynamically most stable of all possible structures. Structure prediction usually begins with a minimal amount of empirical knowledge; there are typically undetermined atomic coordinates, no cell parameters, or the symmetry and space group available. It results in a list of candidate periodic crystal structures with a list of predefined targeted structural or topological features, or functionalities. Identifying an equilibrium structure of an existing solid using force field and electronic structure calculations, starting with an experimentally determined structure or an approximate structure, is not considered to be genuine crystal structure prediction. This includes routines on known structures, including those derived by computational desolvation (and optimization of atomic coordinates and cell parameters) or computational substitution, as in this work.

There is a large variety of CSP computational strategies developed to explore the configurational space of molecular crystals and inorganic solids. These include algorithms based on simulated annealing, genetic algorithm methods and molecular packing approaches.[96–98] This class of methods rely on global optimization approaches that involve a 'cost function' over which minima are searched for. An example of a building-block computational approach for structure prediction is the Automated Assembly of Secondary Building Units (AASBU), which uses predefined SBUs with tailored "sticky-atom" interaction potentials between them.[99] With this principle, SBUs auto-assemble into 3D networks through a series of simulated annealing and energy minimizations. The requirement of simulated annealing and energy minimizations to converge structures makes the AASBU method computationally expensive. The alternative would be to construct frameworks from SBUs by direct enumeration of topologies compatible with the available building blocks. The principle of isoreticularity, is another property of MOFs that can be leveraged for structure

prediction.[21] This means that based on a given structure for a parent MOF, it is possible to predict structures of isoreticular analogues.

The aforementioned CSP computational strategies enable computationally-guided design for novel frameworks, and therefore replacing the trial-and-error approach in MOF synthesis that is often employed. However, they still cannot generate a large number of hypothetical structures. Hence, there have been research efforts to enable large scale screening of potential structures that generate a larger number of hypothetical structures.[100,101] Large scale screening generates all possible framework structures from a chemical library of building blocks. These can then be stored in databases along with basic characterization information, enabling a screening of hypothetical structures for specific applications. The characterization information is usually obtained by evaluating geometrical properties or host-guest interactions and adsorption properties.

1.9.1.2 Geometrical properties

Geometrical properties (surface area, pore volume and pore size distribution) are calculated based on the unit cell parameters and atomic positions. They are therefore calculated once a MOF structure is determined, either crystallographically or using QM calculations. The determination of the geometrical properties relies on the description of a solid where each atom of the framework is a hard sphere centred on the atomic coordinates of the crystal. These hard spheres have radii equal to the van der Waals (vdW) radii. The probe molecules, used in order to calculate the accessibility of guest molecules, are also described as spherical, with a radius equal to the kinetic radius of the specific molecule.

Accessible surface area

To characterize the geometry and solvent interaction of microporous solids, the most common descriptor used is the accessible surface area and accessible pore volume, which represents the surface and volume, respectively, accessible to guest molecules of a particular size. There are three possible atom volume surfaces that can be calculated, as shown in Figure (1.9).

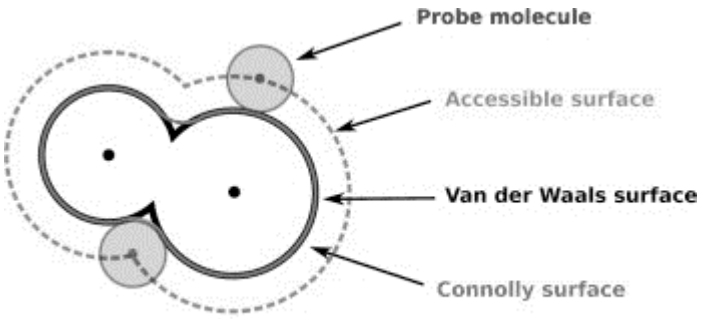

Figure 1.9 *Three types of atom volume surfaces commonly used to characterize the geometry of microporous solids. Figure reproduced from ref 119.*

The vdW surface is the surface that intersects with the vdW radii of the atoms in the structure. It is equivalent to the solvent surface where solvent probe radius is zero, i.e. the vdW surface does not depend on the probe size. The accessible solvent surface is the surface spanned by the locus of the probe centre as the probe rolls over the vdW surface. Finally, the Connolly surface, by definition, is at the boundary between the probe molecule and the atoms (as represented by their vdW radii). The Connolly surface is also called the solvent-excluded surface, since it establishes the space inaccessible to the spherical probe. The accessible surface area can be used to characterize crystalline solids in adsorption applications. In particular, it has been shown that the accessible surface area calculated with a probe molecule of a radius equal to the kinetic radius of N_2 can be directly compared to the BET surface area from experimental nitrogen gas isotherms.[102]

The calculation of the accessible pore volume does not involve the actual rolling of a probe molecule. Instead a Monte Carlo (MC) protocol is employed. Sampling methods used to calculate molecular surfaces are popular numerical methods employed for the evaluation of the accessible pore surface of porous solids. Figure (1.10) shows a scheme to evaluate the accessible pore volume. A sample of random points is set up on the solvation sphere of radius r_i and $r_{p,}$ where r_i is the radius of the absorbent atom and r_p is the radius of the probe molecule.

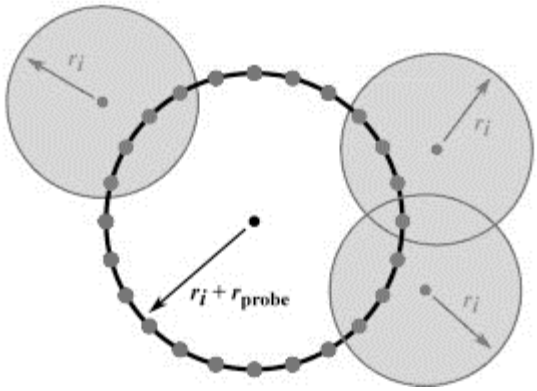

Figure 1.10 *A scheme for the evaluation of accessible surface area contributed by each atom through sampling its "solvation sphere". Figure reproduced from ref 119.*

From this sample of points, there are a group of points that are not hidden inside neighbouring atoms. The group of points are then a contribution of atom to the total accessible surface area. This procedure is called the Shrake-Rupley algorithm.[103] The accessible surface area associated with the adsorbent atom *i* under consideration is then given by Equation (1.1),

$$a_i = f.\pi.\sigma^2 \tag{1.1}$$

where *f* is the fraction of points that are not hidden inside neighbouring atoms, and $\sigma = 2r_i + 2r_p$ is the diameter of the solvation sphere. The total accessible area is then given by a sum of individual accessible areas given by Equation (1.2). This absolute property, usually calculated in $Å^2$, can be converted into more useful properties such as accessible surface area per gram of the material or per unit volume.

$$A_{abs} = \sum_{i=1}^{N} a_i \tag{1.2}$$

Accessible pore volume

The objective of pore volume accessibility is to determine whether a porous network of a material is fully accessible to a spherical probe molecule of a given probe radius. The accessibility of a

network means that the probe molecule can construct a continuous trajectory from one face of the simulation cell to another, without overlapping with any particles. The internal void volume is a particularly important geometrical property for microporous solids, as it determines the permeability to guest molecules and the adsorption capacity. Characterizing pore volume is often the most important and sometimes the only parameter to characterize an adsorbent.

A theoretically determined value for the pore volume can be calculated and then used to compare with an experimentally derived value, for example, from N_2 adsorption experiments at low temperatures.[104,105] Discrepancies between the theoretical and experimental values can provide insight into the characteristics of the crystal structure. For example, should the experimental pore volume be found to be smaller than the theoretical one, an incomplete desolvation, limited permeability at the surface and crystal defects can be suggested. Moreover, discrepancies between theoretical and experimental pore volumes further emphasizes the poor representation of crystal structures in simulations.

A similar analytical method used to evaluate the accessible surface area is also used to evaluate the accessible pore volume. The analytical calculation of the geometric pore volume requires a consideration of all the many-body overlaps between atoms of the absorbent. This makes the MC protocol the most efficient method of calculating the accessible pore volume. As in the case of accessible surface area, a few points are randomly sampled in the unit cell or on a 3D grid. Should a point overlap with an atom, i.e. the distance of the atom from the point is less than its vdW radius, a value of zero is assigned. Otherwise, a value of one is assigned. The void fraction of the geometric pore volume θ_{Gm} of the crystal from N sample points is then given by Equation (1.3).

$$\theta_{Gm} = \frac{\sum_1^N value}{N} \tag{1.3}$$

The geometric pore volume is then obtained by dividing θ_{Gm} by the density of the framework. The pore volume obtained in this way will always be an upper bound, as the volume of the large pores are summed together with volumes of the small pores that are inaccessible to guest molecules.

Pore size distribution

A similar MC procedure is employed to calculate the pore size distribution, and the pore range of interest is then divided into small bins. A sample point is randomly chosen in a simulation cell, ensuring that it is within an atom. The sample point is then tested for overlaps with the structure atoms. If no overlaps are encountered, the pore is probed to find the largest possible probe that contains the sample point that does not overlap with other atoms. Once the largest radius, *r*, has been established, the value of the bin corresponding to that radius and that of smaller radii are incremented by one. The bin distribution can then be normalised to correspond to the monotonically decreasing cumulative pore volume function $V_p(r)$, which is essentially the volume of the porous space that can be covered by spheres of radius *r* or smaller. The pore size distribution function becomes the derivative, $dV_p(r)/dr$, and can be obtained via numerical differentiation of $V_p(r)$.

1.9.2 Characterizing physical properties

Physical properties of porous materials include mechanical, thermal, optical and electronic responses to stimuli, which can all be predicted computationally. In studies of the mechanical properties of MOFs, predictive calculations are employed to obtain properties such as bulk moduli, elastic constants, Young's and shear moduli of a framework.[106,107] Elastic moduli of MOFs can quantify the flexibility. They can determine the ability of a material to undergo large structural changes in response to external stimuli.[108,109] Another mechanical property that can be predicted computationally is the negative linear compressibility. This property quantifies the expansion of the material under hydrostatic compression.[110] Since computational studies of compression experiments allow the determination of structure as a function of pressure, they can also yield information outside the elastic regime, such as pressure-induced structural transitions. Other physical properties of MOFs include thermal and optical properties, useful for understanding the response of MOFs to heat and light.

1.9.3 Adsorption

There are several computational methods that perform simulations on varying lengths and timescales. For shorter lengths and timescales, simulations are available that calculate electronic properties based on QM approaches. At larger lengths and timescales, methods employed exploit the statistics associated with molecular configurations. Two approaches exist for generating molecular configurations, those that generate states of the system evolving in time using Newton's laws of motion and those that generate states at random. It is the latter that are used for the study of adsorption in porous solids.

1.9.3.1 Grand Canonical Monte Carlo

The Monte Carlo (MC) protocol is the procedure of choice for modelling adsorption in porous materials and the thermodynamic properties thereof. Adsorption isotherms of porous materials can be calculated using grand canonical Monte Carlo (GCMC) methods. The simulation models adsorption inside a rigid porous matrix of fixed volume, *V*, for given values of temperatures (*T*) and chemical potential (μ) of the bulk fluid.[111,112]

In MC simulations, a configurational sampling for the system under study is performed via a stochastic process, by random moves weighted by the configuration's Boltzmann probability. The MC moves typically include translations, rotations and intramolecular displacements or conformational changes. In addition to the random moves of MC simulations, GCMC simulates the interchange of molecules between the pores and an external reservoir of a bulk fluid as the molecules are inserted into the pore volume and deleted. This type of a sampled ensemble can be directly simulated with a thermodynamic equilibrium between two phases without an explicit interface.

Each point on a simulated adsorption isotherm is obtained at fixed μ, *V*, *T*. The full isotherm is a function of μ, $N_{ads}(\mu)$, where N_{ads} is the average number of molecules adsorbed on the porous material. The conditions of the simulation are close to the thermodynamic conditions of

experimental adsorption measurements. However, differences in the simulation and experiment needs to be considered. The first difference involves relating the chemical potential used in GCMC to the pressure, *P*, of the external fluid measured experimentally. This is achieved by using Equation (1.4), an equation of state given as

$$\left(\frac{\partial \mu}{\partial P}\right)_T = V_m\,(P,T) \tag{1.4}$$

where V_m is the molar volume of the fluid, which is obtained prior the MC simulations or empirically. At low pressures, an ideal gas is adopted to relate pressure and chemical potential as shown in Equation (1.5).

$$\mu = \mu^0 + RTln\left(\frac{P}{P^0}\right) \tag{1.5}$$

Another important difference between simulated and experimental data is that GCMC uses absolute adsorption properties, whereas the experiment uses excess (i.e. relative to an ideal gas) adsorbed properties. This discrepancy becomes significant in high-pressure experiments and needs to be accounted for.[113]

In addition to the above-mentioned outputs of GCMC, equilibrium thermodynamic properties, and a series of configurations generated at given conditions, GC can also include energetic quantities such as isosteric heats of adsorption. These quantities can be used for validating data obtained from simulations by comparing them to experimental data. A series of configurations generated during MC simulations can also be used to obtain volumetric information. For example, in adsorption, density and potential energy map distributions of adsorbed molecules can be plotted to gain insight into the mechanism of adsorption and positions of probable binding sites.

1.9.3.2 Classical interaction potentials

As seen before, MC simulations rely on the evaluation of the energy of configurations generated to work out the Boltzmann probability of the configurations. This essentially means that the accuracy of the averages computed through GCMC is governed by the accuracy of the description of interactions between molecules in the system. These calculations are of single configuration energies and are made on the order of millions of times per GCMC simulation. As a result, QM calculations become ill-favoured for the evaluation of energies of each configuration generated in GCMC. Thus, classical models are resorted to for calculating the interactions between gas molecules and the MOF.

Force fields or interaction potentials, are functions of bonded distances, angles and torsions, as well as non-bonded interactions, with chemically meaningful interpretations. In the case of modelling MOF adsorption, the adsorbate-adsorbent and adsorbate-adsorbate interactions are broken down into energetic terms representing Coulombic interactions, dispersion, interatomic repulsion, polarization and so on. Many several functional forms that describe these interactions are available, these include the commonly used Lennard-Jones and Buckingham potentials, as well as the Morse potential. Intramolecular terms are also considered for all molecules, excluding the smallest, rigid molecules. Intramolecular interactions include stretching, bending and torsion potentials. The total interaction energy, *U*, which is usually divided into bonding and non-bonding (van der Waals and electrostatic) contributions, is expressed as a sum of all these potentials as indicated by Equation (1.6).

$$\begin{aligned} U = & \sum_{bonds} u_b(\boldsymbol{r}) + \sum_{bends} u_\theta(\theta) + \sum_{torsion} u_\varphi(\varphi) + \sum_{out\ of\ plane\ blends} u_\chi(\chi) \\ & + \sum_{bond-bond} u_{bb}(\boldsymbol{r}, \boldsymbol{r}') + \sum_{bond-bend} u_{b\theta}(\boldsymbol{r}, \theta) \\ & + \sum_{bend-bend} u_{\theta\theta'}(\theta, \theta') + \sum_{bond-torsion} u_{b,\varphi}(\boldsymbol{r}, \varphi, \boldsymbol{r}') \\ & + \sum_{bend-torsion} u_{b,\varphi}(\boldsymbol{r}, \varphi, \theta') + \sum_{non-bonding} u_{nb}(\boldsymbol{r}) \end{aligned} \tag{1.6}$$

In general, one can add as many *ad hoc* potentials as one desires. However, the more terms are present in the force field, the more computationally expensive the calculations become. The challenge with choosing a suitable force field is between accuracy and transferability. Transferability of a force field means that the interaction potentials can describe the same type of atom in many different materials that have the same parameters. The most popular transferable force fields available are UFF (Universal Force Field) and DREIDING.[114,115] Both provide generic potential parameters for elements throughout the periodic table. Additionally, organic linkers and metal ions of MOFs are also covered. While generic force fields can lead to reasonable agreements in cases of adsorption of small non-polar molecules, when modelling adsorption of polar guest molecules, the force field requires supplementary atomic charge calculations, to describe the Coulombic interactions. Several classical methods are available for the calculation of partial charges in molecular systems based on high level QM calculations.[116–118] Additionally, generic force fields are in some cases required to be extended to handle a variety of elements (usually transition metals), or improve the description of other atoms.[119] There have been methodologies proposed for the development of MOF force fields,[120,121] but these have been applied to only a limited number of materials, as yet. The development of MOF force fields for the simulation of adsorption in MOFs is still an open challenge.

1.9.3.3 Challenges of MOF modelling

The current computational studies of MOFs are not without open questions and important challenges remain for further development. An important and common challenge is that of modelling crystal defects and disorder. Computational methods utilize periodic representations of the crystalline structures, this means that they model perfect crystals with no defects or disorder. This implies that defects are ignored during simulations but invoking them can provide insight into the differences between modelling and experiments. The computational study of MOFs can and has provided evidence on the crucial impact of the presence of disorder, and the extent thereof, on the structural, mechanical and thermal properties of MOFs.[122,123] This has been performed by using both QM and classical methods, such as periodic density functional theory (DFT) calculations and

GCMC, respectively.[124,125] Modelling studies have so far not been able to answer why some MOFs present disorders and others do not.[112]

The realization of the prevalence of flexible or stimuli-responsive MOFs and their potential application has led to the emergence of an entire subfield of computational methods dedicated to their modelling. However, this newly emerged subfield is not without its challenges. The nature of flexible MOFs is accompanied by a need to systematically develop high-accuracy interaction potentials. The extra degree of complexity in highly flexible materials is brought on by the requirement to accurately describe the intermolecular interactions of the framework.[112] To describe the interaction potentials, transferable force fields can be used, along with hand-tuned metal-organic bending and torsion terms. They can then be optimized to reproduce certain properties or experimental data, such as adsorption isotherms. The challenge then lies in the fact that these modified transferable force fields are not entirely generalizable: the resulting force field is only tested and validated on limited experimental data and it cannot be systematically improved since the optimization procedure is undertaken using too many constraining parameters fitted on a relatively small data set.[126]

Lastly, the vast number of organic ligands and metal ions that can be used for MOFs, coupled with the growth of computational power and more advanced modelling techniques, has spawned challenges associated with high-throughput computational screening of porous materials in general.[127,128] The challenges arise from the novel questions of how to best exploit already-existing databases for materials discovery.

2

Theoretical background

Computational chemistry provides a medium in which models representing both microscopic and macroscopic systems can be described. Quantum mechanics (QM) explicitly recognizes the fundamental differences between systems of these two size extremes. QM describes in a formal way the fundamental equations that are used to construct computational models. The fundamental postulate in quantum mechanics is that the wavefunction ψ exists for any chemical system, and that the state of the system is completely specified by it. In addition, for every measurable observable property in classical mechanics, there exists an equivalent linear, *Hermitian* operator that acts upon the wavefunction to return the observable property. This postulate forms the foundation for the eigenvalue problem called the Schrödinger equation (SE),

$$\hat{\mathcal{H}}\psi = E\psi \tag{2.1}$$

The operator in Equation (2.1) that returns the system energy *E*, as an eigenvalue, is called the Hamiltonian operator, $\hat{\mathcal{H}}$. The basic form of the Hamiltonian operator considers five contributions to the total energy of a system. These include the kinetic energy of the electron and the nuclei, the potential energy from the attraction of the electrons to the nuclei, and the interelectronic and internuclear repulsions. Less often considered energy contributions include those which exist in the presence of an external electric field, in the presence of a magnetic field, in cases of significant spin-orbit coupling, such as in heavy elements, and in cases where relativistic effects need to be accounted for. The Hamiltonian can be notated as,

$$\hat{\mathcal{H}} = -\sum_i \frac{\hbar^2}{2m_e}\nabla_i^2 - \sum_k \frac{\hbar^2}{2m_k}\nabla_k^2 \sum_i \sum_k \frac{e^2 Z_k}{r_{ik}} + \sum_{i<j} \frac{e^2}{r_{ij}} + \sum_{k<l} \frac{e^2 Z_k Z_l}{r_{kl}} \tag{2.2}$$

where *i* and *j* run over electrons, *k* and *l* run over nuclei, $\hbar$ is Planck's constant over 2π, m_e and m_k are the mass of the electron and nucleus *k* respectively and r_{ab} is the distance between particles *a* and *b*.

In this chapter, the following textbooks were closely followed: *Essentials of Computational Chemistry: Theories and Models* by Christopher J. Cramer;[129] *A Chemist's Guide to Density-Functional Theory* by Wolfram Koch and Max C. Holthausen;[130] *Introduction to Computational Chemistry* by Frank Jensen;[131] *Handbook of Computational Chemistry* by David Cook.[132]

2.1 Approximating the wavefunction

In general, Equation (2.1) has many acceptable eigenfunctions ψ for a given system (molecule), each returning a different associated eigenvalue *E*. Since the operator is *Hermitian*, there exists a complete orthonormal set of wavefunctions ψ_i with eigenvalues E_i. The variational principle[133] offers a prescription for minimizing the wavefunction energy and obtaining the 'best wavefunction' of the ground state. This is done by considering an arbitrary *trial wavefunction* Φ, that is a well-behaved function of the coordinates of the system's particles. The true wavefunctions are defined to be a set of orthonormal functions ψ_i, that forms a complete basis, i.e.,

$$\Phi = \sum_i c_i \psi_i \tag{2.3}$$

where both the individual ψ_i and the coefficients c_i are not known. The energy of the *trial wavefunction* is given by Equation (2.4). The variation theorem states that the expectation value of the energy $\langle E \rangle$ of the trial function will always be an upper bound to the lowest energy eigenvalue of the system E_0, as given by Equation (2.5).

$$\langle E \rangle = \frac{\int \Phi^* \hat{\mathcal{H}} \Phi \mathrm{d}\tau}{\int \Phi^* \Phi \mathrm{d}\tau} \tag{2.4}$$

$$\frac{\int \Phi^* \hat{\mathcal{H}} \Phi d\tau}{\int \Phi^* \Phi d\tau} \geq E_0 \tag{2.5}$$

Equation (2.5) has powerful implications in QM. One of them being, in the search for the best wavefunction to define the ground state of a molecule, the quality of the wavefunctions can be judged by their associated energies. This result is critical because it means that the *trial wavefunction* does not have to be constructed as a linear combination of unknown wavefunctions. The quality of the *trial wavefunction* is then determined by how low a value is calculated for the integral in Equation (2.5). Furthermore, all the tools from calculus for locating local and global minima/maxima can be used to find the lowest possible energy within the constraints of how the wavefunction was constructed.

2.1.1 The Born-Oppenheimer approximation

Accurate wavefunctions for many-electron wavefunctions are difficult to express because of the correlated motions of particles. The correlation of motions of particles implies that no particle moves independently of all the others. This is expressed with the pairwise attraction and repulsion terms of the Hamiltonian in Equation (2.2). The Born-Oppenheimer approximation[134] can be invoked to simplify this complication. In common cases, the nuclei of molecular systems are moving at speeds much slower than those of electrons. This enables the approximation that the electronic 'relaxation' with respect to the nuclear motion is instantaneous. Therefore, the motion of the nuclei and the electrons can be decoupled, and electronic energies for fixed nuclear positions can be calculated. This means that the nuclear kinetic term is ignored, and the repulsive nuclear-nuclear potential energy term is evaluated as a constant. The new Hamiltonian includes only the first, third and fourth terms of Equation (2.2). Thus, the new SE, referred to as the *electronic* SE, is taken to be,

$$(\hat{\mathcal{H}}_{el} + \hat{V}_N)\psi_{el}(\boldsymbol{r}_i; \boldsymbol{r}_k) = (E_{el} + V_N)\psi_{el}(\boldsymbol{r}_i; \boldsymbol{r}_k) \tag{2.6}$$

where the subscript ‘el’ denotes electronic parts, V_N is the nuclear-nuclear repulsion term, and r_i *and* r_k are electronic and nuclear coordinates respectively. The Born-Oppenheimer model has profound consequences, one of them being the concept of a potential energy surface (PES). The PES is the surface defined by E_{el}, the eigenvalue of the *electronic* SE, over all possible nuclear coordinates, where the electronic coordinates parametrically depend on the nuclear coordinates. The full derivation of the Born-Oppenheimer model is more involved than showed here and can be found in standard texts.[135]

2.1.2 Many-electron wavefunctions

The next challenge involves the construction of the *trial wavefunction* and choosing the mathematical functions with which to construct this *trial wavefunction*. The wavefunction should consider the many-electron effects.

2.1.2.1 The Hartree-product wavefunction

A good place to start is to examine the electronic wavefunction a little more carefully. Since the full Hamiltonian (including electron repulsion) is not separable, an approximate Hamiltonian can be constructed where electrons do not interact. For such a Hamiltonian, a wavefunction that is constructed as a product of one-electron eigenfunctions, $\psi_{HP} = \psi_1\psi_2 \ldots \psi_N$ will be the eigenfunction. A wavefunction of this form is called a Hartree-product wavefunction. It can be shown, using the Hartree-product, that the energy eigenvalue of the many-electron wavefunction is simply the sum of the one-electron energy eigenvalues.[136]

2.1.2.2 Introducing spin and the anti-symmetry principle

A further step in approximating a many-electron wavefunction from one-electron orbitals is the theoretical introduction of electron spin. Spin is introduced as an additional coordinate of the electron, forming a *spin orbital.* The new one-electron wavefunction consists of a spatial orbital

and a spin function. For a system with a total number of two electrons of the same spin, the Hartree-product becomes,

$$\psi = \psi_a(1)\alpha(1)\psi_b(2)\alpha(2) \tag{2.7}$$

where α is a spin eigenfunction and a set of two spin eigenfunctions are orthonormal. However, the wavefunction defined by equation (2.7) is fundamentally flawed. From a feature of relativistic quantum field theory, electronic wavefunctions must change sign with an interchange of coordinates of two electrons.[137] Such a wavefunction is said to be anti-symmetric and its consequences are the Pauli exclusion principle, that no two electrons can occupy the same spatial orbital with the same spin. A modification of the Hartree-product wavefunction in Equation (2.7) can be made to invoke anti-symmetry as presented in equation (2.8).

$$\psi' = \frac{1}{\sqrt{2}}[\psi_a(1)\alpha(1)\psi_b(2)\alpha(2) - \psi_a(2)\alpha(2)\psi_b(1)\alpha(1)] \tag{2.8}$$

The Hartree-product wavefunction is now written as the difference of two spin orbitals. In general, the wavefunction of the electronic ground state of a system with N electrons can be approximated, with reasonable accuracy, by a single Slater determinant. This is enabled by the fact that an anti-symmetric wavefunction, consisting of a linear combination of N orbitals (and N electrons) can be conveniently written as a determinant. That is, a different mathematical form of Equation (2.8) is to write,

$$\psi_{SD} = \frac{1}{\sqrt{2}}\begin{vmatrix} \psi_a(1)\alpha(1) & \psi_b(1)\alpha(1) \\ \psi_a(2)\alpha(2) & \psi_b(2)\alpha(2) \end{vmatrix} \tag{2.9}$$

where the difference of MO products has been expressed as a determinant, and the 'SD' subscript stands for 'Slater determinant'. A generalized determinant for an N-electron system is as shown in Equation (2.10).

$$\psi_{SD} = \frac{1}{\sqrt{N}} \begin{vmatrix} \chi_1(1) & \chi_2(1) & \cdots & \chi_N(1) \\ \chi_1(2) & \chi_2(2) & \cdots & \chi_N(2) \\ \vdots & \vdots & \ddots & \vdots \\ \chi_1(N) & \chi_2(N) & \cdots & \chi_N(N) \end{vmatrix} \tag{2.10}$$

where N is the total number of electrons and χ is a spin orbital. The Slater determinant finds its usefulness in a number of interesting properties it possesses, one of them being manifestation of the indistinguishability of electrons. This follows from the fact that every electron appears in every spin orbital, somewhere in the expansion. This feature is violated in the Hartree-product wavefunction. One other feature of the Slater determinant, which is a direct consequence of the Pauli principle, is the so-called QM exchange. Moreover, the Slater determinant becomes zero when it contains two electrons with the same spin orbital. The subtle feature of QM exchange can be shown by considering the electron-electron interaction in the two-electron system, as shown by Equation (2.11).

$$\int \psi_{SD} \frac{1}{r_{12}} \psi_{SD} dr_1 d\omega_1 dr_2 d\omega_2 = J_{ab} - K_{ab} \tag{2.11}$$

where J_{ab} is the classical Coulomb repulsion between the electron clouds in orbitals *a* and *b* and it is reduced by K_{ab}.[138] In contrast, the wavefunctions formed from different spins do not have the exchange correlation integral K_{ab}. This result is derived from the orthogonality of spin eigenfunctions.

2.1.3 The LCAO approximation

To construct the wavefunction, the familiar hydrogenic atomic orbitals (eigenfunctions obtained when Equation (2.6) is solved exactly) can be used to construct more complicated MOs. In particular, a guess wavefunction as a linear combination of exact wavefunctions can be posited as a linear combination of atomic wavefunctions similar to Equation (2.3).

$$\Phi = \sum_{i=1}^{N} c_i \psi_i \tag{2.12}$$

In Equation (2.12), the set of N functions ψ_i, each with an associated coefficient c_i, is called the basis set. This construction of the *trial wavefunction* is referred to as the linear combination of atomic orbitals (LCAO) approximation. A linear combination of these basis functions is fixed for a calculation and it is chosen on a variety of theoretical and practical grounds. For example, Equation (2.12) does not contain information on the locations of the basis function. One would want the basis functions to be centred on the atoms of the molecules, but this is not a requirement.

2.2 The Hartree-Fock theory

A case of modelling a many-electron system by a single determinant is developed by the Hartree-Fock (HF) formalism. Optimization of the single determinant wavefunction involves the optimization of the spin-orbitals of which it is composed. The formalism in which these optimum spin-orbitals are determined is the HF theory. First developed by Hartree,[139] and improved by Fock,[140] the fundamental assumption of HF theory is that electrons experience an average static field due to other electrons. This assumption enables practical MO calculations but neglecting electron correlation can have significant chemical consequences when it comes to determining accurate wavefunctions.

HF formalism starts with the Slater determinant wavefunction being inserted as a wavefunction in the SE and the total energy derived. In linear algebra, there is a well-known theorem that the value of the determinant is unchanged by non-singular linear transformations among its rows and columns. That is, the spin orbitals of Equation (2.10) χ_i may be chosen to be an orthonormal set. A Lagrange multiplier ϵ_i can be introduced to impose the orthonormality of the set χ_i, and determine the turning points of the wavefunction ψ_{SD}. That is, minimize the energy with respect to orthonormal χ.

$$\frac{\delta}{\delta\chi}\left[\langle E\rangle - \sum_j \epsilon_j \int \left|\chi_j\right|^2 d\boldsymbol{r}\right] = 0 \tag{2.13}$$

There is a significant simplification of the expressions for the spin orbitals that results via variational calculus,[141] they are reduced to a set of one-electron equations that resemble single-particle SEs of the form,

$$\left(-\frac{1}{2}\nabla^2 + V_{ion}(\boldsymbol{r}) + U(\boldsymbol{r})\right)\chi_i(\boldsymbol{r}) = \epsilon_i\chi_i(\boldsymbol{r}) \tag{2.14}$$

where $U(\boldsymbol{r})$ is the non-local potential and V_{ion} is the local ionic potential. The full Hartree equation is given by Equation (2.15),

$$\begin{aligned}\epsilon_i\chi_i(\boldsymbol{r}) = \left(-\frac{1}{2}\nabla^2 + V_{ion}(\boldsymbol{r})\right)\chi_i(\boldsymbol{r}) + \sum_j \int d\boldsymbol{r}' \frac{\left|\chi_j(\boldsymbol{r}')\right|^2}{|\boldsymbol{r}-\boldsymbol{r}'|}\chi_i(\boldsymbol{r}) \\ - \sum_j \sigma_i\sigma_j \int d\boldsymbol{r}' \frac{\chi_j^*(\boldsymbol{r}')\chi_i(\boldsymbol{r}')}{|\boldsymbol{r}-\boldsymbol{r}'|}\chi_j(\boldsymbol{r})\end{aligned} \tag{2.15}$$

The first and second term on the right-hand side of Equation (2.15) are the kinetic energy and electron-nuclear potential contributions, respectively. The third term, also called the Hartree term, is the electrostatic potential arising from the charge distribution of N electrons. The third term includes an unphysical case of self-interaction, when *i=j*. However, this self-interaction case is cancelled in the fourth term, also called the exchange term. The exchange term exists because of an inclusion of the Pauli principle and the Slater determinant form of the wavefunction. The set of equations expressed in Equation (2.15) determine the best spin orbitals, for which ϵ_i attains its lowest value. This set is collectively called the HF equations.

2.2.1 Basis set expansion

Numerical solutions of the Hartree-Fock equations are usually found by expanding the orbitals in a basis set, similar to Equation (2.12).

$$\chi_i = \sum_k^N c_{ik}\phi_k \tag{2.16}$$

The HF orbitals, χ, are written in a basis set expansion of N known basis functions ϕ. Substituting Equation (2.16) into Equation (2.15) gives a set of matrix equations for the expansion coefficients, c_{ik}. The resulting HF equations can be solved by linear algebra techniques such as iterative diagonalization.[142] In practise, it is useful to choose basis set functional forms are easy to evaluate in a computationally efficient way. Efficiency involves keeping the total number of basis functions on a minimum. A larger basis set is an improvement over a smaller one, provided the evaluation of the greater number of integrals can be carried out faster. The basis functional forms chosen must make chemical sense. That is, the functions should have large amplitudes in regions of space where the electron density is also large.

2.2.2 Limitations of Hartree-Fock theory

In summary, HF theory is a simple theory which satisfies known features of the electronic wavefunctions – the HF product wavefunctions are antisymmetric with respect to the exchange of two electronic coordinates and they include exchange between like-spin electrons. HF calculations formally scale as N^3, where N is the number of basis functions. The extent to which HF can be used to predict properties of molecular systems is limited by its neglect of electron correlation. HF is then usually useful for determining qualitative information such as trends in structural parameters with system size, but ineffectual in predicting quantitative properties. This is seen with poor predictions of interaction energies. To make up for HF theory shortfalls, 'post-Hartree-Fock' (post-HF) methods, like density functional theory and perturbation theory exists. Density functional theory is said to scale three-dimensionally with the number of basis functions. *Ab initio*

methods like perturbation theory typically scale as fourth or higher of the number of basis functions included in the calculation.

2.3 Post-HF methods

Ab initio methods that use HF as a starting point and try to improve the HF results by taking into account electron correlation are collectively called post-HF methods. They include Configuration Interaction, Möller-Plesset (MP) Perturbation, and Coupled-Cluster. In this thesis, the MP method is used. The general principles of perturbation theory are based on simplifying operators that are difficult to work with, by removing their unwanted portions. Eigenfunctions and eigenvalues of the more complete operator are estimated by using the exact eigenfunctions and eigenvalues of the simplified operator.

Second order Möller-Plesset perturbation theory (MP2) method is a correlated *ab initio* molecular orbital approach which typically accounts for 80-90% of the correlation energy. It is the most economical method for incorporating electron correlation effects in *ab initio* electronic structure calculations; it is therefore the most widely employed method for benchmarking other quantum mechanical methods.[143–145] Generally, the MP2 method possesses greater accuracy compared to HF. For example, the MP2 method does well in describing non-bonded interactions (in both large and small systems) and internal conformational energetics[146,147]

2.4 Density Functional theory

Density functional theory (DFT) is distinct from QM methods like HF in that it uses a system of non-interacting electrons and does not yield a correlated N-body wavefunction. With QM methods, the Hamiltonian depends only on the nuclear positions, atomic numbers and the total number of electrons. The dependence on the total number of electrons enables the exploitation of electron density ρ, since, integrated all over space, density gives the total number of electrons. Moreover,

the information about the nuclear atomic numbers is also available from the density, since for a nucleus A located at an electron density maximum $\boldsymbol{r}_A$,

$$\left.\frac{\partial\bar{\rho}(r_A)}{\partial \mathrm{r_A}}\right|_{r=0} = -2Z_A\rho(\boldsymbol{r}_A) \tag{2.17}$$

where Z_A is the atomic number of nucleus A, r_A is the radial distance from A and $\bar{\rho}$ is the spherically averaged density.[148] With a known electron density, one can determine the external potential to form the Hamiltonian operator, and determine the wavefunctions and energy eigenvalues. There are formalisms that exist to predict the electron density of the system. Earlier approximations had to be improved to establish DFT as we know it today.[149,150]

2.4.1 Hohenberg-Kohn theorems

Hohenberg and Kohn (1964) were the first to prove two theorems that were critical in establishing DFT as a rigorous and legitimate QM methodology.[151] They proved that there is a one-to-one correspondence between the electron density of the system and the energy. The Hohenberg-Kohn (H-K) theorems are premised on a system consisting of electrons moving under the influence of an external potential V_{ext}. The first theorem is an existence theorem that states that the external potential, and hence the total energy, is a unique functional of the electron density. The energy functional $E[\rho(\mathbf{r})]$ referred to in the first H-K theorem can be written in terms of the external potential as shown by Equation (2.18),

$$E[\rho(\mathbf{r})] = \int \rho(\mathbf{r})\, V_{ext}(\boldsymbol{r}) d(\boldsymbol{r}) + F[\rho(\mathbf{r})] \tag{2.18}$$

where $F[\rho(\mathbf{r})]$ is an unknown universal functional of the electron density. The proof of this theorem proceeds by *reductio ad absurdum* and is available in standard texts.[129] The second H-K theorem is analogous to the variational principle in the wavefunction approach. It states that the ground-state energy can be obtained variationally. That is, the density that minimizes the total

energy is the ground-state density. The H-K theorems, however, did not offer a way of computing the ground-state energy of the system in practise.

2.4.2 Kohn-Sham equations

The Kohn-Sham (K-S) formalism was the key breakthrough that enabled DFT to be carried out practically.[152] By proposing to work with a fictitious non-interacting reference system, the challenge was to find the fictitious system of non-interacting electrons that has the same ground state density as the real system. From this notion, Kohn and Sham derived a coupled set of differential equation enabling the ground-state density to be found $\rho_0(\mathbf{r})$. As the exact density functional is not known, finding a good approximation to the energy functional is the goal of DFT. The universal functional $F[\rho(\mathbf{r})]$ in Equation (2.18) is divided into specific components that contribute to the total DFT energy,

$$F[\rho(\boldsymbol{r})] = T[\rho(\boldsymbol{r})] + J[\rho(\boldsymbol{r})] + E_{XC}[\rho(\boldsymbol{r})] \tag{2.19}$$

The energetic contributions to universal functional in equation (2.19) include the kinetic energy $T(\rho)$ of the non-interacting system, the classical Coulomb interaction $J(\rho)$, and the non-classical contributions due to self-interaction correction, exchange and the electron correlation effects, lumped together as $E_{XC}(\rho)$. Since the electrons are interacting, there is a difference between the exact kinetic energy and kinetic energy from assuming non-interacting orbitals. The exchange-correlation term is the part that remains after the non-interacting kinetic energy, the nuclear-electron interaction and the Coulomb interaction is subtracted. In other words, the exchange-correlation term is the functional that contains all that is unknown. It does not only contain contributions from self-interaction effects, exchange and correlation, but also a portion of kinetic energy unaccounted for by the non-interacting system. An involved task in K-S theory is then deriving approximations to the exchange-correlation functional only.

Another task that K-S theory is faced with is a prescription of how to uniquely determine orbitals in the non-interacting reference system. Essentially, one wants to define the effective potential

(potential in which non-interacting electrons move) such that it provides a Slater determinant which is characterized by the same density as the real system. The full K-S expression of the energy functional is shown in equation (2.20).

$$\begin{aligned} F[\rho(\boldsymbol{r})] &= T[\rho(\boldsymbol{r})] + J[\rho(\boldsymbol{r})] + E_{XC}[\rho(\boldsymbol{r})] + E_{ne}[\rho(\boldsymbol{r})] \\ &= T[\rho(\boldsymbol{r})] + \frac{1}{2}\iint \frac{\rho(\boldsymbol{r}_1)\rho(\boldsymbol{r}_2)}{r_{12}} d\boldsymbol{r}_1 d\boldsymbol{r}_2 + E_{XC}\,[\rho(\boldsymbol{r})] \\ &\qquad + \int \rho(\mathbf{r})\, V_{ext}(\boldsymbol{r}) d(\boldsymbol{r}) \\ &= -\frac{1}{2}\sum_{i}^{N} \langle \varphi_i | \nabla^2 | \varphi_i \rangle + \frac{1}{2}\sum_{i}^{N}\sum_{j}^{N} \iint |\varphi_i(\boldsymbol{r}_1)|^2 \frac{1}{r_{12}}\, |\varphi_i(\boldsymbol{r}_2)|^2 d\boldsymbol{r}_1 d\boldsymbol{r}_2 \\ &\qquad + E_{XC}[\rho(\boldsymbol{r})] - \sum_{i}^{N} \int \sum_{A}^{M} \frac{Z_A}{r_{1A}} |\varphi_i(\boldsymbol{r}_1)|^2 d\boldsymbol{r}_1 \end{aligned} \tag{2.20}$$

where E_{XC} is the only term that cannot explicitly be expressed. Equation (2.20) highlights the dependence of the energy expression on orbitals. The energy functional can be expressed in terms of orbitals since the non-interacting system of electrons can be treated using a scheme similar to HF theory. As in the HF scheme, the exact wavefunction of non-interacting electrons are Slater determinants. Thus, it is possible to set up a reference system with a Hamiltonian that contains an effective potential V_{eff} and does not contain an electron-electron interaction term,

$$\widehat{\mathcal{H}}_S = -\frac{1}{2}\sum_{i}^{N} \nabla^2 + V_{eff}(\boldsymbol{r}_i) \tag{2.21}$$

Accordingly, the wavefunctions of this Hamiltonian are represented by Slater determinants and spin orbitals, with the same form as Equation (2.11). In complete analogy to the HF equations of Equation (2.15), the spin orbitals are then determined by the usual eigenvalue problem of the form expressed in Equation (2.21), where the Hamiltonian is a one-electron K-S operator. The orbitals representing the density in K-S formalism are called K-S orbitals. The K-S orbitals establish the connection between the non-interacting reference system and the real system. As shown by Equation (2.22), V_{eff} is chosen such that the density ρ_{eff} that results from summing the square

moduli of the K-S orbitals exactly equals the ground state density of the real system of interacting electrons.

$$\rho_{eff}(\boldsymbol{r}) = \sum_{i}^{N} \sum_{s} |\varphi_i(\boldsymbol{r})|^2 = \rho_0(\boldsymbol{r}) \tag{2.22}$$

Note that equation (2.22) was substituted into the full energy functional to obtain equation (2.20). The energy expression of equation (2.20) can be minimized further under the constraint that the K-S orbitals remain orthonormal, to give the K-S one-electron equations.[153] These electronic equations can then be treated variationally, similarly to what is done in the HF scheme.

In summary, provided that the explicit form of V_{eff} (which exactly equals the sum of potential due to the nuclei, the classical Coulomb potential, and the potential generated by E_{XC}) is known, one-electron equations can be solved to obtain K-S orbitals. These orbitals will define the non-interacting system that has the same density as the ground state density as expressed in equation (2.22). Expressing the full energy functional in terms of density yields the exact ground state and therefore the ground state energy. In real-life applications, DFT is faced with a task of using approximations for the unknown exchange-correlation functional.

2.4.3 Exchange-correlation functionals

As already mentioned, E_{XC} not only accounts for the difference between non-classical and QM electron-electron interaction, but it also includes the difference in kinetic energy of the non-interacting system and the real system. The exact value of E_{XC} is generally unknown and is approximated by various exchange-correlation functionals. The difference between DFT methods is the choice of the functional form for the exchange-correlation energy. The accuracy of these density functionals are categorized in a hierarchy introduced by Perdew.[154] An analogy of Jacob's ladder is used, which ascends from the *Hartree-hell* to the *heaven of chemical accuracy.*[155] The ladder has five rungs, with each rung containing new physical content that is missing in lower rungs.

2.4.3.1 The local density approximation

The local density approximation (LDA) of the K-S formalism is one of the earliest density functional approximations. Functionals that only consider the local electron density are grouped on the first rung of Jacob's ladder. In LDA, the basis is the assumption that the electron density behaves like a uniform electron gas. A uniform electron gas is a system in which electrons move in a positive background charge distribution. An example of such a physical system is an idealized crystal of a metal with valence electrons and positive cores. The external potential of this non-interacting system is local. The potential is local in the sense that it is a function of only the spatial variable and is not dependent on the values of the effective potential at other positions in space. The LDA functionals perform well for systems with a slowly varying charge density or homogeneous systems, such as metallic solids. However, LDA tends to over-bind molecules and solids, which becomes exaggerated in weakly bonded systems.[156–158]

2.4.3.2 The general gradient approximation

For molecular systems with strongly varying electron density, an approximation solely based on the uniform electron gas introduces inaccuracies. The LDA functional can therefore be improved by including gradient corrections, making E_{XC} a functional of both density and its gradient. Gradient-corrected methods fall on the second rung of Jacob's ladder, as generalized gradient approximation methods (GGA). The most common and earliest GGA functionals include the PBE exchange-correlation functional developed by Perdew, Burke and Ernzerhof,[159] Bercke's B88 exchange functional,[160] and the LYP correlation functional by Lee, Yang and Parr.[161]

2.4.3.3 Other exchange-correlation functionals

Functionals on the higher rungs include meta-GGA methods, hyper-GGA methods (also called hybrid functionals) and generalized random phase methods. Meta-GGA functionals are also called higher order gradient methods. As the name suggests, they are an extension of GGA methods that allows the dependence of the exchange-correlation functionals on higher order derivatives of the

electron density. In particular, the Laplacian $\nabla^2\rho$ is the second-order term included in the functional. Alternatively, the functional can be taken to depend on the orbital kinetic energy which carries the same information as the Laplacian of the density. GGA and meta-GGA functionals are referred to as semi-local functionals, since they are evaluated based on both the local density and changes of the electron density in its proximity. The most common meta-GGA functional is the TPSS, developed by Tao and Perdew.[162]

The fourth rung of the ladder includes functionals like the popular B3LYP and PBE0. The general form of hyper-GGA methods are defined by writing the exchange-correlation energy as a combination of LDA, exact exchange (the non-local HF exchange evaluated using K-S orbitals), and a gradient corrected term. For example, the B3LYP functional contains 20% of HF exchange, 0.08% of LDA, 0.72% of B88 exchange and 0.81% of LYP correlation. Other popular hybrid functionals are the Minnesota functionals based on meta-GGA functionals. This class of functionals is extensively used in this work.

Functionals on the fifth and last rung of Jacob's ladder, employ the full information of K-S orbitals. In addition to occupied K-S orbitals used in hybrid functionals, virtual orbitals are adopted. Inclusion of these virtual orbitals significantly improves properties such as dispersion interactions.

2.5 Basis sets

A basis set is a set of mathematical functions that represent a wavefunction. As outlined in Section 2.1.3., each MO in HF theory is written as a linear combination of basis functions, the coefficients of which can be calculated from an iterative solution of HF equations.

2.5.1 Gaussian basis sets

Basis sets in QM calculations are usually expressed by atom-centred functions. There are two types of basis functions that can be used as atomic orbitals, Slater-type orbitals (STOs) and Gaussian-type orbitals (GTOs). STOs are attractive because of their close resemblance to hydrogenic atomic

orbitals. However, there is no analytical method available for general four-index integrals of HF equations. In principle, GTOs perform worse than STOs, but GTOs are easier to implement since the two-electron four-index integrals can be calculated analytically. Although GTOs provide a convenience from a computational standpoint, they have an exponential decay that is too rapid when they are compared to hydrogenic AOs.

2.5.1.1 Contracted Gaussians

The best features of GTOs and STOs can be combined to give what is referred to as contracted Gaussians (CGs). The computational efficiency of GTOs can be exploited, together with the proper radial functional shape of STOs, by using GTOs to build approximate STOs. The individual Gaussian function used in the linear combination of basis functions is referred to as the primitive Gaussians, defined by a contraction coefficient and an exponent. The degree of contraction of a Gaussian is judged by the number of primitive Gaussians in the basis set.

From a primitive Gaussian with optimal contraction coefficients and exponents, Pople's group[163] systematically studied a series of different basis sets of a varying number of basis functions. These different basis sets were termed STO-MGs, which means STOs approximated by an M number of primitive Gaussian functions used in the linear combination. They found that the optimum number of Gaussians that could be used in an efficient calculation is M=3, with STO-3G as the notation. This finding has consequently led to the STO-3G being defined for most of the atoms on the periodic table.

2.5.1.2 Single-ζ, multiple- ζ and split valence

The STO-3G basis set is rather unsatisfactory as it includes only one type of contracted Gaussian per AO, known as a single-ζ basis set. A single-ζ basis set is also called a minimal basis set, as it is the absolute minimum number of basis functions required. The flexibility of the basis set can be improved by 'de-contracting' it. Instead of one basis function per AO, two or three basis functions can be used, giving a double-ζ and a triple-ζ basis set respectively. Higher degrees of de-

contraction of the basis set creates higher multiple-ζ basis sets. Examples of such basis sets include the cc-pCVDZ and cc-pCVTZ, which are the extended forms of correlation-consistent polarized valence basis sets, treating core and core-valence correlation effects.[163]

Core orbitals are only slightly affected when chemical bonding occurs, whereas valence orbitals tend to vary more widely as a function of chemical bonding. What this means computationally is that core orbitals of the same atom in almost any molecule have very similar AO coefficients, and can therefore be described by using a minimal basis set. A 'split valence' basis set can be used to continue representing core orbitals by single (contracted) basis functions, while valence orbitals are split into many functions. Examples of split valence sets that are widely used are 3-21G and 6-311G. The notation contains information about the contraction scheme used for the split basis sets. The number before the hyphen indicates the number of primitive Gaussians used for core orbitals, while the numbers after the hyphen indicate the number of primitives Gaussians used for valence orbitals – two numbers specify a double-ζ basis set, while three number specify a triple-ζ basis set.

2.5.1.3 Polarisation and diffuse functions

Merely increasing the contracted Gaussians per AO does not result in quality basis sets. The basis sets still do not provide sufficient mathematical flexibility to satisfactorily describe the wavefunction for certain types of geometry. In addition, they do not allow the flexibility required in systems with extended electronic densities, such as in molecules with weakly bound electrons, anions and molecules forming hydrogen bonds. To redress these limitations and improve the description of the wavefunction, other types of contracted Gaussians are included. These are polarisation and diffuse functions.

Polarisation functions enhance the flexibility of atoms to form chemical bonds in any direction and therefore improve predictions of geometries of molecules. Polarisation functions are added in the form of basis functions corresponding to a quantum number of higher angular momentum than in the valence orbitals. A nomenclature scheme exists to indicate the inclusion of polarization

functions in the basis set, usually a '*' is added to the basis set. Thus, 6-31G* denotes d functions were added to polarize p functions. A "**" denotes p functions on H and He, like in the case of 6-311G**.[164] A more verbose nomenclature scheme is widely used instead of the star notation, to indicate the presence of polarization functions and allow for more explicit enumeration when more than one set of polarization functions are used. The 6-31G(d) notation is used instead of 6-31G*.

If a system at hand suggests that electron density might be found far from the nucleus, contracted Gaussians that extend further from the nucleus than the AOs are used. The standard basis sets are augmented with such diffuse functions. This improves the predicted properties with systems with extended electron density. Diffuse basis functions are of the same type as valence functions. Their presence is denoted by '+' in the basis set notation. A basis set containing both diffuse and polarization functions is considered 'balanced'.

2.5.2 Planewaves

The basis set that is used to solve the K-S equations is not only limited to Gaussian functional forms. There are many other functional forms that can be used depending on the type of system and problem studied. To address the periodicity of systems like crystals, a basis set that of functions that have the same periodicity as the lattice needs to be used. Planewaves (PWs) are usually used to capture the crystal structure description within DFT. To understand PW basis sets, it is worthwhile to go over the basic principles of crystal structure description.

2.5.2.1 Periodicity of crystal structures

Most solid materials that exist in nature are crystalline. This means they possess spatial periodicity or translation symmetry. A crystal lattice can be built from smaller building blocks called bases. A lattice is a set of points on which a basis can be attached to. Every basis will then be identical to every other one in composition, arrangement and even orientation. It is assumed that there are three non-coplanar vectors a_1, a_2 and a_3 that leave all the properties of the crystal invariant after

the crystal has undergone a shift by any of these vectors. As a result of this invariance after a translation, any lattice point $\boldsymbol{R'}$ can be obtained from another point as

$$\boldsymbol{R'} = \boldsymbol{R} + u_1\boldsymbol{a}_1 + u_2\boldsymbol{a}_2 + u_3\boldsymbol{a}_3 \tag{2.23}$$

where u_i are arbitrary integers. A lattice that is built up with a basis in this way is called a Bravais lattice. There is no unique way of choosing $\boldsymbol{a}_i$. The vector $\boldsymbol{a}_1$ is chosen as the shortest period of the lattice, $\boldsymbol{a}_2$ is chosen as as the shortest period not parallel to $\boldsymbol{a}_1$, and $\boldsymbol{a}_3$ is likewise chosen as the shortest period but perpendicular to both $\boldsymbol{a}_1$ and $\boldsymbol{a}_2$. Vectors chosen in such a way are called primitive and a volume enclosed in such a manner is called the primitive unit cell. There is no cell with a smaller volume $|\boldsymbol{a}_1.\boldsymbol{a}_2 \times \boldsymbol{a}_3|$ than the primitive unit cell.

2.5.2.2 Reciprocal space

As mentioned before, there is no unique way to choose $\boldsymbol{a}_i$, the lattice vectors and therefore no unique way to construct the elementary cell. Other ways exist to choose an elementary cell. Once can draw lines connecting a given lattice point to all neighbouring points, and then draw bisecting lines (or planes) to the previous lines. The smallest volume enclosed in this way is called the Wigner-Seitz primitive cell as shown in Figure (2.1), which is in 2D. This construction can be easily extended in 3D space, where the bisector lines will be planes instead of lines. The significance of the Wigner-Seitz cell is clear when considering the reciprocal space of the lattice. The construction of the Wigner-Seitz cell in reciprocal space is the first Brillouin zone. Brillouin zones are relevant as they are used to describe the behaviour of an electron in a perfect crystal such as describing and analysing the electronic band structure in crystalline solids.

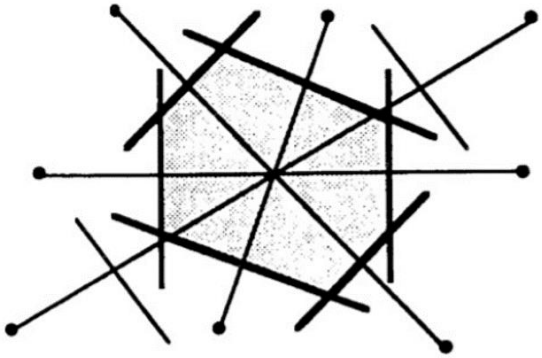

Figure 2.1 *The Wigner-Seitz primitive cell in 2D.*[165]

More relevant to crystallographers is the vivid geometrical interpretation that the first Brillouin zone provides for the diffraction condition. An x-ray beam in the crystal will be diffracted if its wavevector k has the magnitude and direction required by a specific diffraction condition derived from a geometrical interpretation in reciprocal space. Only waves whose wavevector k drawn from the origin terminates on a surface of the Brillouin zone can be diffracted by the crystal.[165] Since solid state physicists usually work in reciprocal space, the Brillouin zone can be constructed in reciprocal space. The real space and the reciprocal space are related to each other by a Fourier series. As an example, Figure (2.2) shows the Wigner-Seitz cell of the body-centred crystal (BCC) and the construction thereof in the reciprocal space.

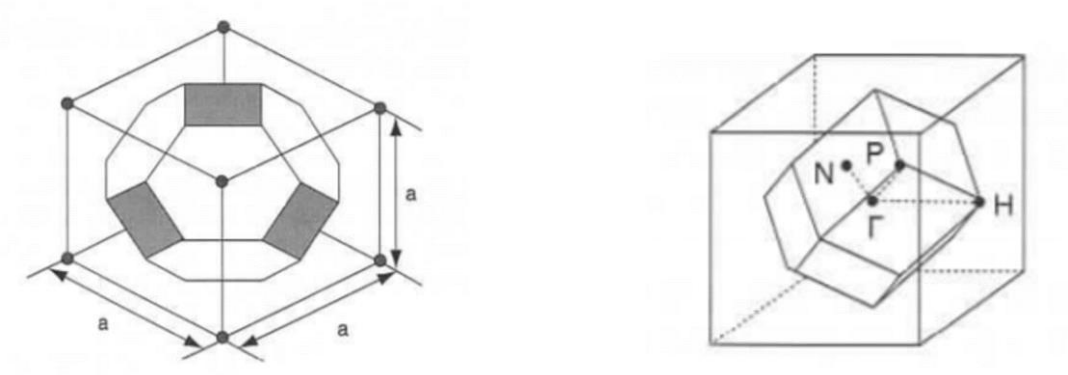

Figure 2.2 *The Wigner-Seitz cell of BCC (left) and the first Brillouin zone of BCC (right).*[166]

The reciprocal lattice vectors can be described as

$$\boldsymbol{G} = \nu_1 \boldsymbol{b}_1 + \nu_2 \boldsymbol{b}_2 + \nu_3 \boldsymbol{b}_3 \tag{2.24}$$

where $\boldsymbol{b_i}$ is related to the lattice vector in real space $\boldsymbol{a_i}$ by,

$$\boldsymbol{b_1} = 2\pi \frac{\boldsymbol{a}_2 \times \boldsymbol{a}_3}{\boldsymbol{a}_1 . \boldsymbol{a}_2 \times \boldsymbol{a}_3};\ \boldsymbol{b_2} = 2\pi \frac{\boldsymbol{a}_3 \times \boldsymbol{a}_1}{\boldsymbol{a}_1 . \boldsymbol{a}_2 \times \boldsymbol{a}_3};\ \boldsymbol{b_3} = 2\pi \frac{\boldsymbol{a}_1 \times \boldsymbol{a}_2}{\boldsymbol{a}_1 . \boldsymbol{a}_2 \times \boldsymbol{a}_3} \tag{2.25}$$

2.5.2.3 The periodic potential and Bloch's theorem

The periodic potential

In a perfect crystal, there exists an infinite number of interacting electrons moving in the static field of an infinite number of ions. Consequently, this poses two difficulties that need to be overcome. A wavefunction must be calculated for each of the infinite number of electrons and secondly, the basis set in which the wavefunction will be expressed will also be infinite. The ions in a perfect crystal are arranged in a regular periodic way. This also means that the external potential felt by the infinite number of electrons will also be periodic. This means that the external potential on an electron can be expressed as,

$$V(\boldsymbol{r}) = V(\boldsymbol{r} + \boldsymbol{R}) \tag{2.26}$$

Bloch's theorem

As mentioned before, this periodicity that exists in the perfect crystal creates an ideal situation for Fourier analysis and the use of Bloch's theorem which states that "energy eigenstates for an electron can be written as Bloch waves" (a type of wavefunction for a particle in a periodically-repeating environment like in a crystal). Using Bloch's theorem, the wavefunction of the infinite crystal can be expressed in terms of wavefunctions at reciprocal space vectors of a Bravais lattice. Therefore, each electronic wavefunction is written as a sum of planewaves (PWs). The wavefunction is expressed as a product of a cell periodic part and a wavelike part,

$$\psi_{i,k}(\boldsymbol{r}) = e^{i\boldsymbol{k}\boldsymbol{r}} f_i(\boldsymbol{r}) \tag{2.27}$$

where ψ_i is the one-electron wavefunction of the *i*th electron and **k** is the wave vector in reciprocal space. The first part and second part are the wavelike and cell periodic part of the wavefunction respectively. The cell periodic part of the wavefunction can be expanded into a finite number of PWs whose wave vectors are the reciprocal lattice vectors of the crystal as shown in Equation (2.28).

$$f_i(\boldsymbol{r}) = \sum_{\boldsymbol{G}} c_{i,\boldsymbol{G}} e^{i\boldsymbol{G}.\boldsymbol{r}} \tag{2.28}$$

where $\boldsymbol{G}$ is the reciprocal lattice vector. The wavefunction can then be written as a sum of finite PW as shown in Equation (2.29).

$$\psi_i(\boldsymbol{r}) = \sum_{\boldsymbol{G}} c_{i,\boldsymbol{k}+\boldsymbol{G}} e^{i\boldsymbol{G}.\boldsymbol{r}}\, e^{\{i(\boldsymbol{k}+\boldsymbol{G}).\boldsymbol{r}} \tag{2.29}$$

Using Bloch's theorem has shifted the problem of the infinite number of electrons to the problem of expressing the wavefunction in terms of an infinite number of reciprocal space vectors. The reciprocal vectors exist in the first Brillouin zone, **k**.

Sampling the Brillouin zone

However, there is still a problem. The Brillouin zone can now be mapped out by a set of k-points, throughout that region of reciprocal space (k-space). There are an infinite number of k-points in the k-space since the occupied states at each k-point contribute to the electronic potential of the bulk solid. Furthermore, the wavefunction needs to be calculated at each k-point. This means the basis set to calculate the wavefunction is infinite. To overcome this difficulty, electronic wavefunctions are only calculated at a uniquely chosen set of k-points. This is possible because electronic wavefunctions at k-points that are very close to each other will be almost identical. Consequently, it possible to represent the electronic wavefunctions over a region of reciprocal space at a single k-point. This approximation allows the electronic potential to be calculated at a finite number of k-points and hence determine the total energy of the solid.

2.5.2.4 Planewave calculations

As described in the previous section, in a PW calculation, the electronic wavefunction is expanded using a PW basis set according to Equation (2.29). There are a number of approximations and simplifications involved to implement the PW basis set numerically.

The cut-off energy

One of the most important parameters that determine the accuracy and the computational cost of a PW calculation is the cut-off energy, E_{cut}. The coefficients for the PWs, $c_{i,\boldsymbol{k+G}}$, each have a certain kinetic energy. PWs with a smaller kinetic energy typically have a more significant role than those with a very high kinetic energy. The introduction of E_{cut} reduces the size of the basis set by excluding PWs with very high energies. The E_{cut} for a particular system can be obtained by performing convergence tests that involve increasing it until the result stops changing.

Pseudopotential

The use of Bloch's theorem, the planewave cut-off energy in the Fourier expansion of the wave function and the careful k-point sampling has allowed the solution to the Kohn-Sham equations for infinite crystalline systems easy to deal with. However, a PW basis set is a poor choice for expanding the electronic wavefunction because a large number of functions is required to accurately describe electrons in the core region. In the core region, electrons oscillate rapidly. The rapid oscillations happen because the potential is very attractive near the nucleus and the strongest potentials result near the nucleus. A poorly suited basis set means that high-frequency Fourier components require very high energy planewave cut-offs. However, the wavefunctions near the nuclei do not affect the chemical, mechanical or electronic properties much. The Coulomb potential near each nucleus can therefore be replaced with a modified, weaker and smoother potential. This modified potential is called a pseudopotential.

The motivation for the pseudopotential method is based on the fact that in almost any molecular system, there exists a set of core orbitals that do not significantly affect the chemical, mechanical or electronic properties of the molecule, as mentioned before. In addition, the behaviour of the

valence electrons are mainly due to the Pauli exclusion principle. Figure (2.3) shows a valence wavefunction of a typical molecular system.

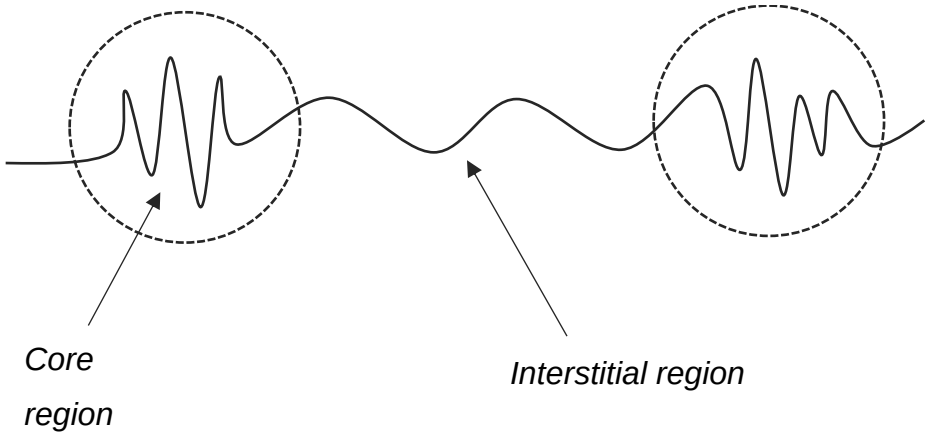

Figure 2.3 *A representation of a valence wavefunction in a typical molecular system.*

The valence wavefunction are divided into two regions, the atomic sphere and the interstitial sphere. In the pseudopotential approximation, the core electrons are removed and the Pauli exclusion enforced via a repulsive pseudopotential. This removes the oscillations in the interstitial region, as shown in Figure (2.4), and allows the efficient application of planewave basis set expansion.

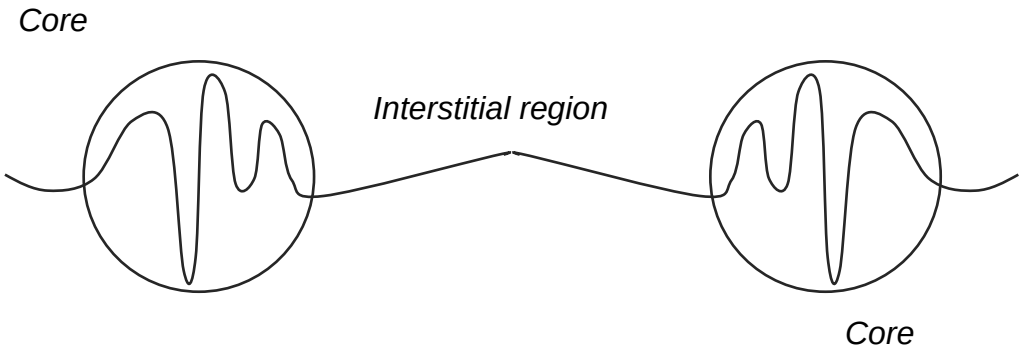

Figure 2.4 *A representation of the valence wavefunction where the strong ionic potential is replaced by a weak and smoother pseudopotential.*

Pseudopotentials allows the concentration to be shifted to the valence electrons, reducing the number of states needed in the SE. All PW calculations are used in combination with a pseudopotential.

2.6 Continuum solvation models

2.6.1 Explicit solvation models

Most of chemistry occurs in solution and therefore solvation effects are often crucial. In this work, a simple approach of an implicit treatment of the solution environment is employed. Alternatively, an explicit treatment of solvation involves modelling solvent molecules by explicitly placing them around the solute. However, this is not a true and complete picture of solvation – one needs to consider, for example, the interaction of the solvent molecules with the second solvation shell. Many solvation shells would need to be included to complete the picture, which equals hundreds of thousands of solvent molecules. A QM calculation of this enormous system size would be very expensive. In addition, accounting for many possible minima, one needs to compute statistical mechanical averages to determine equilibrium properties.

2.6.2 The implicit treatment of solvation

To counter this expensive approach, one can remove the individual solvent molecules and in turn modify the space those molecules occupied so that it has properties that are consistent with those of the solvent. To define such a medium, continuous solvation models have been developed.[167–169] Continuum solvation models, also called implicit solvation models, represent a solvated molecule inside a molecule-sized electrostatic cavity, surrounded by a dielectric medium representing the solvent. The dielectric medium is associated with a relative permittivity, which can be equated to the static dielectric constant of the bulk solvent outside the electrostatic cavity. The solute can be modelled as polarizable and quantum mechanical – where the charge distribution of the solute polarizes the surrounding dielectric medium. The electric potential due to this polarized dielectric

continuum and the polarization of the solute is called the reaction field, which is defined as the difference between total potential and the potential of the solute with the same charge distribution as in vacuum. Since the electric potential obeys the non-homogeneous Poisson equation, the reaction field can be determined by self-consistently solving the Poisson equation via numerical integration.

The continuum solvation model relies on the non-homogeneous Poisson equation of classical electrostatics, which expresses the electrostatic potential as a function of the electronic charge density and the dielectric constant as shown by Equation (2.30).[129]

$$\nabla^2\phi(\boldsymbol{r}) = -\frac{4\pi\rho(\boldsymbol{r})}{\epsilon} \tag{2.30}$$

where ϵ is the dielectric constant of the dielectric medium. Equation (30) is valid in cases where the surrounding dielectric environment responds linearly to the embedding of charge. Since the explicitly treated solute molecule forms a cavity inside the homogeneous dielectric medium, there are essentially two regions, one inside and one outside the cavity. Equation (2.30) can then be properly formulated as,

$$\nabla\epsilon(\boldsymbol{r}).\nabla\phi(\boldsymbol{r}) = -4\pi\rho(\boldsymbol{r}) \tag{2.31}$$

Density-based solvation models (those that use continuous charge density) are employed to solve the non-homogeneous Poisson equation. An example of such a model is the polarizable continuum model (PCM), which includes the integral-equation-formalism (IEF-PCM) as one of its various PCM formalism.[170] In this work, a variation of IEF-PCM, SMD,[171] is used to study changes of potential energy surfaces upon solvation. It involves a QM treatment of the charge density of the solute molecule interacting with its surrounding medium. The 'D' in SMD stands for 'density', and it indicates that the solute electron density is used as opposed to defining partial atomic charges. The SMD model is a universal solvation model; it can be applied to any medium for which a few relevant macroscopic descriptors (such as the dielectric constant and refractive index) are known.

2.6.3 Limitations of implicit solvation model

In an attempt to remove difficulties associated with modelling large number of solute molecules across an entire configuration space, continuum models lose molecular-model detail. The correct description of the molecular structure of the solvent is lost with the assumption that electrostatic interaction of the solute and its surrounding medium does not depend on a correct description. This assumption particularly becomes a limitation when strong, specific interactions between the solute molecule and solvation shells need to be considered. Therefore, directional interactions such as hydrogen bonding, π-π stacking interactions, and monoatomic ions, are not addressed.

3

Computational studies into the use of fluorination to control the conformational and dynamic behaviour of Metal-Organic Framework linkers

One permanent issue in quantum chemistry is that there are many different approximations to the SE. It is imperative that the most appropriate computational chemistry method is chosen for modelling MOF linkers and ultimately truncated MOF structures. One needs to aim for reliable results and one way of choosing the best method is considering methods that give optimized geometries that are the closest to experimental geometries.[172] Experimental data with which one can validate computational data is not always available. Therefore, benchmarking QM methods with another reliable QM method can be done. The benchmark is usually a highly accurate, but expensive method.

In this chapter, a comprehensive study on isolated MOF linkers is performed in order to investigate the effect of *vicinal* fluorination on their conformations. In addition, the influence of the dielectric environment on the conformations is also investigated. Initially, reference studies are performed on 2,3-difluorobutane. These reference studies are performed by closely following a computational study (validated by experimental data) by Fox *et al.*[173] A comparative assessment of various DFT functionals, used in the computational study, is carried out by using the MP2 method as a benchmark. The accuracy of and variance within functionals will be quantified by mean absolute errors (MAEs) of relative energies of 2,3-difluorobutame low-energy conformers. The purpose of the reference studies on 2,3-difluorobutane is an attempt to identify a suitable DFT functional for further studies on MOF linkers and MOF structures themselves. DFT functionals that will be

employed in the study include some of the Minnesota functionals (M05, M05-2X, M06, M06-2X), PBE and PBE0.

3.1 Computational details

All calculations in this chapter were carried out by using the Gaussian 09 E.01 program package[174] unless stated otherwise. The molecular structures were built within GaussView and then subjected to different calculations run on the Centre for High Performance Computing (CHPC) cluster and the Scientific Computing Research Unit (SCRU) cluster.

DFT calculations were performed by employing the M05, M05-2X, M06 and M06-2X PBE and PBE0 exchange-correlation functionals, using the 6-311+G(d,p) basis set as in the Fox *et al.* paper. The MP2 method was used as a benchmark for the DFT calculations. All solvation-related calculations for 2,3-difluorobutane diastereomers were performed *in vacuo* and various solvents with dielectric constants in the range 1.5-78.54. The universal SMD model was used for calculations in solvents. To generate a full rotational profile of the structures, a conformational sweep of the C-C-C-C dihedral angle was performed, sampling every ten degrees. The dihedral angle was constrained while the rest of the molecule could relax. To ensure accuracy, the low-energy conformers as in Figure (3.1), were geometrically optimized with no structural constraints to obtain the true energy. The low-energy conformer structures from the rotational profiles were used as starting points when calculating these true energies. It is the energy from these geometrically optimized structures that were used to compute relative energies of low-energy conformers. Energies of low-energy conformers were also obtained in a similar manner.

To study the effect of a *vicinal* fluorination motif on conformational flexibility, an angular range around the respective minima was considered for butane, butene and the diastereomers of 2,3-difluorobutane, sampling every degree, to provide a more refined sweep. Force constant were then obtained from fitted curves around the respective minima.

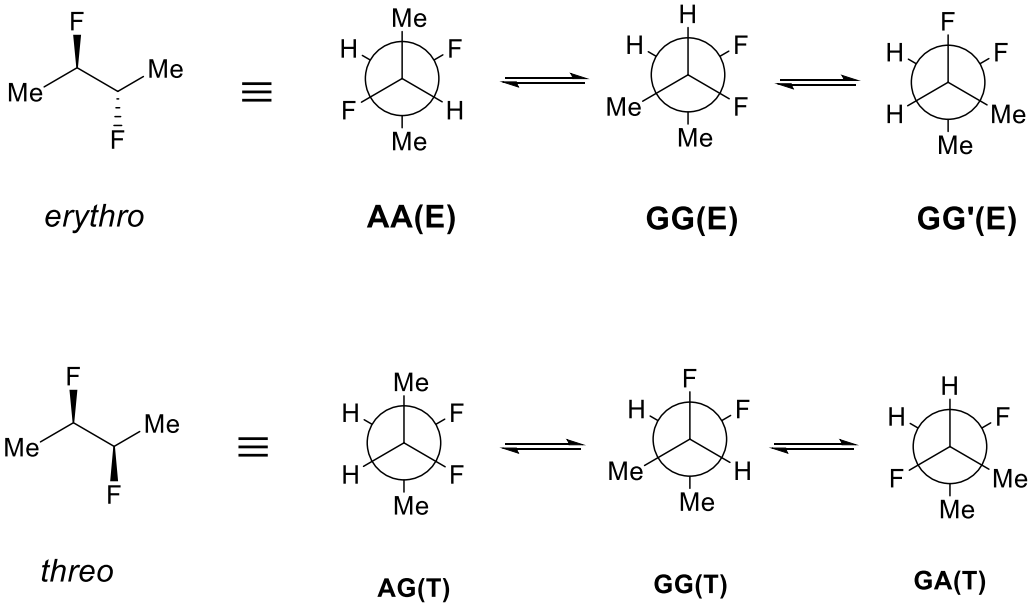

Figure 3.1 *The low-energy conformers of 2,3-difluorobutane with their corresponding labels. The 'A' and 'G' in the labels refer to the geometry of the methyl groups and the fluorine atoms. The geometry of the methyl groups is mentioned first followed by that of the fluorine atoms. 'A' denotes anti and 'G' denotes gauche.*

To complement the calculations performed previously, Natural Bond Analysis (NBO) analysis[175] available in Gaussian E.01 was used. NBO allowed to address the hyperconjugation interactions in the low-energy conformations to better comprehend the adopted conformations observed.[14] In addition, NBO analysis was also useful for evaluating the strength of interactions. NBO analysis was performed on 2,3-difluorobutane to gain more insight on the extent of the fluorine *gauche* effect on conformational control. Similar calculations and analysis performed on 2,3-difluorobutane were also performed 2,3-difluorosuccinic acid, 2,3-difluorosuccinate and 1,2-difluoro-1,2-di(pyridin-4-yl)ethane MOF ligands.

3.2 Reference studies on 2,3-difluorobutane

3.2.1 The effect of the functional on relative energies of low-energy conformers

Figure (3.2) is a bar graph representing relative energies of 2,3-difluorobutane conformers, *in vacuo* (ε_r= 0) and in water (the environment with the largest dielectric constant, ε_r=78.54), calculated using various DFT functionals and the MP2 method. Appendix I shows bar graphs representing relative energies calculated in all solvent using various DFT functionals and the MP2 method.

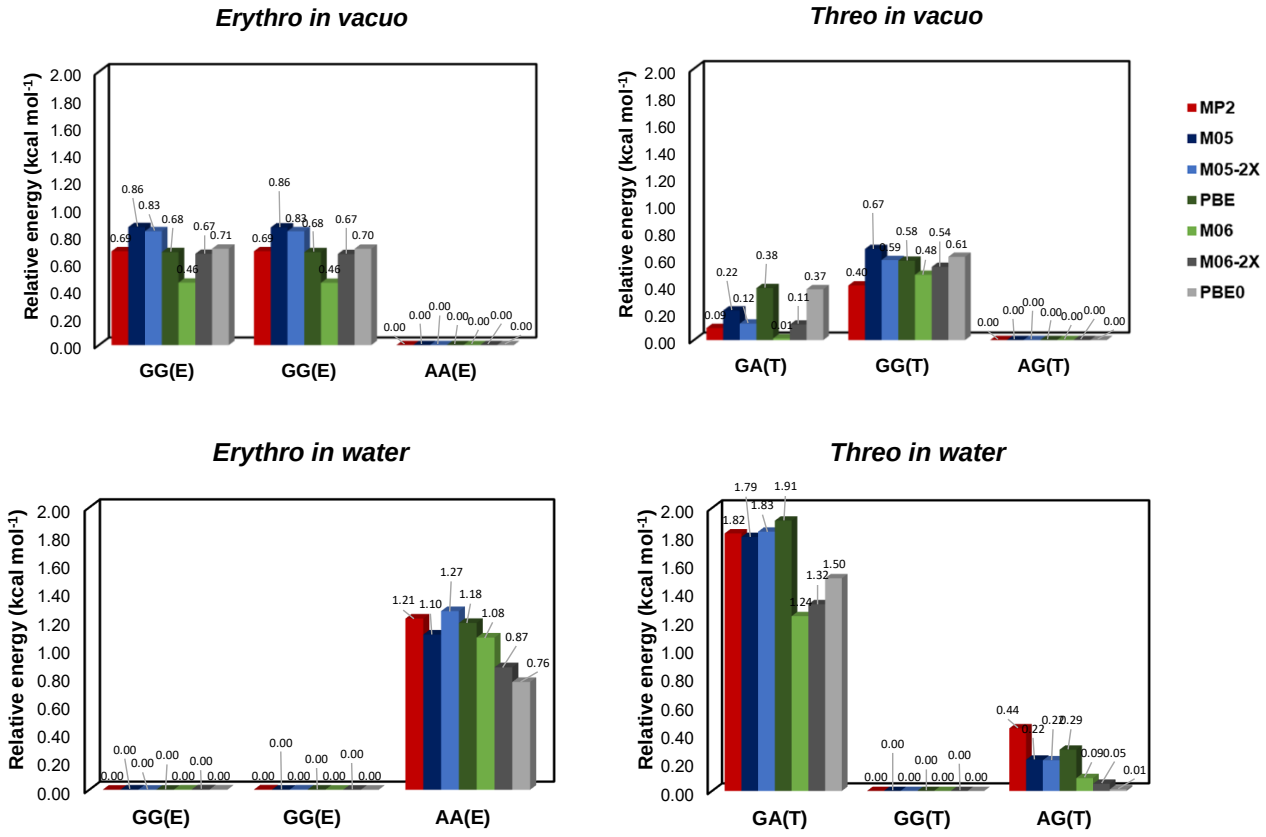

Figure 3.2 *The relative conformational energies of threo and erythro-2,3-difluorobutane low-energy conformers in water (a), (b) and in vacuo (c),(d) using various density functionals and the MP2 method.*

The general trend of relative energies of conformations seen with MP2 (red) can also be seen for all the DFT functionals. That is, for the *threo* diastereomer conformers, the GG(T) conformer has the lowest energy for all the functionals whilst the GA(T) conformer has the highest energy in solvent. For the *erythro* diastereomer *in vacuo*, the degenerate GG(E) conformer is the least stable conformation. This holds for all functionals in all solvents. *In vacuo*, both conformers that have the methyl groups in *antiperiplanar* position are lower in energy than conformers with the methyl groups in *gauche* position, with the AA(E) conformer being the most stable structure overall. Variances of the relative energies observed can be quantified.

3.2.2 Error analysis of DFT functionals

Variance within the functionals was quantified by a comparative assessment against MP2, as benchmark. Relative energies of low-energy conformers were compared from calculations with each functional. The calculations were done *in vacuo* and various solvents and compared with those obtained using the MP2 method. Appendix II shows the results.

What is immediately apparent is that M06, M06-2X and PBE0, having the highest MAEs of 0.13-0.14 kcal mol^{-1}, show the largest discrepancy to MP2. M05, M05-2X and PBE show the smallest discrepancies with MAEs of 0.05-0.07 kcal mol^{-1}. The M05 and M06 functionals show similar performances. Inclusion of exact exchange in the functional therefore has minimal effect on improvement in accuracy. In addition to the percent errors, understanding of the construction of the functional can help identify a suitable functional for the chemical system under study. Furthermore, consulting literature on the types of chemical systems that the functional has been employed for can also be helpful. For example, both the Minnesota and PBE-related functionals are gradient-corrected functionals. However, the Minnesota functionals achieve the inclusion of gradient corrections by introducing experimentally fitted parameters, whereas the PBE functionals introduce non-empirical parameters. This makes the latter, in principle, valid for a wider range of systems. Nazarian *et al.* used a test set of diverse MOFs to benchmark the performance of various DFT functionals, which included a Minnesota functional (M06-L[176]) and functionals based on PBE.[177] They showed that some PBE-related functionals predicted lower deviations from

experiment in the description of structure. This result is important when experimental crystal structures are geometrically optimized and used for further studies. Therefore, the choice of a suitable functional would be between M05, M05-2X and PBE functionals. The more widely employable PBE functional will be used for further reference studies of 2,3-difluorobutane and larger scale calculations. Furthermore, the PBE functional has been used for chemical systems containing transition metals, which is important in the case of MOFs.

3.2.3 Rotational profiles of 2,3-difluorobutane

3.2.3.1 Low-energy conformers

Figures (3.3a) and (3.3b) shows the rotational energy profiles from the PBE calculations done *in vacuo* (top) and water (bottom) for the *threo* and *erythro* diastereomers of 2,3-difluorobutane, with a representation of the relative conformational energies of low-energy conformers in Figures (3.3c) and (3.3d). Only the rotational profile of water is currently presented as it has the highest dielectric constant, and thus more significant energetic effects. Conformational energies for the other solvents are be presented later.

The rotational energy profile in water, is significantly different from that *in vacuo*. Surprisingly, the AA(E) conformer now has a higher relative conformational energy than the GG(T) conformer. This is despite the minimized steric interactions due to *antiperiplanar* methyl groups in AA(E). Moreover, in the GG(T) conformer, steric interactions are maximized by the methyl groups being in the *gauche* position. Another interesting observation is that in water, conformers with the fluorine atoms in *gauche* position have higher relative energies than those that do not. To elucidate the relative conformational stability observed, NBO analysis will be utilized, as mentioned before, to quantify energetic contributions.

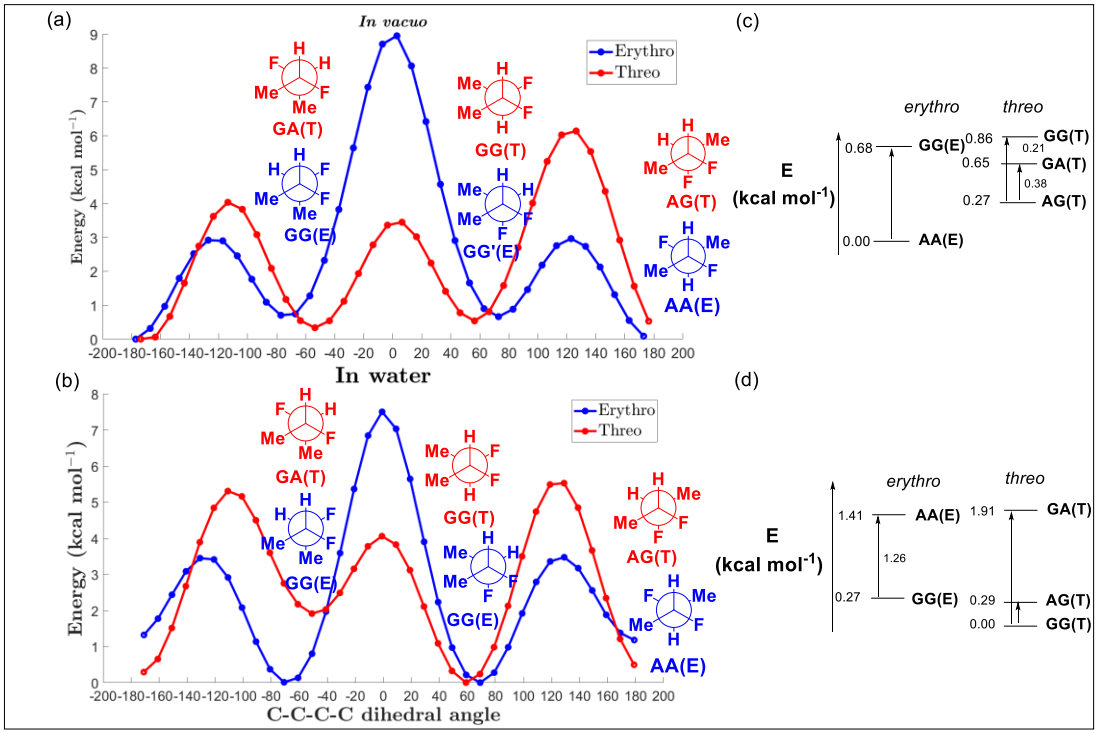

Figure 3.3 *Rotational profiles of* **threo***-2,3-difluorobutane (red) and* **erythro***-2,3-difluorobutane (blue) (a) in vacuo and (b) in water, calculated at a PBE/6-311+G(d,p) level of theory. Threo and erythro energies are relative to the global minimum. (c) and (d) is a representation of the relative conformational energies of low-energy conformations.*

Figure (3.4) shows a representation of the relative conformational energies of low-energy conformations in acetone and chloroform (water and vacuum included for clarity). The rotational energy profiles in acetone and chloroform obtained using PBE are qualitatively similar to that in water. The GG(T) conformer remains the global minimum structure in both acetone and chloroform, and the GA(T) conformer remains the structure with the highest relative energy. The conformers between these two extremes are still at the same relative positions.

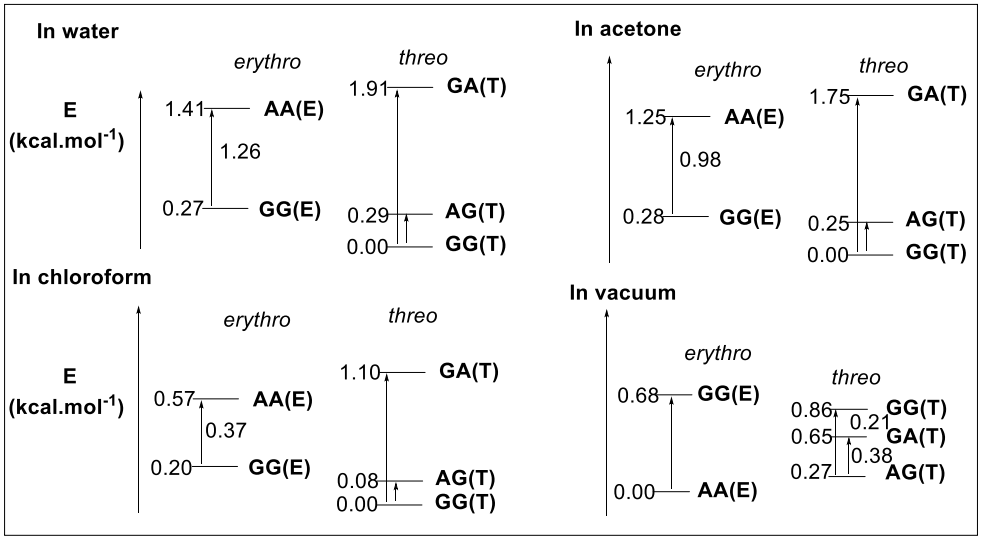

Figure 3.4 *A representation of the relative conformational energies of low-energy conformations in vacuo and in water, acetone and chloroform.*

There are larger relative conformational energy differences between conformations in acetone compared to those in chloroform. For example, the energy difference between the two *erythro* conformations is 0.98 kcal mol^{-1} and 0.37 kcal mol^{-1} in acetone and chloroform, respectively. The relative conformational energy differences between the global maximum and the global minimum in acetone and chloroform are 1.75 kcal mol^{-1} and 1.10 kcal mol^{-1}, respectively.

3.2.3.2 High-energy conformers

To gain further insight into the dynamic behaviour of 2,3-difluorobutane, it is worth looking at the high-energy eclipsed conformers, with methane groups and fluorine atoms eclipsed. Figure (3.5) shows the high-energy structures of 2,3-difluorobutane, as well as their relative energies *in vacuo* and solvent.

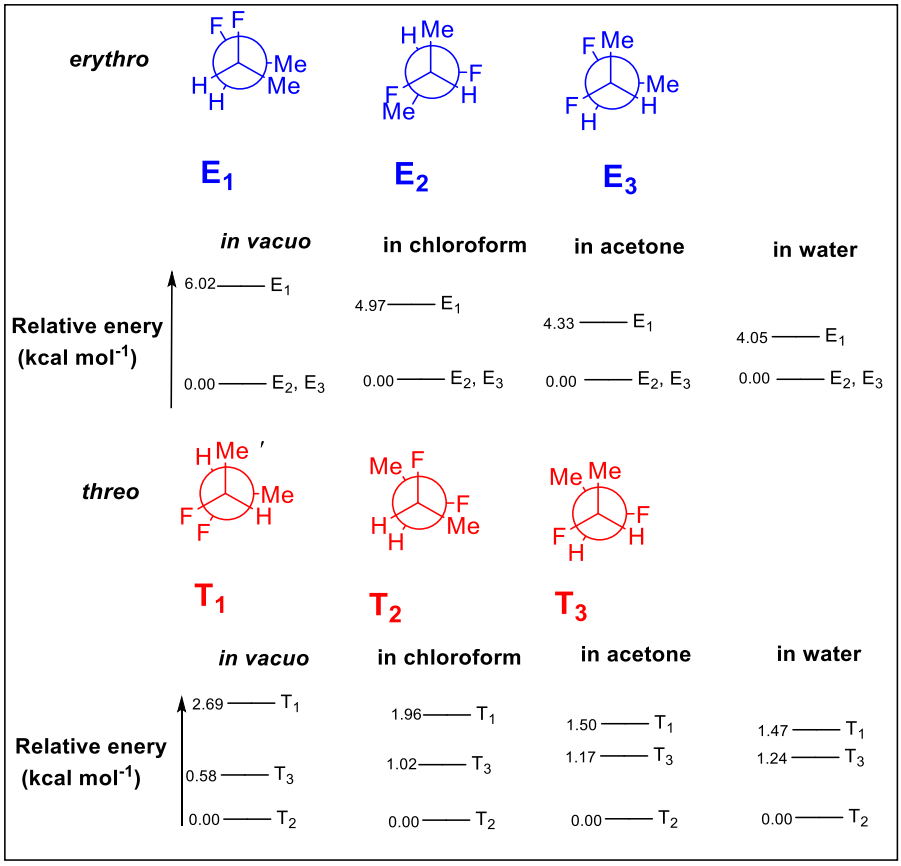

Figure 3.5 *High-energy conformers of erythro (top) and threo-2,3-difluorobutane (bottom) in vacuo and in solvent.*

For the *erythro* isomer *in vacuo* and solvent, the conformer with the highest relative energy, E_1, has both the fluorine atoms and the methyl groups eclipsed (eclipsed C-F/C-F and C-Me/C-Me bonds), maximizing steric interactions. This result persists in all solvents, with the relative energies of E_1 decreasing with an increasing solvent polarity. That is, increasing the solvent polarity lowers the energy barrier of conformations with low relative energies in solvent, particularly GG(E) for the *erythro* diastereomer and GG(T) and AG(T) for the *threo* diastereomer. This is consistent with the fact that upon a 30° rotation of the C-C-C-C dihedral angle of the E_1 (and E_3) conformer, the GG(E) conformer results. For the *threo* isomer, only the energy barrier to the T_2 conformer is lowered, while the energy barrier to the T_3 structure is raised. A 30° rotation of the C-C-C-C dihedral angle of the T_2 structure leads to the AG(T) conformer. Similarly, a 30° rotation of the T_2 dihedral angle leads to the GA(T) conformer, which has the least relative conformational energy

in solution. It is then established that solvent polarity can control the energy barriers of conformations. Just in the Fox *et al.* paper, an interesting observation is made that the eclipsed C-F/C-F bonds is more destabilizing than the eclipsed C-Me/C-Me bonds for the *threo* high-energy structures. This is reflected by the T_1 conformer having higher relative conformational energy than the T_3 conformer. To gain chemical insight on the low-energy and high-energy conformers observed, effects of solvent polarity on solvation free energy, polarizability and dipole moment will be addressed in Section (3.2.4).

3.2.4 Effect of solvent polarity on conformational control

The discrepancies observed within different solvents can be analysed on a qualitative level. Investigating solvation effects in this case, will lead to a clearer understanding of the influence of the dielectric environment on the conformations of framework linkers. Typically, one conformer can be found to be predominant in one medium and not the other. An established guiding rule is that the conformer of higher dipole moment is more favoured in media of higher relative permittivity.[178] The solvent with the largest dielectric constant is therefore expected to have the largest population of the more polar conformers. Relative permittivity describes the ability to polarize a medium subjected to an electric field. The source of the polarization can be electronic, atomic, dipolar or ionic in nature.

3.2.4.1 Solute interactions

As a consequence of conformational flexibility of 2,3-difluorobutane, substantial changes in polarity effects can be expected. The effect of solvent polarity on molecular dipole moments of the low-energy conformations can be explored. Appendix III shows the molecular dipole moments of the low-energy conformers in different solvents using the PBE functional.

For conformations *in vacuo,* the lowest energy AA(E) conformer has an overall molecular dipole moment of 0.00 D and the GG(T) conformer has the largest dipole moment of 3.47 D. The result

of the AA(E) conformer having the least energy is consistent with the fact that polar conformations are unable to be stabilized in the gas phase or in non-polar solvents.

In solvent, the strength of solute interactions is dependent on the size of the dipole moment of the conformer (the solute) and the dielectric field. In all solvents, the global minimum structure, GG(T), has the highest dipole moment, with the GG(E) conformer having the second highest dipole moment. Conformers that have the fluorine atoms in the *gauche* position have relatively large molecular dipole moments and are therefore more stabilized in solution. In addition to their stabilizing solute interactions, they are expected to also have hyperconjugation interactions that further stabilize them. The AA(E) conformer has the highest relative conformational energy in all solvents, which is consistent with the fact that it has the smallest dipole moment and therefore no stabilizing solute interactions in polar solvents. Although the GG(E) conformer has a larger dipole moment than the AG(T), it does not have a lower relative conformational energy. The GG(E) conformer has the methyl groups in the *gauche* position, which lowers its energy.

The GG(T) conformer has a larger dipole moment (albeit only slightly larger) than the GG(E) conformer. To gain insight into this, electronegativities and positions of the atoms that are part of the molecule can be used as a guide to estimate the polarity of involved bonds and the direction of their dipole moments. Figure (3.6) shows a simplified vector analysis for 2,3-difluorobutane using the bond dipole moment vectors associated with the C-F bond and C-H bond. The bond dipole of C-Me is ignored since the C-C bond is nonpolar. Furthermore, the C-F bonds contribute more to the total dipole moment than the C-H bonds. The total dipole moment is then estimated from a vector sum of the individual bonds and depends both on the magnitude and the relative orientation of each bond dipole.

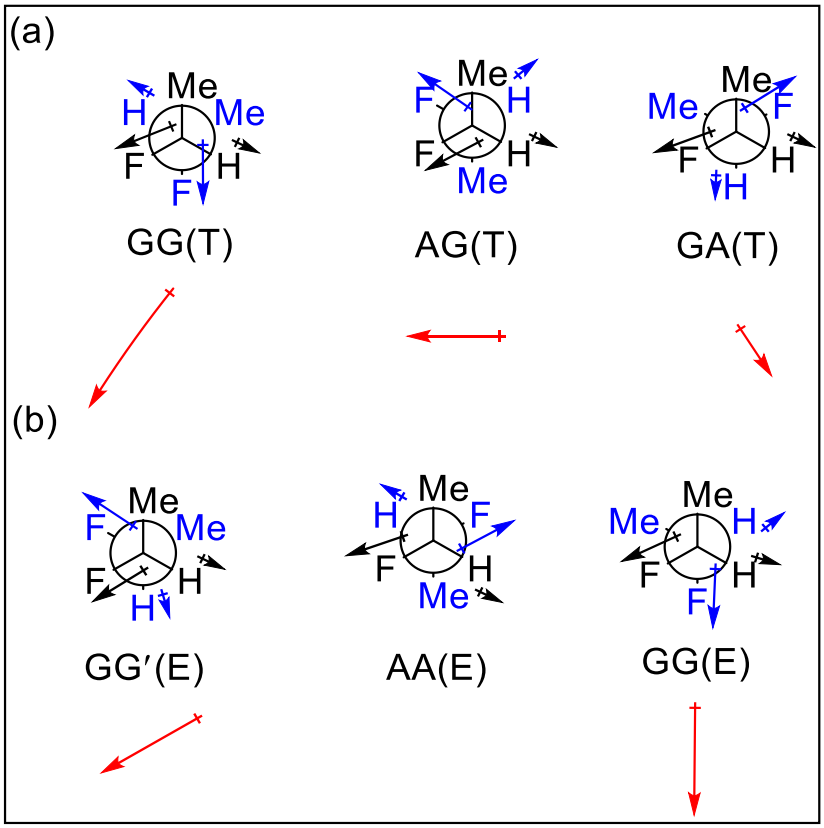

Figure 3.6 *The dipole moment vectors associated with the bond dipoles (blue and black) and the overall estimated molecular dipole (red) of 2,3-dilfuorobutane in the (a) threo isomer (b) erythro isomer.*

The simple vector analysis explains why the GG(E) and GG(T) conformers have similar dipole moments, with the magnitude of the GG(T) slightly larger. The GG(T) conformer has C-H bonds that oppose each other, and therefore their C-H bond dipoles cancel each other. The GG(E) conformer, on the other hand, has C-H bond dipole moments to add to the total dipole. The addition of the C-H bond dipole moments has an overall effect of a smaller total dipole moment, since they are facing away from the C-F bond dipole moments. As a result, GG(T) conformer has a slightly larger total dipole moment. These results are consistent with the calculated dipole moment.

3.2.4.2 Boltzmann distribution

Vicinal fluorination can bias populations of conformations and therefore influence the most likely conformations. Furthermore, solvent can also bias the *vicinally* fluorinated conformation populations, and this has implications on adopted conformations during synthesis. Table (3-1) shows dipole moments of low-energy conformers and the relative populations of each. The probability of each conformation occurring was obtained from the Boltzmann equation by using free energies (the sum of electronic and thermal free energies) obtained under the rigid rotor harmonic oscillator approximation. At this point, more solvents with a wider range of dielectric constants were added to the study. All calculations were done using PBE/6-311+G(d,p).

Table 3-1 *The dipole moments of low-energy conformers with their associated relative populations in various solvents*

Solvent	GG(E)[a]	AA(E)	GA(T)	GG(T)	AG(T)
Water	4.54(90%)	0.00(10%)	1.00(3%)	4.94(60%)	4.14(37%)
Acetone	4.42(86%)	0.00(13%)	1.01(3%)	4.84(58%)	4.02(39%)
Chloroform	4.01(68%)	0.00(33%)	0.95(8%)	4.45(49%)	3.58(43%)
Diethyl Ether	3.96(65%)	0.00(35%)	0.95(9%)	4.41(48%)	3.53(43%)
Dibutyl Ether	3.79(57%)	0.00(43%)	0.92(13%)	4.24(43%)	3.36(44%)
Hexanoic Acid	3.70(54%)	0.00(46%)	0.91(15%)	4.15(41%)	3.26(44%)
Toluene	3.64(50%)	0.00(50%)	0.89(17%)	4.08(37%)	3.19(46%)
Cyclohexane	3.54(46%)	0.00(54%)	0.86(19%)	3.99(35%)	3.12(47%)
Xenon	3.43(42%)	0.00(58%)	0.84(21%)	3.88(31%)	3.01(47%)
Argon	3.31(39%)	0.00(61%)	0.81(24%)	3.75(28%)	2.90(48%)
Vacuum	3.06(36%)	0.00(65%)	0.72(31%)	3.47(23%)	2.67(47%)

[a] degenerate conformer

The populations of conformers are calculated separately for each diastereomer. The data shows that as the dielectric constant of the solvent decreases from water to argon, the less polar conformers become more populated while the more polar conformers become less populated.

There is a transitory point at which this happens. For the *erythro* diastereomer, the transitory solvent is toluene, whereas for the *threo* diastereomer, it is dibutyl ether. That is, at dielectric constants below that of dibutyl ether, the greatest contribution is no longer from the most polar conformer. Similarly, at the dielectric constant below that of toluene, the most populated *erythro* conformation is no longer the most polar one. The GA(T) conformer does not follow the same trend as GG(T) and AG(T). It remains the least populated *threo* conformer in all solvents. Solvent polarity can therefore be used to bias populations of targeted conformations. Furthermore, the transitory point can be used as a precautionary tool in choosing suitable solvents to bias populations of conformations.

3.2.5 The influence of hyperconjugation on conformational stability

Hyperconjugation can further elucidate the relative stability of conformations observed. The extent of influence of the fluorine *gauche* effect can be investigated by NBO analysis. NBO perturbative analysis allows one to quantify the interaction between filled Lewis-type donor orbitals and empty (or low occupancy) non-Lewis acceptor orbitals. Hyperconjugation will show up as donation of the electron density from the adjacent electron-rich C-H bond to the vacant *antiperiplanar* antibonding orbital associated with the C-F bond, $\sigma \rightarrow \sigma^*$. The donor-acceptor interactions are given by the second order perturbation energy. An alternative to obtaining hyperconjugation energy using NBO is deleting specific donor-acceptor interactions and then determining the energetic effects of the deletions. In this way, the energy can be dissected into Lewis contributions and the non-Lewis contributions (the delocalization energy). The latter approach is used to quantify hyperconjugation in low-energy conformers. By obtaining the hyperconjugation energies of each conformer on the rotational profile, the extent of hyperconjugation can be inferred from the stability of a conformer. That is, structures with no fluorine atoms in *gauche* arrangement, would be expected to have little or no hyperconjugation, whereas low-energy conformers with fluorine atoms in *gauche* position should comparably have considerable hyperconjugation. Figure (3.7) shows the relative hyperconjugation energy curves of 2,3-difluorobutane superposed with the rotational profiles *in vacuo*. Table (3-2) shows the hyperconjugation energies of low-energy conformations, relative to that of the AA(E) conformer.

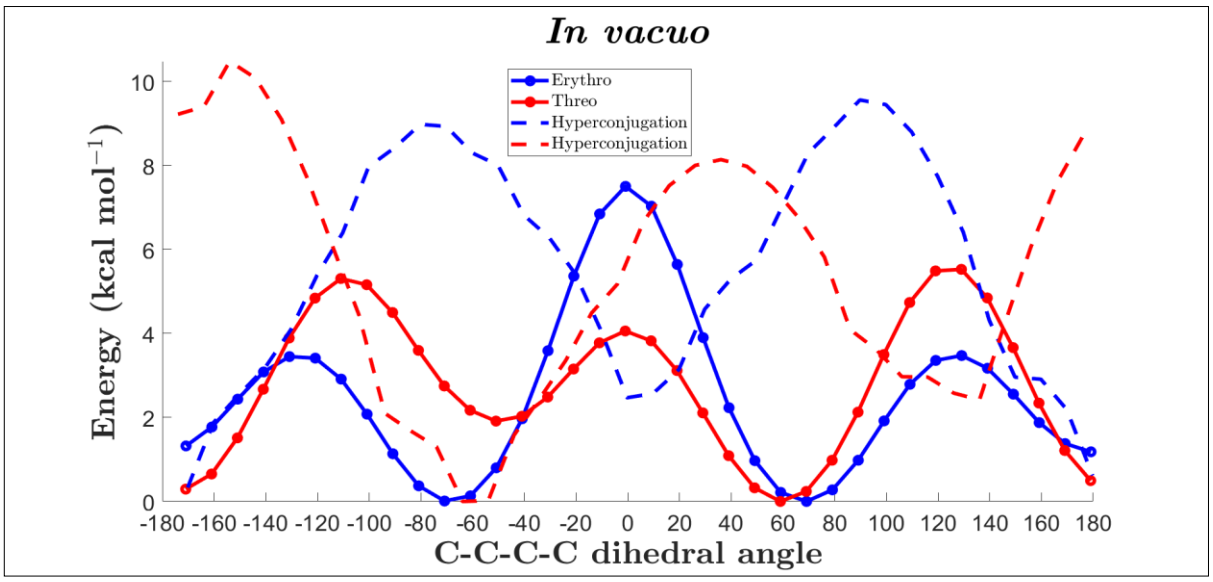

Figure 3.7 *Hyperconjugation energy curve (dotted line) of 2,3-difluorobutane superposed with the rotational energy profile. Hyperconjugation energy is relative to the lowest energy.*

Table 3-2 *Relative hyperconjugation energy relative to AA(E) for low-energy conformer*

Conformer	Hyperconjugation energy in vacuum (kcal mol^{-1})	Hyperconjugation energy in water (kcal mol^{-1})
GG(E)	4.62	4.32
GG′(E)	4.62	4.32
AA(E)	0.00	0.00
GA(T)	0.63	0.73
GG(T)	2.59	2.42
AG(T)	6.75	6.02

The relative hyperconjugation energies are qualitatively similar in vacuum and water. In water, the relative hyperconjugation energies are slightly lowered. The conformers that have the fluorine atoms in the *gauche* position have higher relative hyperconjugation energy compared to those that do not. The AG(T) conformer shows the highest relative hyperconjugation energy, whereas the AA(E) conformer shows the smallest in both vacuum and water. Although considerable hyperconjugation energy is observed in conformers with the fluorine atoms *gauche*, it does not

reflect the relative stability seen on the rotational profiles in solvent. For example, the AG(T) conformer is not the global minimum despite it showing the highest relative hyperconjugation energy. The global minimum structure in solvent, GG(T), has hyperconjugation energy that is half that of the AG(T) conformer. Therefore, hyperconjugation does not seem to be predominant interaction influencing the relative conformational stabilities of conformers.

In addition to solute and hyperconjugation interactions, steric interactions (which includes electrostatic interactions and Pauli's repulsion) can also significantly influence relative conformational stability. Rotational barriers *in vacuo* can be used to explain the relative steric effects in each conformer.[179] The concept of rotational barriers is only adopted here to try and explain the relative effects of steric interactions between any two conformers. The more stringent definition of a rotational barrier is not referred to. Therefore, the term "steric penalty" will rather be used. Table (3-3) shows conformational energy differences of each conformation relative to the global minimum AA(E) *in vacuo*.

Table 3-3 *Conformational energy differences relative to the global minimum in vacuo and in solvent*

Conformer	**In vacuo** ***(kcal mol^{-1})***	***In water (kcal mol^{-1})***
GG(E)	0.68	0.27
GG′(E)	0.68	0.27
AA(E)	0.00	1.41
GA(T)	0.86	1.91
GG(T)	0.65	0.00
AG(T)	0.27	0.29

As expected, conformers that have the methyl groups in the *gauche* position have higher relative steric penalties *in vacuo*. The GA(T) conformer shows the highest relative steric penalty *in vacuo*. In addition, it has relatively negligible hyperconjugation energy. The steric penalty present in the GA(T) conformer override the stabilizing solute interactions compared to the GG(E) conformers and the GG(T) conformer, which have considerable hyperconjugation stabilizing them. In water, the relative energies reflect the mitigation of the steric penalty by the solute interactions. The

GG(T) conformer is now the global minimum despite the high relative steric penalty seen *in vacuo*. This was attributed to its relatively high dipole moment, which lowers its energy in solvent. It can be proposed that the destabilizing 'steric interactions' are mitigated by a combination of hyperconjugation energy and solute interactions, where the solute interactions are predominant. The GG(E) conformers have higher dipole moments and higher relative hyperconjugation energies than the GG(T) conformer. This is not reflected in the relative energies and it is unexpected. On the other hand, the GG(E) conformers show slightly higher steric penalties than the GG(T) conformer.

3.2.6 The effect of the *vicinal* fluorination motif on conformational flexibility

To establish the control that *vicinal* fluorination has on conformational flexibility, an analysis of the rotational profiles around the global minimum of butane, 2-butene and the fluorinated analogues of butane was performed. Butane and 2-butene are referred to as the C-C 'single bond' and 'double bond' equivalents of each other, respectively. This is to describe and distinguish the type of bond on the bridging dihedral angle of the linker. The flexibility of 2,3-difluorobutane was quantified by thinking of a spring as being a fundamental elastic component found in mechanical systems. Thus, it can be used as a physical model for elastic properties of materials.[180] The minimum energy regions, as shown in Figure (3.8), can therefore be treated as '*elastic potential energy*' curves and the force constant of each conformer can be calculated. The shape of the curve allows the assumption of a linear force and the satisfaction of Hooke's law. The curves are non-Hookean, which is an artefact of curve fitting as the data was fitted to limited points around the minima of rotational profiles. The extent of the conformational flexibility can then be inferred from the magnitudes of the force constants. Figures (3.8a), (3.8b), (3.8c) and (3.8d) show the plots of rotational profiles for butane (single bond equivalent), butene (double bond equivalent) and the fluorinated analogues of butane at a range of angles (±10° relative to the minimum at 1° intervals) *in vacuo* (Figures 3.8a and 3.8b) and in water (Figure 3.8c and 3.8d). A second order polynomial was fitted to each curve and the force constants were obtained.

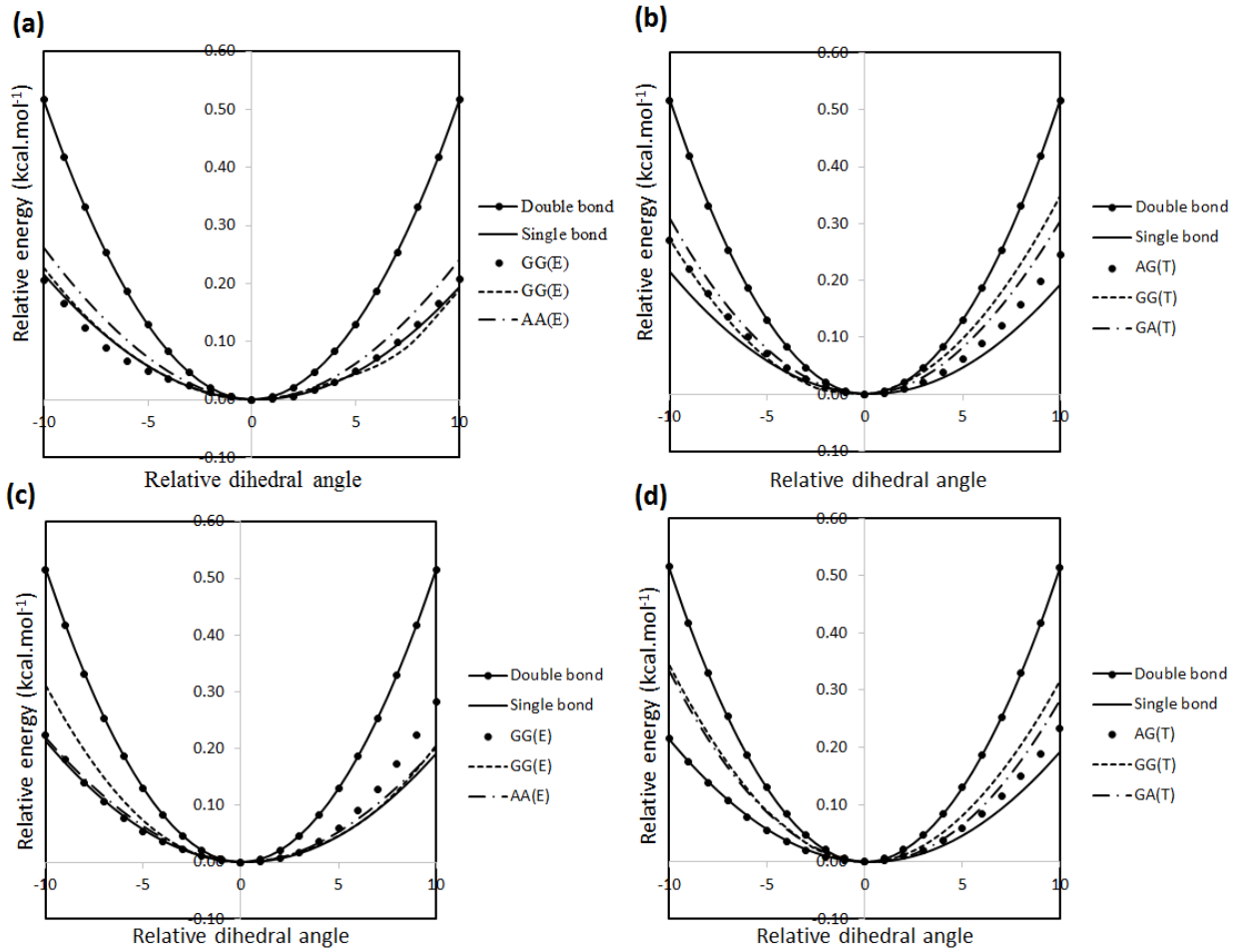

Figure 3.8 *Relative energies of butane, butene and the fluorinated analogues of butane against relative dihedral angles around respective minima (a), (b) in vacuo and (b), (d) in water. The energies and dihedral angles are normalised relative to the lowest energy and dihedral angle of the species in concern.*

The slope represents how the force around a particular minimum is changing. A higher slope reflects the difficulty of a conformer to rotate. Similarly, a lower slope indicates rotational flexibility of a conformer. The force constant can be used to quantify rotational flexibility. Table (3-4) shows the force constants for C-C-C-C rotation in butane, butene and fluorinated analogues of butane (*threo* and *erythro* conformers of 2,3-difluorobutane).

Table 3-4 *Force constants for butane, butene and the fluorinated analogues of butane*

In vacuo		***In water***	
Analogue	Force constant ($cal.mol^{-1}\ degree^{-2} \times 10^{-3}$)	Analogue	Force constant ($cal.mol^{-1}degree^{-2} \times 10^{-3}$)
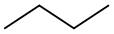	0.61	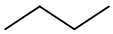	0.65
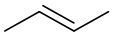	4.74	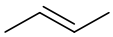	5.15
GG(E)	2.24	**GG(E)**	2.08
GG′(E)	2.20	***GG′(E)***	1.86
AA(E)	1.28	**AA(E)**	1.59
AG(T)	2.33	**AG(T)**	1.44
GG(T)	2.13	**GG(T)**	2.47
GA(T)	1.85	**GA(T)**	1.61

The larger the force constant, the stiffer the spring. In the case of conformational flexibility, the higher the force constant, the less flexible the molecule. As seen from the elastic potential curves in Figure (3.8), the force constant for butene is the largest, both *in vacuo* and in water, and that of butane is the smallest. Whilst controlling the relative energies of minima, the incorporation of a solvent does not seem to have a drastic influence on the force constants. The global minimum structure *in vacuo*, AA(E), has the smallest force constant of all fluorinated conformers. In water, the AG(T) conformer becomes the most flexible fluorinated analogue, whereas it is the least flexible *threo* conformer *in vacuo*. The GG(T) conformer is the least flexible in water.

It is noteworthy that the GG(E) and GG(T) conformers, with low relative energies in solvent, have the largest force constants out of all fluorinated species and thus the least conformational flexibility. The conformational flexibility of GG(T) is similar to that of the GA(T) conformer, which has the highest relative conformational energy *in vacuo*. This illustrates that conformational flexibility does not have any link to the relative stability of a conformation. As hypothesized, butane (the C-C single bond equivalent) shows the most conformational flexibility, butane (the double bond equivalent) shows the least conformational control and the fluorinated analogues are

intermediate between the two. This indicates that control over the conformation and dynamics of a linker could be achieved via *vicinal* fluorination.

3.3 The study of isolated MOF linkers

With the methodology and ideas formulated from the study on 2,3-difluorobutane, conformational analysis on the isolated organic linkers, 2,3-difluorosuccinic acid, 1,2-difluoro-1,2-di(pyridin-4-yl)ethane and 2,2,3,3-tetrafluorosuccinate, as shown in Figure (3.9), was performed. As with 2,3-difluorobutane, the non-fluorinated structures with single and double bonds on the bridging ligand are referred to as the C-C single bond and double bond equivalents, respectively, of the MOF linker in question.

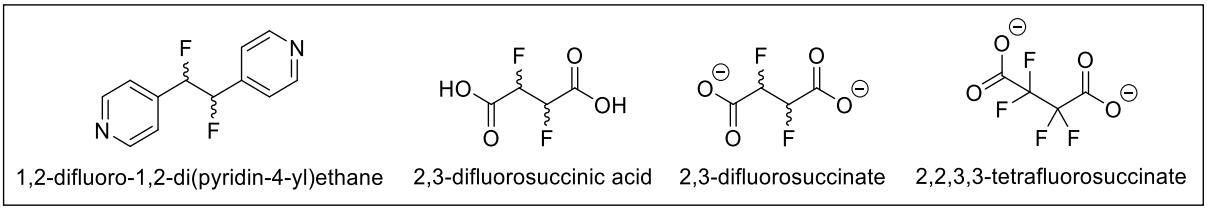

Figure 3.9 *The fluorinated analogues of isolated MOF linkers to be studied.*

The choice of these particular linkers was due to their popularity in the field of MOFs.[181–186] They are commonly used in mixed-ligand MOFs and possess different features that can potentially be explored, such as flexibility. The 2,3-difluorosuccinic acid MOF linker was included to establish the effect of deprotonation (in 2,3-difluorosuccinate) on hyperconjugation, and thus relative energies of the conformations and the structural flexibility. Since in the synthesis of MOFs, rapid assembly of MOFs is typically achieved via deprotonation of the ligands and a subsequent rapid nucleation of crystals.[187–190] The perfluorinated tetrafluorosuccinate system was included in the study for its ease of synthesis and its availability. The benchmarking study of Section 3.2.1 showed which methods are best suited for further investigations. In this section, results at the PBE/6-311+G(d,p) level of theory will be presented. Since the general effect of solvent on the relative

energies of conformations was established in the study of 2,3-difluorobutane, only water is adopted in the study of rotational profiles of isolated MOF linkers.

3.3.1 Rotational profiles of isolated MOF linkers

3.3.1.1 2,3-difluorosuccinic acid

Figure (3.10) shows the optimised conformers of 2,3-difluorosuccinic acid in a 3D representation.

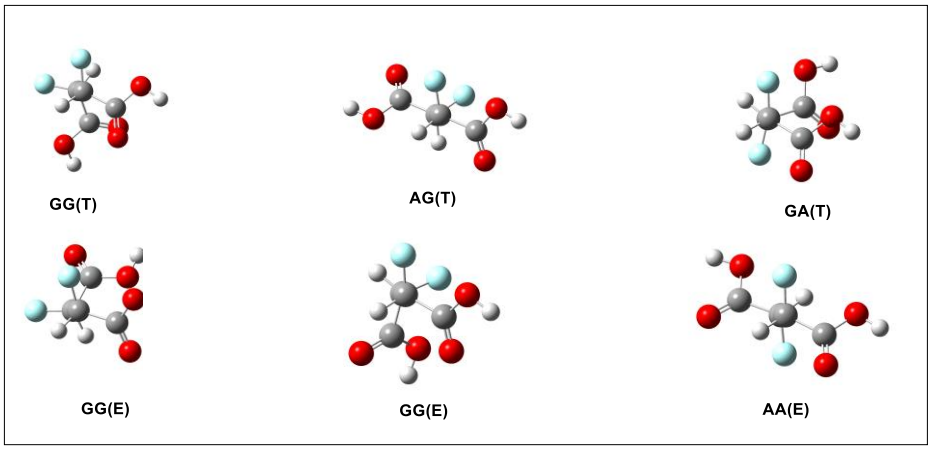

Figure 3.10 *Structures of 2,3-difluorosuccinic acid conformers in a 3D representation.*

Figure (3.11) shows the torsional profile for 2,3-difluorosuccinic *in vacuo* and in water. The two GG(E) conformers are not degenerate *in vacuo*, with an energy difference of 0.52 kcal.mol^{-1}. This is attributed to the changes in orientation that the side carboxylic acid groups undergo, raising the energy of one conformer over the other. The GG(E) conformer that has a dihedral angle of ~75° is the global minimum structure and the GA(T) conformer has the highest relative conformational energy. In contrast to the case of 2,3-difluorobutane, the conformers that have the fluorine atoms in the *gauche* position are more stabilized than those that do not *in vacuo*.

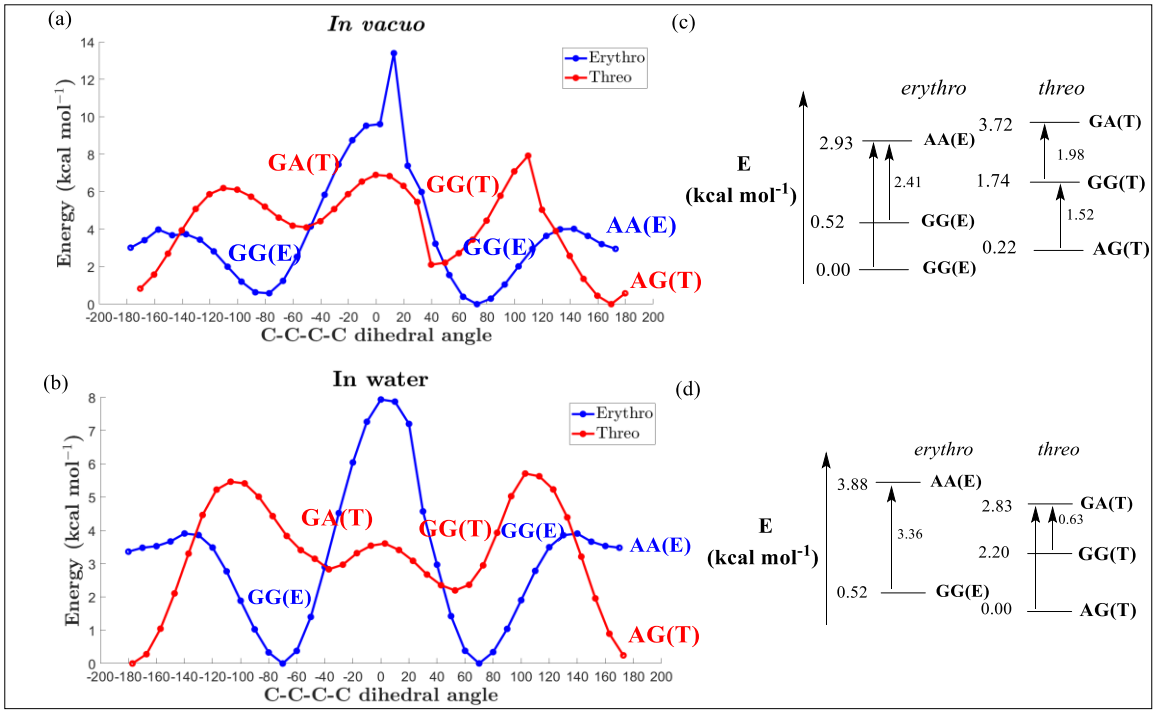

Figure 3.11 *Rotational profile of* **threo***-2,3-difluorosuccinic acid (red),* **erythro***-2,3-difluorosuccinic acid (blue), (a) in vacuo and (b) in water. Threo and erythro energies are relative to the global minimum. A representation of relative energies of 2,3-difluorosuccinic acid threo and erythro conformers at the PBE/6-311+G(d,p) level (c) in vacuo and (d) in water.*

The energy spike at ~20° on the torsional profile of *erythro* 2,3-difluorosuccinic acid *in vacuo* is the result of the carboxylic acid groups undergoing a large change of orientation whilst the C-C-C-C dihedral only undergoes a small change. Essentially, it is the transition from one PES[191] to another, where the difference between the two PESs is the relative orientation of the hydroxyl groups on the carbonyl carbon. There are two orientations that the hydroxyl groups can adopt, either '*cis*' or '*trans*' to each other, as shown in Figure (3.12). That is, the OH groups can be on the same side of an axis (*cis*) that runs through the carboxylic carbons or they can be on opposite sides (*trans*). The energy scan starts with the OH groups *cis* and they switch to *trans* at the spike. A more refined fixed scan (per degree instead of 10° for example) around the spike does not smooth it out. This also applies to all the slight energy spikes (~-160° on the *erythro* curve, ~40° and ~117° on the *threo* curve) seen on the torsional profiles. However, simply extending the number of coordinate steps might lead to just observing multiple transitions. A more extensive

conformational analysis study that can address this issue needs to be carried out, but it is not the focus of this work. The assessment of such flexibility in molecules using computational methods is an active area of research.[192–194]

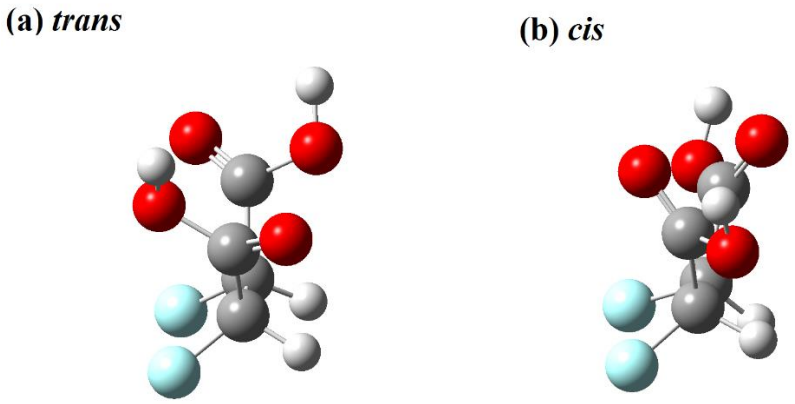

Figure 3.12 *The orientations that 2,3-difluorosuccinic acid can exist in as taken from the PES of the erythro isomer in vacuo. (a) The OH groups are trans to one another. (b) The OH groups are cis to one another relative to the axis running through the carboxylic carbons.*

The stabilising solvent interactions mitigate abrupt changes of orientation seen *in vacuo* and therefore leads to smoother rotational profiles. In water, the global minimum structure is the GG(T) conformer while the AA(E) conformer has the highest relative conformational energy. This drastic change in energy of conformers from vacuum to water, can be elucidated by considering dipole moments as in 2,3-difluorobutane. The carboxylic acid groups can adopt many more conformations than the methyl groups in 2,3-difluorobutane, since their flexibility introduces further degrees of freedom. As a result, differences in conformer energies can be anticipated when results are compared to those of 2,3-difluorobutane.

3.3.1.2 2,3-difluorosuccinate

Figure (3.13) shows the conformational structures of 2,3-difluorosuccinate in a 3D representation and Figure (3.14) shows the rotational profile of 2,3-difluorosuccinate *in vacuo* and in water. In

addition to the conformational freedom possessed by the side carboxylic acid groups, the charged nature of 2,3-difluorosuccinate is expected to play a role in the energy dynamics.

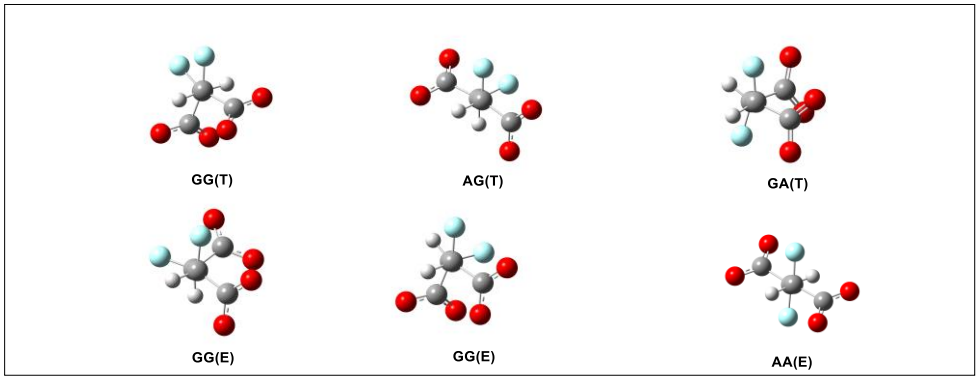

Figure 3.13 *Conformational structures of 2,3-difluorosuccinate in 3D.*

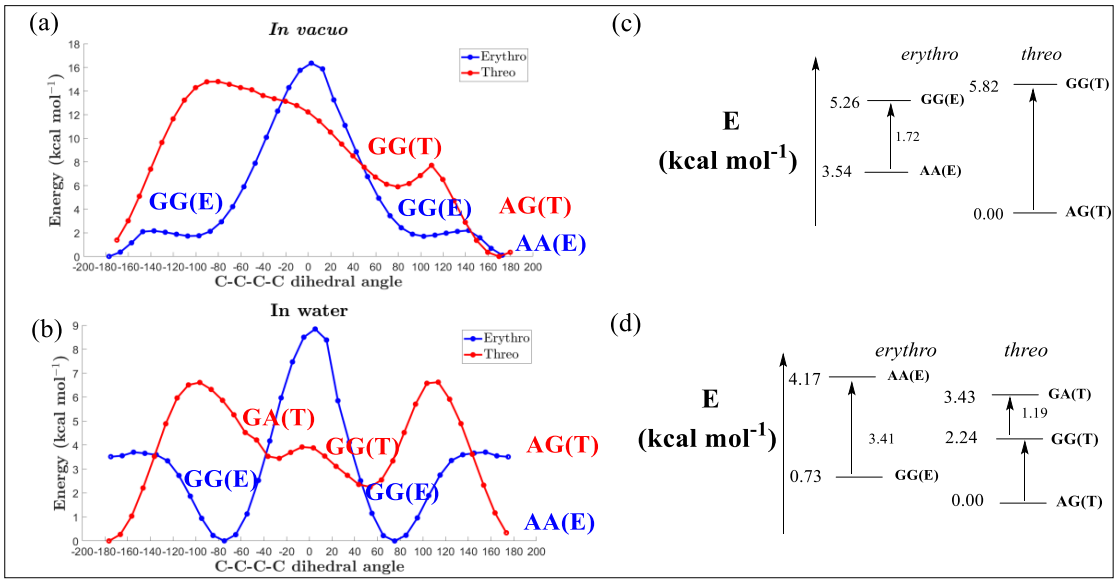

Figure 3.14 *Rotational profile of threo 2,3-difluorosuccinate (red), erythro (blue) (a) in vacuo and (b) in water. Threo and erythro energies are relative to the global minimum (c),(d) Calculated energy differences between the 2,3-difluorosuccinate threo and erythro conformers at the PBE/6-311+G(d,p) level in water.*

In contrast to the protonated system, there are only two *threo* minima *in vacuo*, the GG(T) and AG(T) conformers, with the AG(T) conformer being the global minimum structure. The GA(T) conformer is presumably destabilized by the repulsive electrostatic interactions resulting from the

carboxylic acid groups in the *gauche* position. The GG(T) conformer also has the carboxylic acid groups in the *gauche* position, however, there might also be stabilizing hyperconjugation interactions, which seems to provide sufficient compensation to overcome the electrostatic repulsion and lead to a stable conformer. This is supported by the work of O'Hagan *et al.*,[195] who have synthesized solid state *erythro* and *threo* conformations and found, by inference from J-coupling constants, that there is a significant fluorine *gauche* effect in 2,3-difluorosuccinates.

In water, the AG(T) conformer remains the global minimum structure. Despite the electrostatic repulsion present in the GG(E) conformers and the GG(T) conformer, the structures show lower relative energies in water. This suggests that the stabilizing solvent interactions mitigate the destabilizing electrostatic repulsion effects.

3.3.1.3 The effect of deprotonation of 2,3-difluorosuccinic acid

Deprotonating 2,3-difluorosuccinic acid introduces new structural features that causes different structural behaviour. These factors include delocalization of charge between oxygen atoms of the carboxylic acid groups, increased steric interactions between the side carboxylic acid groups and less conformational freedom of these groups. Figure (3.15) shows the torsional profiles of 2,3-difluorosuccinic acid and 2,3-difluorosuccinate, side by side for ease of reference.

Much more complex and unpredictable rotational profiles are observed *in vacuo* for both 2,3-difluorosuccinic acid and 2,3-difluorosuccinate. This is as a consequence of the additional degrees of freedom in the carboxylic acid groups. The cusps observed *in vacuo* are smoothened by the introduction of solvent.

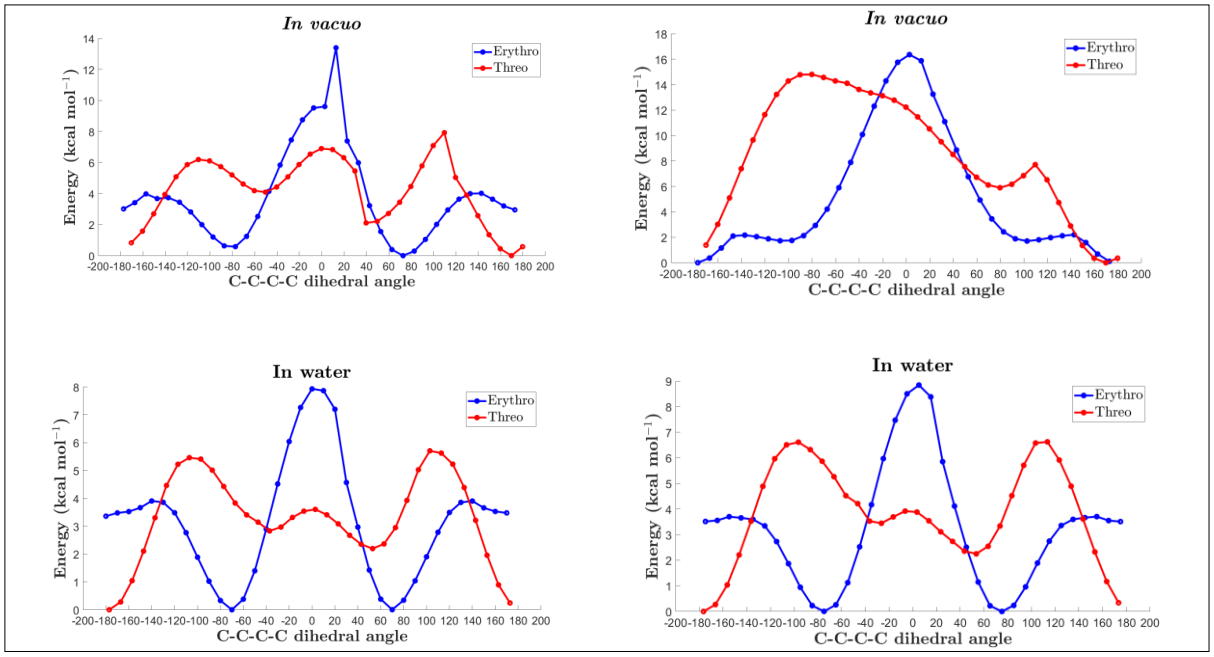

Figure 3.15 *Rotational profiles of the protonated (left) and deprotonated (right) systems in vacuo and in water to highlight the effects of 2,3-difluorosuccinic deprotonation.*

The energy difference between the global minimum and global maximum structure of 2,3-difluorosuccinic acid and 2,3-difluorosuccinate *in vacuo* is 1.52 kcal.mol^{-1} and 5.89 kcal.mol^{-1}, respectively. The carboxylic groups (COO$^-$) cause a higher barrier of rotation as expected from their negative charge. To characterize this steric interaction of the COOH and COO$^-$ groups, A-values, used to quantify steric effects of substituents in cyclohexane conformations can be adopted.[196]. A larger A-value indicates a larger steric effect of a substituent. The A-values for COO$^-$ and COOH are 2.0 and 1.4 kcal.mol^{-1}, respectively.[197] There are many other ways to quantify steric effects using steric parameters used in organometallic chemistry such as the ligand repulsive energy, but these were not investigated in further detail here.[196–198] The AA(E) conformer of 2,3-difluorosuccinate is more stable than the GG(E) conformer, unlike for the acid where GG(E) is more stable. This further supports the view of enhanced repulsive steric effects between the deprotonated carboxylic acid groups.

The sensitive nature of describing anionic species in the gas phase using DFT calculations should be addressed. Typically employed exchange-correlation functionals in KS-DFT do not adequately describe the extra electron on anions. Consequently, an inaccurate electronic structure is described, which leads to qualitatively erroneous results.[199]

3.3.2 Rotational profiles of 1,2-difluoro-1,2-di(pyridine-4-yl)ethane

The incorporation of a bipyridyl ligand in this study is motivated by the coordination of the ligand with metal centres to form relatively flexible frameworks based on binding neutral pyridyl groups of ligands. Pyridyl groups are ideal connectors between transition metals to form porous 3D frameworks with high surface areas, periodic pore structure, large pore volume and good gas storage properties.[200] Inclusion of 1,2-difluoro-1,2-di(pyridin-4-yl)ethane is motivated by the investigation of *vicinal* fluorination on conformational control. Figure (3.16) shows conformations of 1,2-difluoro-1,2-di(pyridin-4-yl)ethane in 3D.

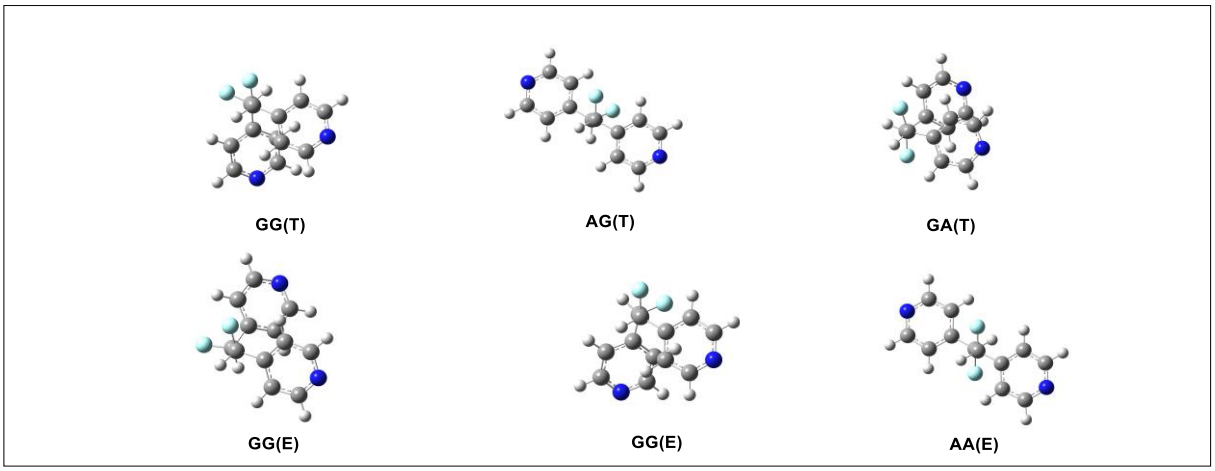

Figure 3.16 *Conformational structures of 1,2-difluoro-1,2-di(pyridine-4-yl)ethane in 3D.*

The behaviour of 1,2-difluoro-1,2-di(pyridin-4-yl)ethane is much more predictable as indicated by the smooth rotational profiles in Figure (3.17). The isoenergetic GG(E) conformers are the global minima *in vacuo* and the AG(T) conformer is the conformer with the highest relative conformational energy. In water, the GG(T) conformer becomes the global minimum in water,

with the GA(T) conformer having the highest relative conformational energy. Conformers with the pyridyl rings are found to have higher relative energies in both vacuum and water. It is expected that the bulky pyridyl rings should sterically hinder *gauche* conformers. However, stabilizing factors that can surpass any destabilizing ones clearly exist. The stabilizing factors are presumably π-stacking interactions from the stacked arrangement of the pyridyl rings in the *gauche* position.[201]

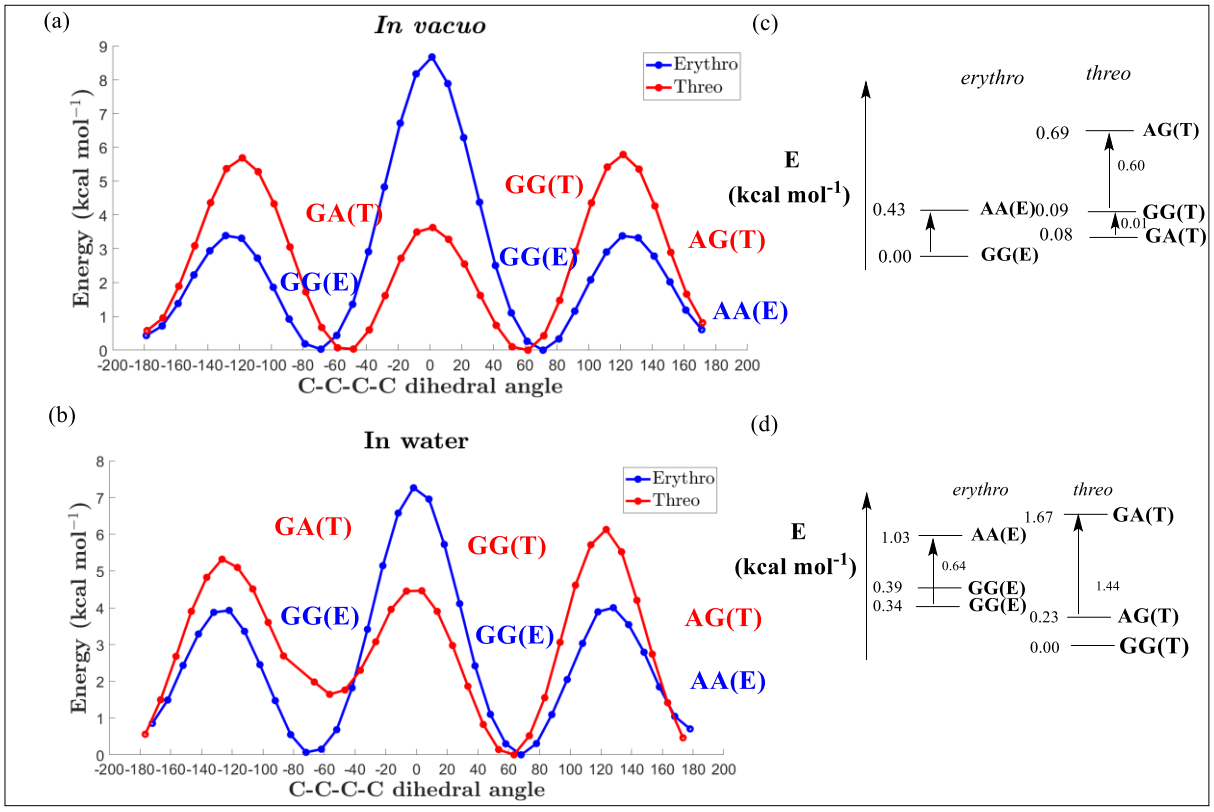

Figure 3.17 *Rotational profile of erythro-1,2-difluoro-1,2-di(pyridin-4-yl)ethane (blue) (a) in vacuo and (b) in water. Threo and erythro energies are relative to the global minimum. (c), (d) A representation of relative energies calculated at a PBE/6-311+G(d,p) level.*

3.3.3 Solvation and hyperconjugation effects on conformational control of MOF linkers

To rationalize the relative energies of conformers on the rotational profiles, solvation effects and hyperconjugation are once again going to be looked at. The molecular dipole moments of the low-

energy conformations, shown in Appendix IV, were once again considered. Table (3-5) shows relative energies of hyperconjugation for each linker *in vacuo* and in water.

Table 3-5 *Relative hyperconjugation energy (kcal.mol^{-1}) of the isolated linkers in vacuo and in water*

	2,3-difluorosuccinic acid		***2,3-difluorosuccinate***		***1,2-difluoro-1,2-dio(pyridine-4-yl)ethane***	
	In *vacuo*	In water	In *vacuo*	In water	In *vacuo*	In water
GG(E)	17.78	16.47	3312.76	0.00	6.11	5.41
GG′(E)	23.16	21.14	4615.07	1.10	6.21	5.49
AA(E)	0.00	0.00	27606.46	10023.75	0.00	0.00
AG(T)	17.86	16.24	0.00	0.47	7.58	7.71
GG(T)	15.73	14.38	28825.22	14630.28	3.20	2.26
GA(T)	11.29	10.25	-	-	1.75	2.13

3.3.3.1 Conformational analysis of 2,3-difluorosuccinic acid

In vacuo, there is no apparent connection between the dipole moment of the conformer and its relative conformational energy. The GA(T) conformer has a dipole moment that is comparable to that of the global minimum, despite it having the highest relative conformational energy. On the other hand, relative energies of hyperconjugation explain the relative stabilities of conformations. The conformers with the fluorine atoms in the *gauche* position generally have lower energies. The GG′(E) conformer has the highest relative hyperconjugation energy and it is the global minimum. The GA(T) is the exception because despite its considerable hyperconjugation energy and its high dipole moment, it has the highest relative conformational energy. Steric effects from the carboxylic acid groups being *gauche* seem to override present stabilizing interactions. Hyperconjugation effects considerably and predominantly contribute to conformational stability *in vacuo.*

For 2,3-difluorosuccinic acid in water, the AA(E) conformer, with the highest relative conformational energy, has the smallest dipole moment as expected, suggesting the absence of polar stabilizing interactions. In addition, the AA(E) conformer has insignificant hyperconjugation compared to conformers with the fluorine atom in the *gauche* position. The global minimum, AG(T), has a molecular dipole moment of 4.49 D, while the GG(T) conformer has the largest

dipole moment of 5.09 D. Steric crowding from the *gauche* positions of the bulky carboxylic acid groups in the GG(T) conformer mitigate the stabilizing polar interactions. This steric crowding is absent in the AG(T). Furthermore, there is considerable hyperconjugation energy in the AG(T) conformer, which further stabilizes it. The GG(E) conformer of 2,3-difluorosuccinic acid has a considerably smaller dipole moment (0.76 D in water) compared to the GG(T) conformer and thus polar solvent interactions are decreased. However, the GG(E) conformer has a lower relative conformational energy. This can be explained by the higher relative hyperconjugation energy of the GG(E) conformers. In solvent, the stabilizing solute interactions and hyperconjugation interactions enhance each other.

O'Hagan *et al.*[202] synthesized both the *threo* and *erythro* isomer of 2,3-difluorosuccinic acid as shown in Figures (3.18a) and (3.18b).

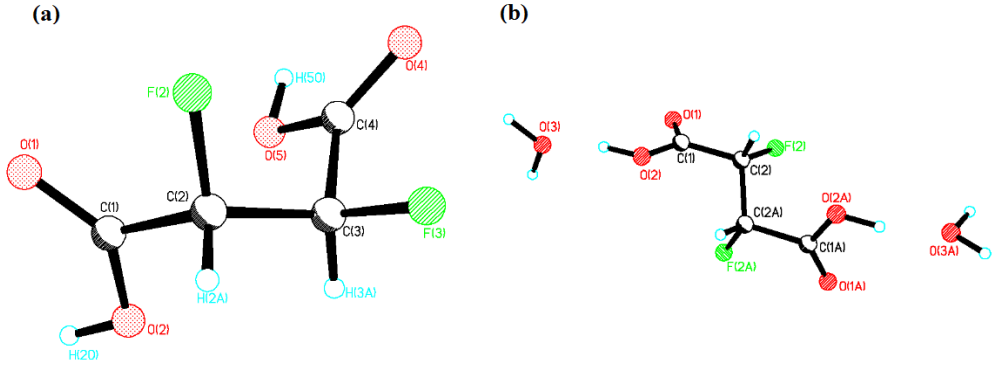

Figure 3.18 *The X-ray crystal structure of 2,3-difluorosuccinic acid (a) erythro diastereomer (b) threo diastereomer synthesized by O'Hagan et al.*

In the X-ray crystal structure of the *erythro* diastereomer of 2,3-difluorosuccinic acid, both the carboxylic acid carbonyl oxygens adopt a *syn* periplanar conformation with respect to the C-F bonds and in that of the *threo* isomer the molecule is in an extended chain conformation with both the C-F bonds *gauche* to each other and the carboxylic acid groups antiperiplanar. This is in line with the fluorine *gauche* effect of 2,3-difluorosuccinic acid as confirmed by experiment. The

findings of O'Hagan *et al.* further supported the observation that the low-energy conformations with the fluorine atoms in *gauche* positions are influence by the fluorine *gauche* effect.

3.3.3.2 Conformational analysis of 2,3-difluorosuccinate

Conformers with the carboxylate groups in *anti* position have lower relative energies than those that do not. In water, the AA(E) conformer, with the highest relative conformational energy, has the smallest dipole moment as expected. The AG(T) conformer, with a large dipole moment, is the most stable conformer. Steric crowding in conformers with the carboxylic acid groups in the *gauche* positions mitigates solute and hyperconjugation interactions. Unusually large relative hyperconjugation energies are observed. This is attributed to the fact that the non-Lewis energetic contributions include delocalization that exists in the carboxylates.

In solvent, the stabilizing solute interactions are mitigated by the destabilizing electrostatic repulsion. Compared to 2,3-difluorosuccinic acid, the molecular dipole moments of the 2,3-difluorosuccinate are larger than those of the protonated version in various solvents. For example, the dipole moment of the GG(E) conformer of the protonated species is 0.76 D whilst that of deprotonated GG(E) is 11.7 D. However, this is not reflected in the relative minimum energies of the conformations. The extent of stabilization from the higher dipole moments of the deprotonated system is reflected in the higher energy barriers.

3.3.3.3 Conformational analysis of 1,2-difluoro-1,2-di(pyridin-4-yl)ethane

In vacuo, conformers with the pyridyl rings in the *gauche* position are more stabilized than those that do not. Relative hyperconjugation energies do not match the relative conformational energies. The AG(T) has the highest relative conformational energy despite it having the highest relative hyperconjugation energy. It can be proposed that the π-stacking interactions of the pyridyl rings are the dominant interactions lowering relative conformational energies *in vacuo.*

In water, the relative hyperconjugation energies match the relative conformational energies. Conformers with considerable hyperconjugation in them have their relative conformational energies lowered. Conformers that do not have considerable hyperconjugation in them have raised relative conformational energies. For example, the AA(E) and the GA(T) conformers have high relative conformational energies and low relative hyperconjugation energy. Furthermore, hyperconjugation and solvent interactions work together to lower the overall relative conformational energy.

3.3.4 Rotational profiles of 2,2,3,3-tetrafluorosuccinate

The incorporation of 2,2,3,3-tetrafluorosuccinate in the study is motivated by its ease of synthesis and therefore availability. In this case, *vicinal* fluorination as a structural motif is absent. However, a new fluorination pattern can be explored. The Figure (3.19) shows rotational profiles of 2,2,3,3-tetrafluorosuccinate *in vacuo* and in water.

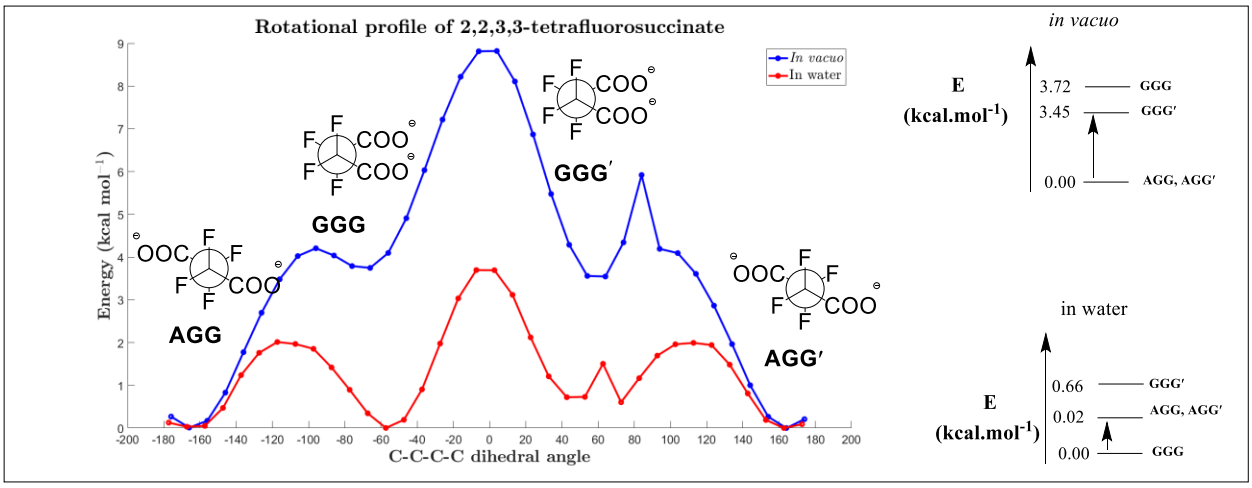

Figure 3.19 *Rotational profiles of 2,2,3,3-tetrafluorosuccinate in vacuo and in water.*

From the rotational profiles, the stability of the conformers brought about by the solvent can be inferred. The lowering of minima as well as barrier heights can be attributed to the indiscriminate solvent interactions. Like with previous linkers, dipolar interactions can be investigated by looking

at the molecular dipoles of 2,2,3,3-tetrafluorosuccinate conformers. Table (3-6) shows the molecular dipole moments of minimum conformers with their associated dihedral angles.

Table 3-6 *The dipole moments of 2,2,3,3-tetrafluorosuccinate conformers with their associated dihedral angles*

Conformer	**Dihedral angle (°)**	**Dipole (D)**
	Water	
AGG	-162.66	1.38
AGG′	162.67	1.38
GGG	-55.02	8.13
GGG′	47.91	8.09
	Vacuum	
AGG	-164.02	1.12
AGG′	164.03	1.11
GGG	-57.31	6.02
GGG′	59.22	6.11

In vacuo, the *anti* conformers (AGG and AGG′) have dipole moments of 1.12 D and 1.11 D, respectively, and the *gauche* conformers (GGG and GGG′) both have dipole moments of 6.02 D and 6.11 D, respectively. The *gauche* conformers have higher relative conformational energies because of the repulsive electrostatic interactions between the bulky carboxylic acid groups. In water, the destabilizing interactions are overshadowed by the stabilizing solute interactions brought about the higher dipole moments of the *gauche* conformers.

3.3.5 The *vicinal* fluorination motif on conformational control

Similar to 2,3-difluorobutane, the extent of linker flexibility can be quantified by obtaining force constants from a curve fit, as shown in Figure (3-20). Table (3-7) shows the force constants for the conformers of 2,3-difluorosuccinic acid and 1,2-difluoro-1,2-di(pyridin-4-yl)ethane.

Table 3-7 *Force constants of various species of the different MOF linkers*

2,3-difluorosuccinic acid		**2,3-difluorosuccinate**		**1,2-difluoro-1,2-di(pyridin-4-yl)ethane**	
Species	Force constant $(cal\ mol^{-1} degree^{-2} \times 10^{-3})$	Species	Force constant $(cal\ mol^{-1} degree^{-2} \times 10^{-3})$	Species	Force constant $(cal\ mol^{-1} degree^{-2} \times 10^{-3})$
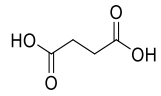	1.43	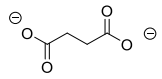	0.97	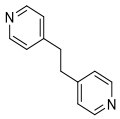	1.94
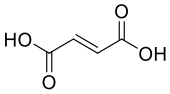	3.93	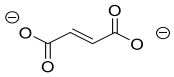	3.19	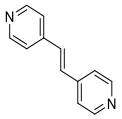	4.38
GG(E)	**3.64**	**GG(E)**	1.85	**GG(E)**	2.82
GG(E)	2.45	**GG(E)**	1.84	**GG(E)**	2.34
AA(E)	1.15	**AA(E)**	1.73	**AA(E)**	1.95
AG(T)	1.83	**AG(T)**	**3.27**	**AG(T)**	2.82
GG(T)	1.07	**GG(T)**	1.98	**GG(T)**	2.65
GA(T)	1.90	**GA(T)**	-	**GA(T)**	2.71

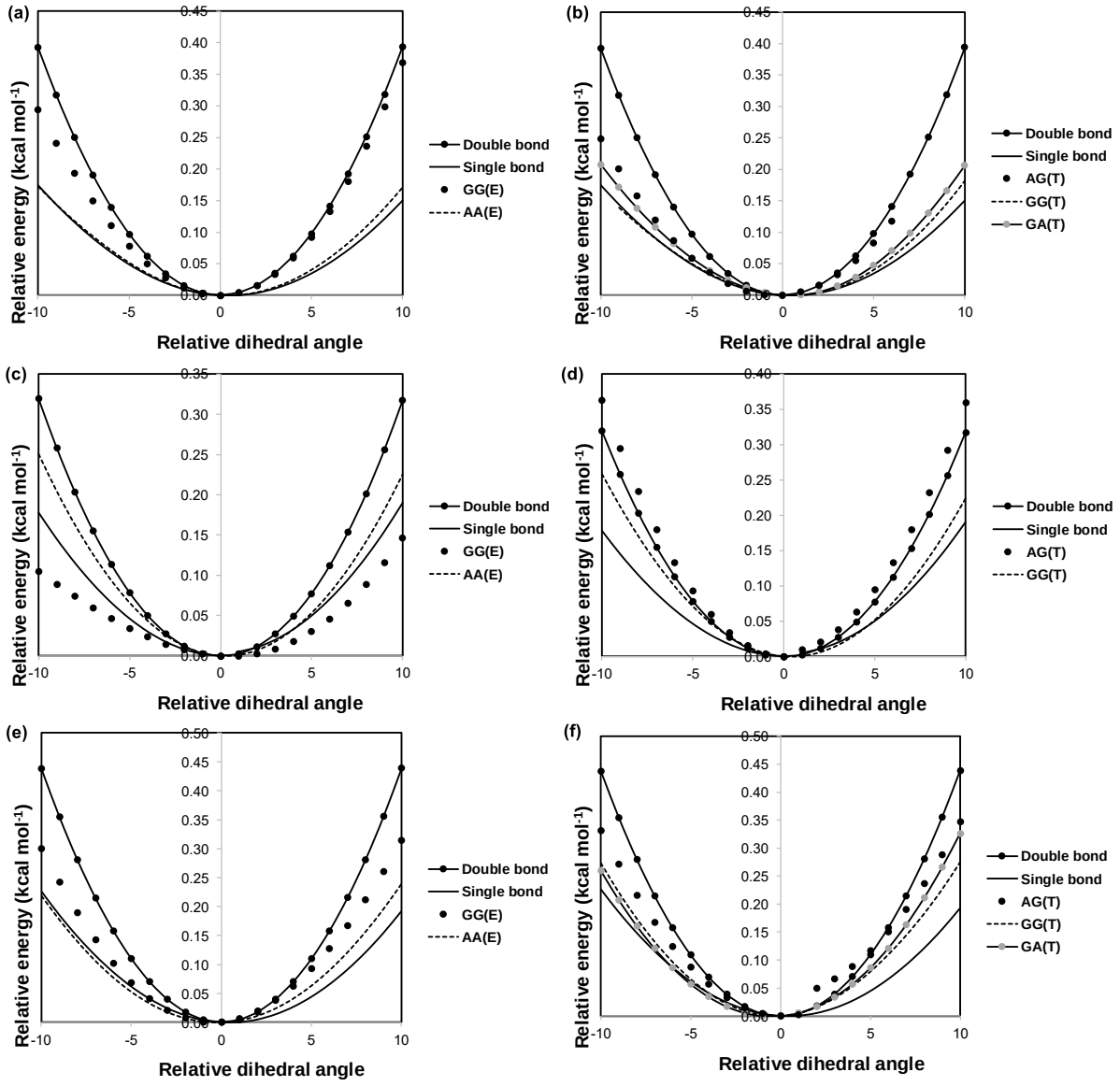

Figure 3.20 *Relative energies of the non-fluorinated and fluorinated species of (a), (b) 2,3-difluorosuccinic acid (c), (d) 2,3-difluorosuccinate (e), (f) 1,2-difluoro-1,2-di(pyridine-4-yl)ethane relative to normalised dihedral angles in vacuo. The energies and dihedral angles are relative to the lowest energy and dihedral angle of the structure in concern. 'E' denotes erythro and 'T' denotes threo.*

As expected, the force constants for the double bond equivalents are the largest for 2,3-difluorosuccinic acid and 1,2-difluoro-1,2-di(pyridin-4-yl)ethane. An exception is seen for 2,3-difluorosuccinate, where the AG(T) conformer has the largest force constant. Similarly, the

smallest force constants are those of the single bond equivalents for 2,3-difluorosuccinate and 1,2-difluoro-1,2-di(pyridin-4-yl)ethane, with the AA(E) conformer of 2,3-difluorosuccinic showing the smallest force constant. The force constants of the fluorinated analogues are intermediate between the single and double bond equivalents. However, the AG(T) conformer of 2,3-difluorosuccinate shows a force constant that is larger than the double bond equivalent and the GG(E) conformer shows a smaller force constant than the single bond equivalent. Deprotonating 2,3-difluorosuccinic acid decreases the force constant for the double bond equivalent, suggesting an increase in flexibility. For the single bond equivalent, there is a slight increase in the force constant, and therefore a slight decrease in flexibility. Thus, for 2,3-dilfuorosuccinate, deprotonation leads to a decrease in flexibility for some conformers, which does not follow the expected trend. This could be a consequence of the high negative charge of this anionic species, which leads to reduced flexibility.

For 1,2-difluoro-1,2-di(pyridin-4-yl)ethane, the results are as expected, fluorinated species have force constants that are intermediate between the single and double bond equivalents. Upon *vicinal* fluorination, there is a notable increase in conformational flexibility.

Table (3-8) shows the force constants of the conformers of 2,2,3,3-tetrafluorosuccinate and its single bond and double bond equivalents. With most conformers having force constants intermediate between the single and double bond equivalents, the GGG_2 conformer has a force constant larger than the double bond equivalent. Just as in the case of 2,3-difluorosuccinate, it is observed that the presence of charge in the linker makes the flexibility more difficult to predict.

Table 3-8 *Force constants of the various of the 2,2,3,3-tetrafluorosuccinate MOF linker*

Analogue	**Force constant** $(cal.mol^{-1}\ degree^{-2} \times 10^{-3})$
Single bond	0.97
Double bond	3.19
AGG	2.14
AGG′	2.37
GGG	1.96
GGG′	3.81

3.4 Summary

In the reference studies of 2,3-difluorobutane, a comparative assessment of various DFT functionals was performed by calculating rotational profiles of *threo* and *erythro* 2,3-difluorobutane. Relative energies of the low-energy conformations obtained by using various DFT functionals and the MP2 method were compared. From this error analysis, it was established that the PBE functional showed the lowest discrepancy to MP2, while M05-2X showed the largest discrepancy. In addition to this, PBE is less computationally intensive (as it does not require calculation of exact exchange), which proved useful when calculations were performed on larger systems. With this, PBE was rendered a fitting choice for further large-scale studies.

Rotational profiles of *threo*- and *erythro*-2,3-difluorobutane were also calculated in several solvents. No significant differences were seen across the functionals and the relative energies of the low-energy conformations did not vary greatly from one functional to the next. Rather, a consistent trend was observed across all functionals. In *vacuo*, the AA(T) conformer is the most stable conformation, while the GG(E) was the least stable conformation. In solvent, the GG(T) becomes the global minimum, while the GA(T) conformation becomes the least stable. Outliers were observed with M05-2X results in chloroform, where the relative energies of the *erythro*'s low-energy conformations were considerably higher. These large discrepancies are attributed to

the specific parameterization of the M05-2X functional. The key in the performance of the Minnesota functionals is the parameter fitting to an extensive set of reference data, making them exist in a heavily parameterized functional form.[203]

The effect of the functional on the eclipsed conformations (high-energy conformations) was also investigated. As with the minimum structures, no apparent large differences were observed when the changing functional. A consistent trend of the relative energies of the conformations was observed across all functionals.

3.4.1 Analysis of 2,3-difluorobutane

A comprehensive study of 2,3-difluorobutane was performed. This included the calculation of rotational profiles in vacuum and in solvent, NBO analysis and the Boltzmann weighing of the low-energy conformations. The incorporation of solvent in the calculation of rotational profiles highlighted the significance of the solvent-induced dipole moments and therefore provided insight into the influence that solvation has on conformational stability. Electrostatics interactions encountered in the polar solvents increase with increasing dielectric constant. These interactions have considerable influence on the relative conformational energies and thus the stability of the low-energy conformations, more than other interactions, such as hyperconjugation.

The incorporation of NBO analysis assisted with investigating the extent of influence hyperconjugation has on conformational stability. The relative conformational stability on the rotational profile did not necessarily match the relative hyperconjugation energies. Additionally, the conformer with the highest relative hyperconjugation energy was not the conformer with the lowest relative conformational energy. It was also observed that hyperconjugation insignificantly attenuates when solvent is introduced, suggesting that the extent of hyperconjugation does not drastically change when a solvent is introduced.

When the molecular environment was changed by solvation, significant changes were observed. The most stable AA(E) conformer became the least stable conformer when solvent was introduced. Relative energies of other conformations with higher dipole moments became lower whereas conformations with low dipole moments had higher relative energies. In addition to the minimal hyperconjugation effects, the high molecular dipole moments of some conformers stabilized the overall energy via solvent induced polar interactions. The stabilizing solvation effects seemed to override the destabilizing steric repulsions of the methyl groups in GG(T), which became the global minimum in solvent. In addition to the *gauche* effect in the next most stable conformer, AG(T), the methyl groups are in *anti* arrangement, minimizing the steric interactions. These observations indicate that in polar media, the stabilization of polar conformations is the dominant effect on conformer stability. Capecilli *et al.*[204] investigated solvent effects on the conformations of chloroethane and observed an increase in the weight/population of the *gauche* conformation in going from non-polar to polar solvents. Fox *et al.*[173] also observed a similar trend, where the AG(T) and GG(T) becomes the most populated in water. A similar trend was observed when more solvents were included in the study and the range of dielectric constants increased. The population of the more polar conformers increased with the increasing solvent polarity. A transitory point, where the polar conformations stop being the least populated as the solvent polarity is increased, was identified. This transitory point has implications when a solvent is chosen during the synthesis of MOFs. A solvent that is close to the transitory point can be avoided to bias populations in one direction or the other.

3.4.2 The conformational flexibility of 2,3-difluorobutane

To fully investigate the effect of *vicinal* fluorination on conformational control, the extent of flexibility was to be quantified. This was done by obtaining a force constant from a curve fit to an *elastic potential curve.* As hypothesized, butane and butene indicated the most and least amount of flexibility, respectively, and the fluorinated species had flexibilities that were intermediate between the two. No significant change going from vacuum to solvent was reflected in the force constants. This suggested that, in this case, solvation effects have little influence on the dynamic properties of the species. The investigation of the dynamic properties of butane and its *vicinally*

fluorinated analogues indicated the power held by the *vicinal* fluorination to bias conformations and achieve conformational locking by design.

3.4.3 MOF linkers

3.4.3.1 Conformational analysis of 2,3-difluorosuccinic acid

Unexpected results were observed for 2,3-difluorosuccinic acid *in vacuo* — the GG(E) conformer, which should have significant steric repulsion, was the global minimum and the AA(E) conformer had the highest relative conformational energy. In addition, conformers with the fluorine atoms in the *gauche* position had lower relative conformational energies. It was therefore shown that hyperconjugation effects considerably and predominantly contribute to conformational stability *in vacuo.* Furthermore, hyperconjugation interactions mitigate the effects of steric interactions between the bulky groups. In solvent, it was found that the stabilizing solute interactions and hyperconjugation interactions cooperate to control conformational energy.

3.4.3.2 Conformational analysis of 2,3-difluorosuccinate

The extent of destabilization brought about by the steric repulsion of the bulky carboxylate acid groups could be inferred from the A-values. The electrostatic repulsion between two carboxylate groups in the *gauche* position were observed to maximize the relative conformational energy. *In vacuo,* complex rotational profiles with PES transitions were seen. In addition, unusually large relative hyperconjugation energies were calculated. This was attributed to the extra delocalization present in the carboxylate groups. The complex rotational profiles were smoothened by introduction of a solvent. Furthermore, solvent lowered the high energy barriers that exist because of the charged species. No conclusive remarks could be made about the extent of hyperconjugation from the NBO results. However, stabilization of conformers with the fluorine atoms in the *gauche* position as observed from rotational profiles could suggest the presence of the fluorine *gauche* effect.

3.4.3.3 Conformational analysis of 1,2-difluoro-1,2-di(pyridin-4-yl)ethane

In vacuo and in water, the conformations of 1,2-difluoro-1,2-di(pyridin-4-yl)ethane with the pyridyl ligands in the *gauche* position had lower relative conformational energies compared to conformers that did not. This was attributed to the π-stacking interactions. *In vacuo*, stabilizing π-stacking is the dominant interactions lowering relative conformational energies. However, cooperative stabilizing interactions that include solvent and hyperconjugation were proposed for conformations in water.

3.4.4 Conformational flexibility of MOF linkers

For 2,3-difluorosuccinic acid and 1,2-difluoro-1,2-(pyridin-yl)ethane, similar results to 2,3-difluorobutane are observed. That is, the C-C double bond equivalent shows the least flexibility, the C-C single bond equivalent shows the most flexibility and fluorinated analogues have intermediate flexibilities. *Vicinal* fluorination is not dominant on conformational selectivity of MOF linkers. However, it has been shown to control flexibility. MOFs with linkers that have the desired flexibility can be synthesized. Furthermore, solvation effects can bias populations of MOF linkers and achieve conformational locking during the synthesis of MOFs containing these linkers. It should be acknowledged that there are more accurate approaches to quantify elastic properties of MOF that were beyond the scope of this work. Ortiz *et al.*[205] characterized the elastic properties of five different MOFs by calculating elastic constants tensors of each using DFT calculations with localized basis sets. A full tensorial analysis was then performed to derive quantities that characterized mechanical behaviour of the crystal. Among many quantities, Young's modulus, which characterizes deformation of an object along an axis was characterized.

The concept of conformational flexibility and biased populations (due to solvation effects) of the MOF linkers has implications in the computational construction and synthesis of MOF crystal structures. In the computational construction of MOF crystal structures, a large number of structures can be generated from possible combinations of nodes, judiciously designed linkers and structural arrangement. Further studies can then sort through the large number of hypothetical and

existing structures. This can guide the synthesis process towards promising candidates for particular applications, such as CO_2 adsorption. Computational screening using structure-property relationships can be used to evaluate MOFs for particular applications. Conformational flexibility and biased linker populations in solutions are just two of many parameters that can be used to evaluate a MOF for a particular application.[206] The generation and prediction of a large number of structures is beyond the scope this work. A different procedure is employed in Chapter 4, that constructs computation-ready MOF structures that are generated by manipulating atomic positions in existing structures, for example, computational substitution. By using the manipulated and modified structures, or by using crystal structure prediction, parameters such as linker conformations and flexibility can be incorporated to come up with noble frameworks that can be further characterized. Furthermore, the extent of flexibility in a linker can be controlled by *vicinally* fluorinating linkers.

4

The effect of difluorination on dicarboxylic and dipyridyl linkers in a Metal Organic Framework

Thus far, the study of metal-organic frameworks (MOFs) has been limited to isolated linkers. Despite the insight and the affordability that accurate quantum mechanical calculations provide, the adsorption of gas molecules in MOFs has not been addressed. In the study of the frameworks themselves, the type and scale of the problem that presents itself is different. Different computational methods are therefore required to be used, and the limitations thereof ought to be known and addressed. In this chapter, plane-wave DFT was employed to effectively describe the periodicity of the frameworks. Unlike in the previous study, *classical potentials* are also employed for the prediction of adsorption isotherms.

This chapter is concerned with the study of adsorption of CO_2 in MOFs. Small scale calculations, of not more than 30 atoms, of CO_2-ligand interaction energies is done using reliable *ab initio* methods. This provides insight into the strength and nature of interactions of non-fluorinated ligands compared to their fluorinated counterparts, as well as probable binding sites. Understanding the CO_2-ligand interactions with the various bridging ligands is also useful for the design of novel materials that effectively capture CO_2 gas. Adsorption isotherms of non-fluorinated MOFs and their fluorinated counterparts are predicted using GCMC simulations. The chapter also focuses on the effect of difluorination on the adsorption capacities of the frameworks containing the fluorinated bridging ligands. In addition to *vicinal* fluorination, various other difluorination patterns are explored, for an extensive comparative study of the effect of difluorination on adsorption capacities of MOFs.

4.1 Computational details

4.1.1 Structural details

Using the ABCluster software,[207] multiple different CO2-ligand conformations were generated. ABCluster uses a swarm intelligence algorithm called the artificial bee colony (ABC),[208] to search through conformational space for optimal (low energy) molecular clusters. It is inspired by the behaviour of bee swarms as they forage for food. ABCluster was employed to generate geometries that are close to a minimum, instead of manually building CO2-ligand conformations, which can lead to conformations that are far from a minimum.

The crystal structure of $\{Cu_2(Glu)_2(\mu\text{-bpa})\}\cdot(CH_3CN)]_n$ (Glu = glutarate, bpa = 1,2-bis(4-pyridyl)ethane (Cu-MOF), as shown in Figure (4.1), is based on experimental work reported by Hwang and co-workers.[183] This MOF was chosen because it contains linkers that were previously studied. The Cu-based MOF contains Cu_2 dinuclear units connected by glutarates and bipyridyl ligands and has been shown to selectively adsorbs CO_2 over H_2 and N_2.

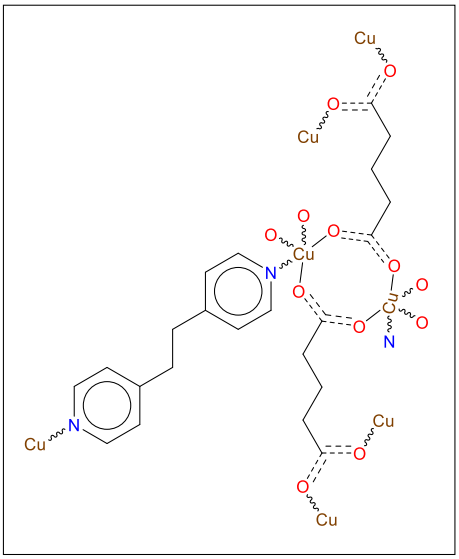

Figure 4.1 *Crystal structure of Cu-MOF, based on experimental work and used in this study as a non-fluorinated MOF analogue.*

Unlike the linkers studied in Chapter 3, the MOF linkers in Cu-MOF are conformationally locked in a certain conformation; the dicarboxylic acid groups and bipyridyl groups in the *anti* position. Therefore, only conformation with these groups in the *anti* position will be focused on in this chapter. No further conformational analysis will be performed.

4.1.2 Gaussian calculations

The CO_2-ligand geometries were optimized at a PBE-D3(BJ)/def2-SVP level of theory, with an empirical dispersion correction to address dispersion interactions. The interaction energies of the CO_2-ligand geometries were calculated at a DSD-PBEP86-D3(BJ)/def2QZVP level of theory. The DSD-PBEP86-D3(BJ) functional is a dispersion-corrected, spin-component scaled, double-hybrid fifth-rung functional, employed to address dispersion interactions in the CO_2-ligand clusters.[209] During development and benchmarking of PBEP86, the def2 family of basis sets were employed, hence the decision to switch to def2-SVP in this part of the study.[209,210] The counterpoise method implemented in the Gaussian software was employed to account for basis set superposition error (BSSE).[211] A basis set superposition error in studies of clusters, manifests as an artificial shortening of intermolecular distances and a concomitant artificial strengthening of the intermolecular interactions.

To gain a complete physical understanding of the interaction between the non-bonded CO_2 molecules and the various functionalized ligands, the widely used Symmetry Adapted Perturbation Theory (SAPT)[212] was employed. The SAPT approach provides, in addition to interaction energy between two molecules, decomposition of the interaction into physically meaningful energetic components consisting of electrostatic, exchange, induction and dispersion. The electrostatic contribution includes permanent multipolar type interactions, as well as charge cloud interactions. The exchange part is the repulsive force due to the quantum exchange phenomenon. The induction interaction arises from the polarization of each monomer responding to each other's electric field. Induction also includes charge transfer (CT), although the regular SAPT partitioning does not separate the two. However, CT can be estimated by calculating the induction contribution using a monomer and dimer centred basis set, but as charge transfer is

expected to be minimal in this case, this was not done. Dispersion is the attractive force resulting from a shift in electron density of atoms in each monomer, and a consequent correlation of the induced multipole moments. The interaction energy is given as a perturbation series, and the size of the series is governed by the accuracy one wants to achieve, the system size under study and the nature of the molecular system. A Hamiltonian of the two monomers is partitioned as shown in Equation (4.1).

$$\hat{H} = F_1 + W_1 + F_2 + W_2 + V \tag{4.1}$$

where F_1 and F_2 are the Fock operator for each monomer, W_1 and W_2 are the fluctuation potentials associated with each monomer and V is the interaction potential. The level of the truncation for the perturbation series is denoted by $E^{(nl)}$, where *n* indicates the order of the interaction potential, and *l* indicates the order of the fluctuation potential of the monomers. The simplest truncation that can be made is SAPT0 and it is defined by Equation (4.2).

$$E_{SAPT0} = E^{10}_{electrostatics} + E^{10}_{exchange} + E^{20}_{induction,resp} + E^{20}_{dispersion} + E^{20}_{exchange-induction} + \delta^2_{HF} \tag{4.2}$$

The subscript *resp* refers to the inclusion of orbital relaxation effects. The term δ^2_{HF} is included in the definition to take into account higher-order induction effects. The level of truncation employed in this work is SAPT2+, which is defined by Equation (4.3).

$$E_{SAPT0} = E_{SAPT0} + \underbrace{E^{12}_{electrostatics,resp} + E^{11}_{exchange} + E^{12}_{exchange} + {}^{t}E^{22}_{induction}}_{\mathrm{E_{SAPT2}}} + E^{21}_{dispersion} + E^{22}_{dispersion} \tag{4.2}$$

The Materials Studio (MS) CASTEP module was utilized to perform fully periodic DFT calculations – cell optimizations of the Cu-MOF and its fluorinated analogues. CASTEP employs a plane-wave basis set to calculate electronic properties of periodic systems.[213] The GGA approximation of PBE in combination with the Tkachenko-Scheffler method for dispersion

correction (DFT-D) was employed, using on-the-fly-generated (OTFG) ultra-soft pseudopotentials.[214] OTFG pseudopotentials have been developed in order to minimize the error with respect to fully converged all-electron DFT calculations.[215] (DFT-D) was used to study all MOF systems to account for dispersion interactions which are important when considering weak intermolecular interactions. A plane wave basis set cut-off energy of 571.4 eV with *k*-point sampling at the Γ-point was used to optimize unit cell lattice vectors with cell optimization convergence thresholds for energy change and maximum force of 1.0×10^{-5} eV/atom and 0.03 eV/ Å respectively.

4.1.3 GCMC Method

To calculate the adsorption of CO_2, H_2 and N_2 in the optimized frameworks as a function of pressure and temperature, the forcefield based grand-canonical Monte Carlo (GCMC) simulation tool, *Sorption,* within MS was used. GCMC simulations of CO_2 adsorption were carried out at 196 K, 273 K and 298 K, while H_2 and N_2 adsorption were carried out at 77 K, following the methodology of Hwang *et al.*[183] The generic parameters of the COMPASS forcefield implemented within MS were used to predict the adsorption isotherms. COMPASS is an *ab initio* forcefield that is able to accurately and simultaneously predict gas-phase and solid-phase properties for a broad range of molecules, including coordination polymers, such as MOFs. Partial charges obtained from the cell optimization calculation using the PBE functional were assigned to the adsorbent. One hundred thousand equilibration steps were followed by one million production steps.

In addition to the predicted adsorption isotherms, isosteric heats of adsorption (q_{st}) were also calculated and they could be directly compared to experimental data. The values of q_{st} (defined in MS as the partial molar enthalpy of the adsorbate in the reservoir minus that in the framework) are determined by using a post-processing GCMC subroutine in MS's Sorption module.[216,217] To calculate CO_2 q_{st} values, MS uses average values of the system energy and number of adsorbate molecules obtained during the GCMC simulation to evaluate the Clausius-Clapeyron equation in the grand canonical ensemble. Density fields of the sorbates obtained from the simulations were analysed in order to investigate the energetically most favourable adsorption sites.

4.2 Systematic computational study of the frameworks

4.2.1 Computational fluorination of framework linkers

To investigate the structural and adsorption properties of MOFs upon fluorination, various computational fluorination patterns were explored as shown in Figure (4.2). This systematic investigation via various fluorination patterns allows a tailoring of electronic properties of MOFs that best improve the adsorption capacity. Computational fluorination of linkers involved the computational substitution of hydrogen atoms with fluorine atoms.

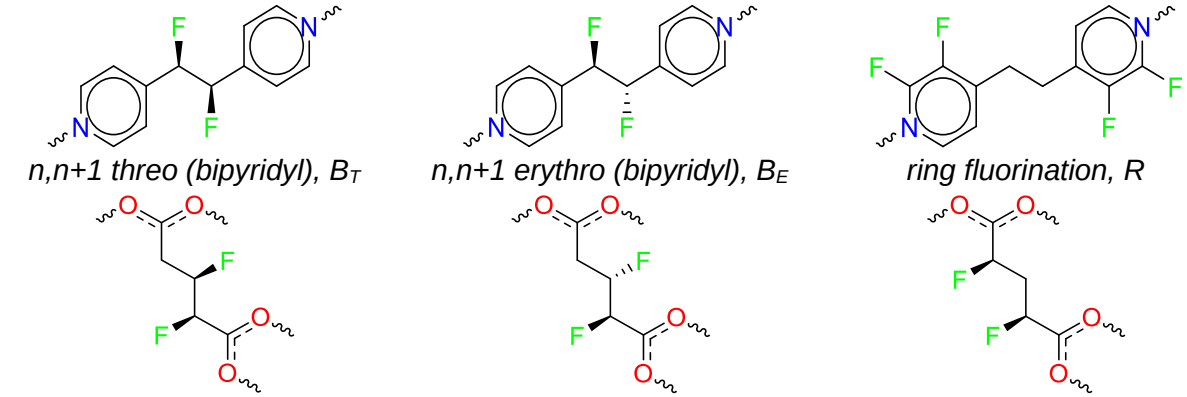

Figure 4.2 *A chemical diagram of the various fluorination patterns explored in this work.*

The *n,n+1* fluorination pattern follows from the study of the isolated linkers in the previous chapter. The fluorine atoms in *n,n+1* are, however, not exposed to the pore surface of the framework with the *n,n+1* fluorination pattern as shown in Figure (4.3a). In Figure (4.3), Connolly surfaces of the framework are visualized by using a probe radius of 1.65 Å, the kinetic radius of carbon dioxide.

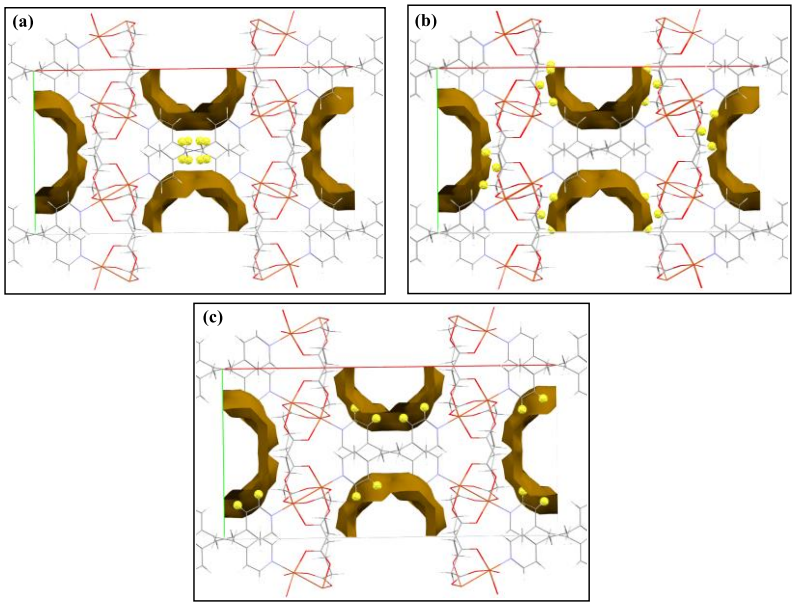

Figure 4.3 *Connolly surfaces(bronze) with a probe radius of 1.65 Å. (a) n,n+1 fluorination on the bipyridyl ligand linker. (b) n,n+1 and n,n+2 fluorination on the dicarboxylic ligand linker. (c) Partial ring fluorination. The fluorine atoms are shown in yellow.*

Non-exposure of the fluorine atoms to the channel surface suggests that there will be little to no interactions of the exposed fluorine atoms with gas molecules introduced into the channels. Using the *n,n+1* motif on the dicarboxylic ligand on the other hand, does expose the fluorine atoms to the channel surface, and since the dicarboxylic ligand linker has three carbons instead of two, *n,n+2* fluorination (shown in Figure (4.3b)) could also be explored. However, in literature, partial fluorination of MOFs usually occurs on aromatic rings and not linkers.[218] As a result, this common fluorination pattern (shown in Figure (4.3c) was undertaken for purposes of comparison. The geometries of the resulting fluorinated MOF analogues were then optimized, and the optimized structures utilized for analysis.

4.2.2 Geometry optimization

To study the adsorption of the non-fluorinated desolvated MOF and its fluorinated analogues, a full cell optimization of the shape, volume and lattice parameters was performed after computational fluorination. Even after crystallographic structure refinement of a known structure,

the geometry of the crystal structure should still be optimized to obtain strain free lattice parameters, atomic coordinates, and the ground state crystal structure. Comparable lattice parameters and atomic coordinates of the experimental crystal structure and the optimized structure provide support in favour of the DFT exchange-correlation functional, optimization constraints and the pseudopotential used in the calculation. Moreover, the lattice parameters of the optimized non-fluorinated crystal structure can be directly compared to optimized crystal structures of the fluorinated analogues.

The most commonly used quantitative measure of the similarity between the superimposed atomic coordinates of the optimized structure and the experimentally determined structure, is the root mean square deviation (RMSD) presented in Å.[219] The RMSD value measures the average change in displacement of a selection of atoms for a particular structure (geometrically optimized structure in this case) with respect to a reference structure (the experimentally determined structure in this case). In molecular docking, an RMSD value of 1-3 Å is acceptable, while a value of less than 2 Å is ideal.[220] Figure (4.4) shows an overlay of molecular fragments from the experimentally determined crystal structure and the optimized crystal structure of Cu-MOF. The RMSD for the overlay was calculated to be 0.13 Å using *Mercury*,[221] which is indicative of the close agreement of experimental lattice parameters and the optimized parameters, providing further support that the computational procedure is the correct choice for this study.

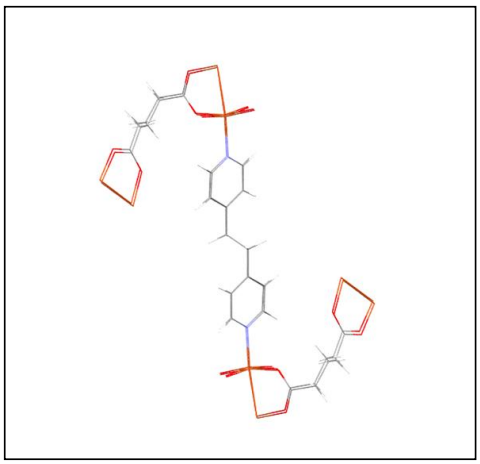

Figure 4.4 *An overlay of molecular fragments in the experimentally determined structure and the optimized structure, with an RMSD value of 0.13 Å.*

Appendix V shows the lattice parameters of the experimentally determined structure, the optimized structure and its various fluorinated analogues.

4.3 Cell volume changes upon fluorination

The fluorination of the linkers in the framework is accompanied by the reduction and expansion of the cell volumes, as the electron environment is changed by newly introduced fluorine atoms. Table (4-1) shows the cell volumes and cell densities of various frameworks after geometry optimization.

Table 4-1 *Cell volumes and cell densities of the experimentally determined Cu-MOF, the optimized Cu-MOF and its various fluorinated analogues, with the naming scheme shown in Figure (4.2)*

	Cu-MOF	B_T	B_E	D_T	D_E	***R***	$D_{n,n+2}$
Cell volume ($Å^3$)	2978.75	3027.89	2961.37	3083.65	2976.09	2920.72	2996.46
Cell density ($g.cm^{-3}$)	1.274	1.333	1.363	1.386	1.465	1.463	1.426

The cell volumes of the fluorinated analogues are larger than the optimized non-fluorinated analogue, except for the cell volumes of B_E, D_E and R. The lattice expansion is attributed to the introduction of the larger fluorine atom. In addition, the polarisation of the C-F bond leads to geometric changes in hydrocarbons, which follows directly from electron density shifts in the bonds. Valence shell electron pair repulsion (VSEPR) theory can be used to rationalize these shifts. Fluorination leads to the widening of the C-C-C angle and the consequent narrowing of the F/H-C-H/F angle from propane to 2-fluoropropane and then to 2,2-difluoropropane, as shown in Figure (4.5).[222]

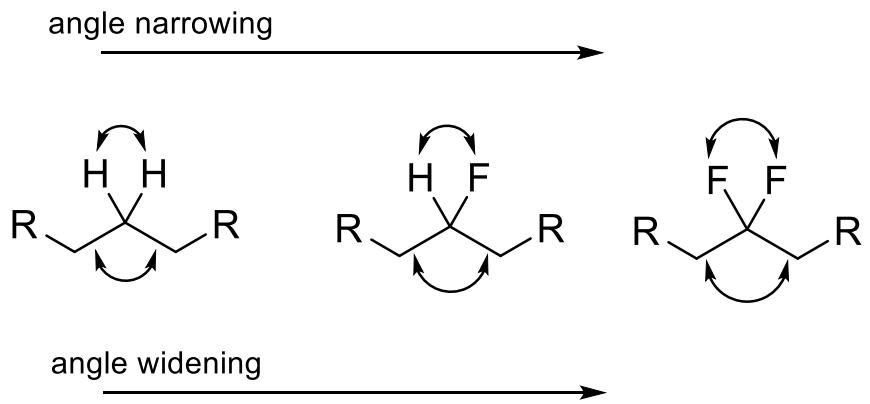

Figure 4.5 *A sketch showing the C-C-C angle widening and the consequent H-C-H angle narrowing upon fluorination*

The relatively electron rich C-C and C-H bonds repel each other in comparison to the relatively electron-deficient C-F bond, which should then close the F/H-C-H/F angle. The F/H-C-H/F angle narrowing occurs despite the high charge density and the lone pairs on the fluorine atom. The H-C-F angle is still narrower compared to the ideal 109.5° angle commonly observed in tetrahedral molecules, as expected in VSEPR theory. This widening of the C-C-C and H-C-F angle might be an additional reason for the unit cell expansion observed in some computationally fluorinated analogues, the other reason being the bigger size of fluorine atoms. Figure (4.6) shows a sketch of C-C-C and F/H-C-H/F angles in the non-fluorinated analogue and in the fluorinated analogues of the framework linkers. The angles are given in Table (4-2).

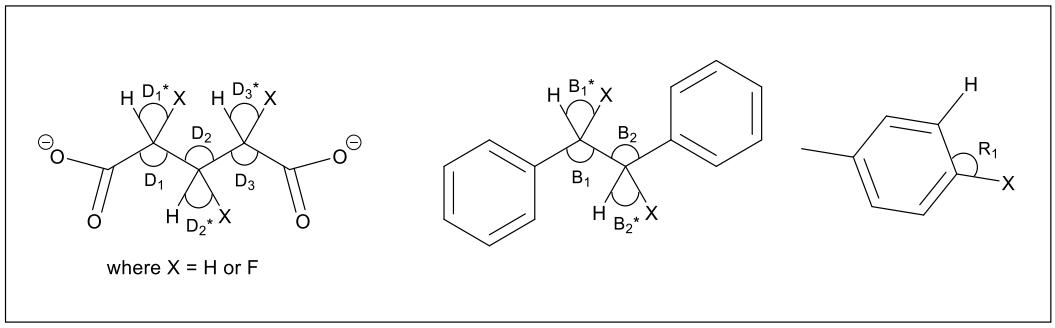

Figure 4.6 *A sketch of C-C-C and H-C-H/H-C-F angles of the framework linkers.*

Table 4-2 C-C-C and H-C-H/H-C-F angles for the non-fluorinated and various fluorinated analogues

Cu-MOF Analogue	*C-C-C angle (°)*	*F/H-C-H/F angle (°)*
Non-fluorinated	B_1= B_2: 113.06 D_1: 112.79 D_2: 112.21 D_3: 116.06	B_1*= B_2*: 106.67 D_1*: 106.69 D_2*: 106.83 D_3*: 107.19 R_1: 121.33
B_E	B_1 = B_2: 114.01	B_1*= B_2*: 107.48
B_T	B_1: 114.99 B_2: 115.52	B_1*: 107.73 B_2*: 108.59
D_E	D_1: 116.21 D_2: 113.38 D_3: 115.13	D_1*: 108.00 D_2*: 106.71 D_3*: 107.66
D_T	D_1: 114.67 D_2: 113.52 D_3: 112.16	D_1*: 108.25; D_2*: 107.743 D_3*: 107.20
R		R_1: 119.20
$D_{n,n+2}$	D_1: 114.77 D_2: 115.21 D_3: 113.00	D_1*: 107.21 D_2*: 107.29 D_3*: 106.76

[a] *Angle-labelling according to Figure (4.6)*

The replacement of the hydrogen atom with the fluorine atom on the bipyridyl ligand leads to widening of both the C-C-C (B_1) and F/H-C-H/F (B_1*) angles (114.01° and 107.48° for the B_E; 114.99° and 108.59° for the B_T) compared to the non-fluorinated bipyridyl ligand (113.06° and 106.67°). This result agrees with the trend of angle widening of the C-C-C bond but not consistent with the angle narrowing of the F/H-C-H/F observed for propane and 2-fluoropropane. Of the bipyridyl ligand, the B_T analogue shows the largest increase in the cell volume, this is consistent with it showing the largest angle broadening when compared to the B_E analogues. For the $D_{n,n+2}$ analogue, there is a slight F/H-C-H/F angle (D_1*) widening, accompanied by a widening of the middle H-C-H angle (D_2*). The C-C-C angle widens for only one side of the ligand (D_1) and closes for the other side (D_3). In case of the $D_{n,n+2}$ analogue, there is a complex interplay of bond repulsion and attraction which overall leads to a slight increase in cell volume. The cell volume for D_E is similar to the cell volume of the non-fluorinated analogue. There is widening and narrowing of the

C-C-C angles (D_1 and D_2) and F/H-C-H/F angle (D_2*), respectively. The overall effect is a slight decrease in the unit cell volume. The D_T analogue shows a widening of both the C-C-C and F/H-C-H/F angles which is accompanied by a relatively significant unit cell volume increase. In all the dicarboxylic ligands, the D_3 angle consistently decreases while the D_3* angle consistently increases, albeit slightly. For the ring-fluorinated analogue, the H-C-C angle (R_1) of 121.33° shows a narrowing upon fluorination to 119.20°. This can serve as an explanation for the decrease in the unit cell volume observed upon fluorination.

An angle widening of both the C-C-C and F/H-C-H/F angles is observed in all analogues, except for dicarboxylic ligands which has a C-C-C angle narrowing on side of the ligand. This is not always apparent or reflected in the cell volumes, since the angle changes are not significant. However, the polarity of the C-F bond introduces electron density shifts, which manifests as structural changes, i.e. angle changes. A slight angle change in one part of the unit cell does not lead to a significant increase in the cell volume. However, these slight local changes may lead to other changes of the structure, such as changes on a small part of a cavity or the electronic environment of the binding site, that has an overall influence on the adsorption properties of the material. It is worth noting that the replacement of hydrogen with fluorine in medicinal chemistry is considered conservative, on steric grounds, due the similar sizes of hydrogen and fluorine.[86] However, such a replacement could have significant electronic factors which can dramatically change the properties of the molecule. The changes in cell volumes observed could therefore be as a result of both geometric and electronic grounds that can be rationalized by models such as VSEPR, steric repulsion, bent bond or hyperconjugation.[86]

4.4 Prediction of gas adsorption isotherms

4.4.1 CO_2 adsorption isotherms

The adsorption isotherms of the Cu-MOF and its fluorinated analogues at different temperatures were predicted using GCMC. A comparison between the experimental and simulated data was carried out to determine the validity of the methodology and to determine the accuracy of the

forcefield used, at 196 K, 273 K and 298 K. The agreement between the experimental and simulated data is fairly good over the pressure range, as shown in Figure (4.7).

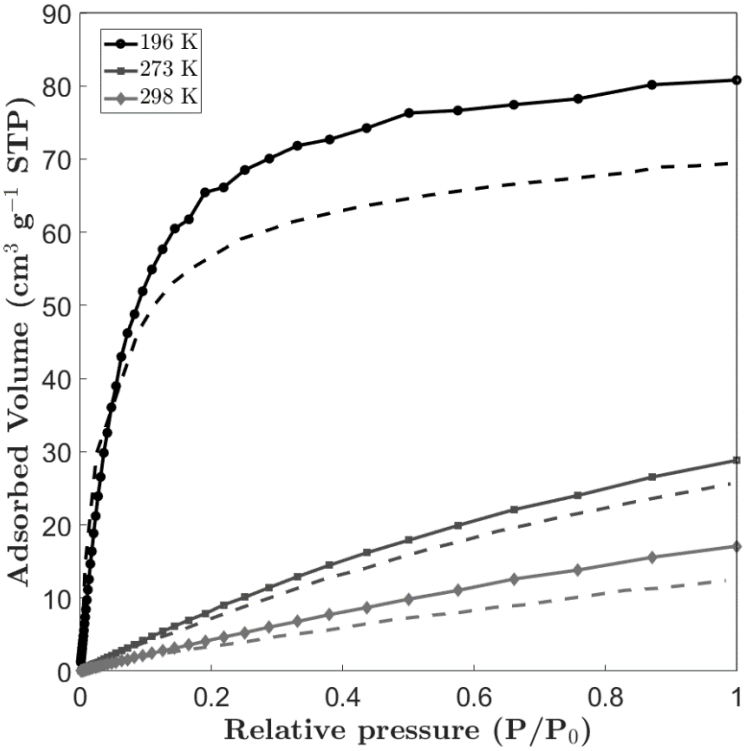

Figure 4.7 *Adsorption isotherms of CO_2 of the non-fluorinated Cu-MOF obtained experimentally (dashed line) and computationally (solid line) at 196 K, 273 K and 298 K.*

The experimental CO_2 capacity at 1 bar was found to be 70.0 cm^3 g^{-1}, 26.4 cm^3 g^{-1} and 12.7 cm^3 g^{-1} at 196 K, 273 K and 298 K, respectively. The simulated CO_2 capacity was found to be 81.47 cm^3 g^{-1}, 28.25 cm^3 g^{-1} and 16.27 cm^3 g^{-1} at 196 K, 273 K and 298 K, respectively. Furthermore, the type I shapes[223] of the isotherms, confirming the micro-porosity of the MOF, are also reproduced by the simulation. The agreement between experiment and computation is acceptable (with errors of 14%, 7% and 22%), considering the fact that the forcefield parameters were not optimized for this particular MOF. The discrepancies between the experimental and simulated data may be attributed to the fact that the computationally desolvated and optimized crystal structure that was used in the simulation is not a perfect representation of the synthesized crystal. For example, some binding sites might have been blocked during the activation process.

In the simulation, a desolvated phase of the crystal structure is used, therefore adsorbates have access to previously blocked binding sites.[224] Another possible source of discrepancy is that the adsorbate-adsorbent interaction energies of the desolvated crystal structure are not the same as the experimental structure, due to the computational desolvation of coordinated solvent molecules.

4.4.2 Isosteric heats of CO_2 adsorption

The isosteric heat of adsorption is a unique thermodynamic characteristic of the interaction strength between an adsorbate and a solid adsorbent. It is often used for porous materials as a characterization parameter. Comparing CO_2 q_{st} from experimental and simulated data can further validate the methodology and forcefield employed to predict adsorption isotherms. Experimental CO_2 q_{st} values were obtained from work by Hwang *et al.*[183] In their case, CO_2 q_{st} values were indirectly evaluated by applying the Clausius-Clapeyron equation to adsorption isotherms measured at different temperatures. Figure (4.8) shows the experimental and simulated CO_2 q_{st}.

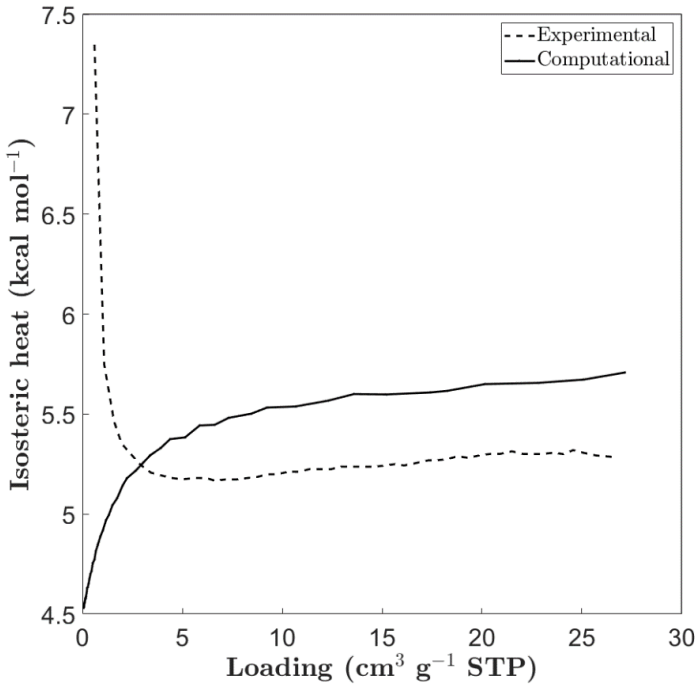

Figure 4.8 *q_{st} values of the non-fluorinated MOF calculated using experimental data (dots) and simulated data (solid line) at various CO_2 loadings.*

The q_{st} values from simulation underestimate the experimental data by ~3 kcal mol^{-1} at low coverage and by ~0.5 kcal mol^{-1} at high surface coverage. Nevertheless, both q_{st} values are in the usual range observed for CO_2 adsorption in MOFs.[225] In the experimental case, there is a substantial decrease of q_{st} at low coverages. At the high surface coverage region, q_{st} plateaus to a value of ~5 kcal mol^{-1}. Contrarily in the simulated case, a gradual ascent of the q_{st} values in the low surface coverage region is observed. However, at high coverages, q_{st} once again plateaus to a value of ~5.5 kcal mol^{-1}. Therefore, the strength of the interaction energies at high coverage is overestimated by the simulation. This result is reflected by the overestimation of uptakes in the plateau region of the adsorption isotherms. The initial gradual ascent suggests a strong attractive interaction of new incoming CO_2 molecules with the pre-adsorbed CO_2 molecules in the simulation.[226] The large discrepancies of q_{st} in the low coverage region can be explained by the lack of surface heterogeneity in simulations. Solid surface areas are never ideally regular. Regular, in this case, means that solid surface areas are not geometrically and energetically homogeneous.[227] The initial q_{st} descent observed in the experimental case is a reflection of the binding site heterogeneity, which reduces the deliverable gas uptake capacity. On the other hand, GCMC methods are based on idealized models that do not capture the specifics of surface morphology. As a result, an increase in q_{st} at low surface coverages is observed, because of the absence of an energetic penalty accompanied by surface heterogeneity.

4.4.3 Probable CO_2 binding sites

Regions of low potential energy and therefore the strength of different binding sites can be inferred from q_{st} curves. For example, at low adsorbate concentrations, molecules usually occupy positions of minimum potential energy at the pore walls, this shows up as minima on q_{st} curves.[228] At higher densities, molecules tend to be adsorbed closer to the pore centre and consequently the adsorbate-adsorbate interactions increase. This is indicated by maxima at high surface coverage regions of the q_{st} curve. For q_{st} curves with no maxima or minima, sites of adsorption cannot be inferred from the curve. In addition to the CO_2-CO_2 interactions, the gradual increase in q_{st}, observed in the simulated case, suggests an existence of active sites on the material surface. The probable position and the strength of a specific binding site can be determined by mass density maps and potential energy fields. Figure (4.9) shows a mass density map of the adsorbed CO_2, with pores visualized by using a solvent-accessible

Connolly surface. The mass density map is used to identify probable binding sites. Denser sites (blue regions) indicate more probable binding sites.

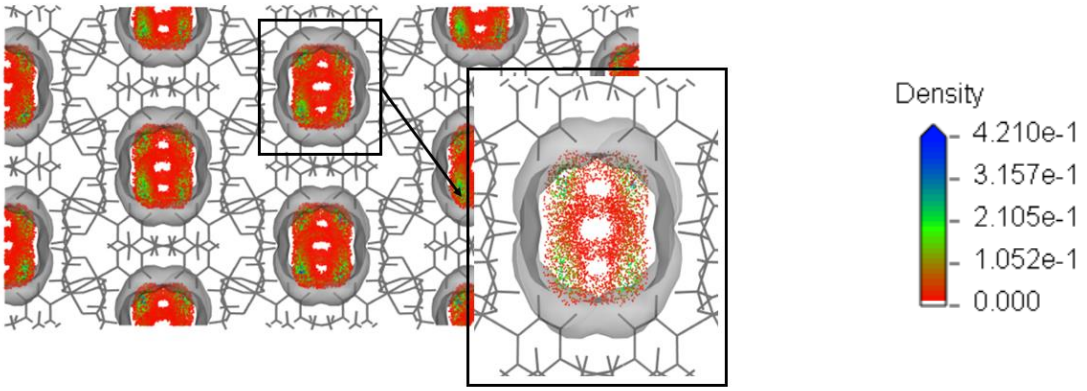

Figure 4.9 *Mass density map (average CO_2 count per $Å^{-3}$) of CO_2 in the Cu-MOF at 1 bar/196 K. Pores are visualized by using a solvent-accessible Connolly surface calculated at a probe radius of 1.65 Å.*

At a pressure of 1 bar and temperature of 196 K, the mass density map shows four regions of high density per cavity, suggesting the existence of four probable binding sites. The binding sites are positioned at or near the MOF surface. Regions of low density exist towards the pore centre, where adsorbate-adsorbate interactions are likely to take place. Mass density maps are usually used as a starting point for more accurate methods of locating binding sites. Once a probable binding site is identified, explicit adsorbate molecules can be placed and their conformation and interaction energy with the surface determined. However, geometrically optimizing placed adsorbate molecules in the pores of MOFs with typically 200-400 atoms a unit cell, can rapidly become expensive. Rather, finite structures can be used to study the binding modes adopted by the adsorbate molecules and the strength of the interaction with the MOF.

Figure (4.10) shows a potential energy field of CO_2 adsorption at a pressure of 1 bar and temperature of 196 K. The field quantifies the strengths of the short-range interaction forces involved in the adsorption process. Higher potential (in magnitude) regions indicate stronger interaction energies, whereas lower potential regions indicate weaker interaction energies.

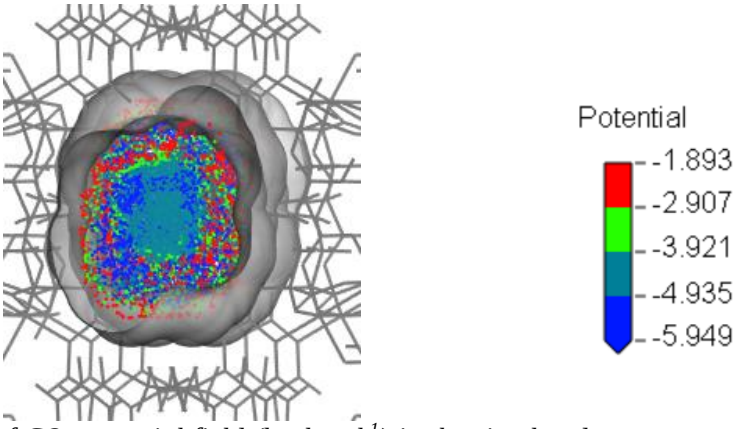

Figure 4.10 *Snapshots of CO_2 potential field (kcal mol^{-1}) in the simulated pore structures at 1 bar/196 K. The potential energy field is coloured by blue-green-red. The grey isosurface is the Connolly surfaces calculated at a probe radius of 1.65 Å.*

Positions of potential minima exist at or near the walls, as indicated by the blue regions. This is consistent with the mass density map, where the denser regions exist at or near the pore surface. These regions are occupied by the first molecules adsorbed. At higher uptakes, molecules tend to be adsorbed closer to the pore centre, and consequently, the adsorbate-absorbent interactions decrease. Consequently, there are significant interactions occurring towards the pore centre, as shown by the turquoise blue regions.

4.4.4 H_2 and N_2 adsorption isotherms

In addition to CO_2 sorption studies, *Hwang et al.*[183] performed H_2 and N_2 sorption studies as well. They discovered that Cu-MOF selectively sorbs CO_2 over H_2 and N_2. However, in this work, the adsorption simulations (done using the same computational procedure as explained earlier, for CO_2) predicted H_2 and N_2 uptakes (137.70 and 156.83 cm^3 g^{-1}, respectively, at 1 bar/77 K) that were not only much higher than experimentally determined values (12.89 and 10.17 cm^3 g^{-1}, respectively, at 1 bar), but also inverted in their ordering. The former can explained, in part, by the over estimation of the micropore volume or the surface area, and therefore the simulation of adsorbate molecules in areas of occluded volume that would not be accessible in the real crystal because of inaccessible pores or non-porous defects.[229–231] This over prediction essentially leads to significant 'false sorption' in the occluded pores. The simulated high uptakes of N_2 occur despite

its low quadrupole moment (-4.72 ± 0·26 × 10^{-40} C m^2; -13.4 ± 0·4 × 10^{-40} C m^2 for CO_2)[232] and low polarizability. The adsorption cooperative effects occurring in simulated micropores are exaggerated. Gregg and Sing[233] suggested that the first molecules being adsorbed enhance the adsorption affinity in the adsorption space (the accessible pore volume present in the pore) remaining, and thus complete micropore filling occurs, which becomes exaggerated for smaller molecules. This can also be proposed for H_2. The over estimation of gas uptake is not observed in the case of CO_2 because of the smaller sizes of H_2 and N_2. The smaller the adsorbent, the more likely it is to fit in an inaccessible pore or defect. Since the adsorption of microporous adsorbents, as shown by the type I shape of the isotherms in Figure (4.7), occurs by filling the micropores at higher pressures, the adsorbate rate depends on the accessible micropore volume rather than the total surface area. Therefore, the ratio of some theoretically determined volume parameter to the experimentally determined total pore volume will allow the scaling of the simulated data to fit the experimental data.[230,231] Ongari *et al.* [234] have shown that unlike other definitions of pore volumes, the occupiable pore volume can be directly related to the experimentally measured pore volumes from nitrogen isotherms. Figure (4.11) shows snapshots of H_2 and N_2 mass density and potential field in the simulated pore structures at 1 bar/77K. Connolly surfaces were also calculated with a probe radii of 1.445 Å and 1.820 Å, [235] the kinetic radii of H_2 and N_2, respectively.

The mass density maps of H_2 and N_2 show significant adsorption despite what the experimental data shows. Like the mass density of CO_2, the mass density of H_2 and N_2 has high-density regions at or near the pore walls and low-density regions away from the walls. Furthermore, the mass density map of N_2 shows distinct positions where the molecule is likely to be found and site specificity is therefore more pronounced in this case.

High potential regions near the pore wall are observed for H_2. This suggests repulsive interactions between the H_2 molecules and the pore wall. Low potential energy regions at the pore and towards the pore centre are also observed. However, the suggestive pore wall-H_2 interactions and H_2-H_2 interactions are not as strong as in the N_2 in magnitude. In the case of N_2, stronger interactions are observed, as indicated by the values of low potential regions on the potential energy field. A more extensive study of the interaction energies between the adsorbate and the framework needs to be

carried out to better understand the observed adsorption behaviour of H_2 and N_2. However, given the anomalous results for these adsorbents, only CO_2 will be used for further studies of fluorinated analogues, as presented in the next section.

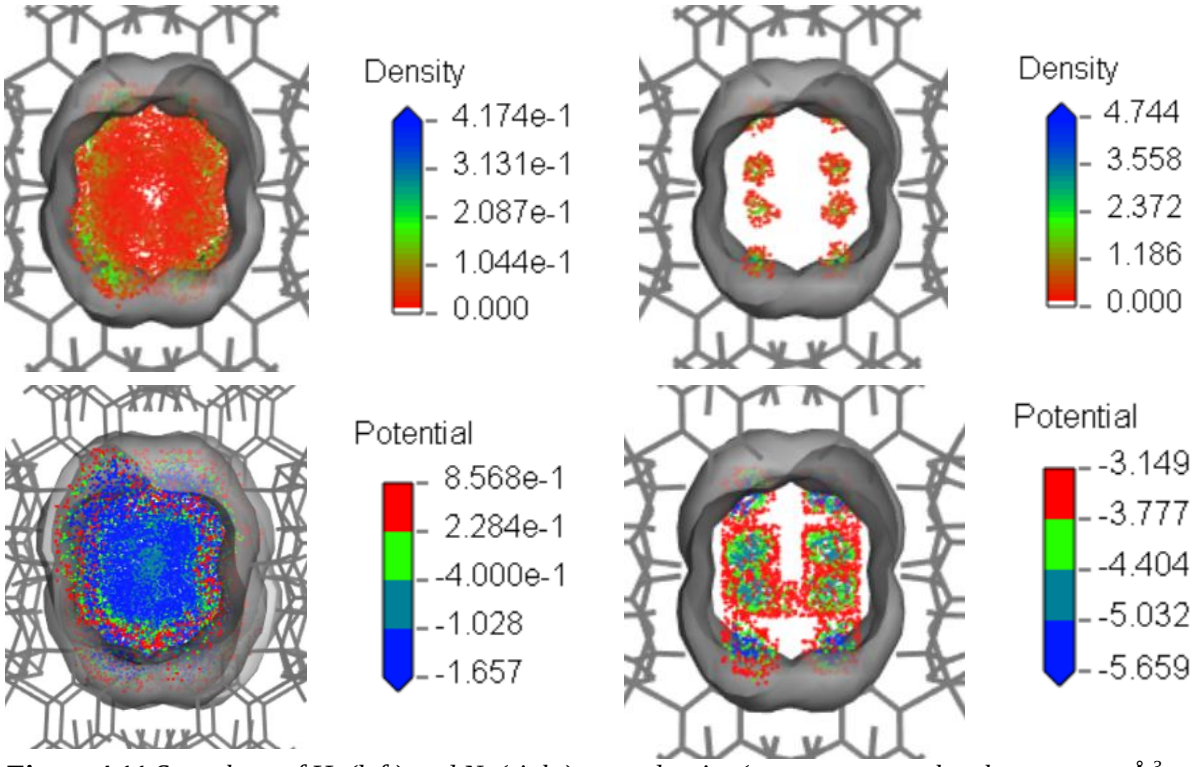

Figure 4.11 *Snapshots of H_2 (left) and N_2 (right) mass density (average gas molecule count per $Å^{-3}$, top) and potential energy fields (kcal mol^{-1}, bottom) in the simulated pore structures at 1 bar/77K. The field of adsorbed H_2 and N_2 molecules are shown in red, green and blue. Connolly surfaces are also shown.*

4.4.5 Fluorinated analogues of Cu-MOF

Figure (4.12) shows simulated CO_2 adsorption isotherms of all computationally fluorinated analogues at 196 K, 273 K and 298 K. Appendix VI shows the tabulated uptakes and percentage increases or decreases of uptakes upon fluorination.

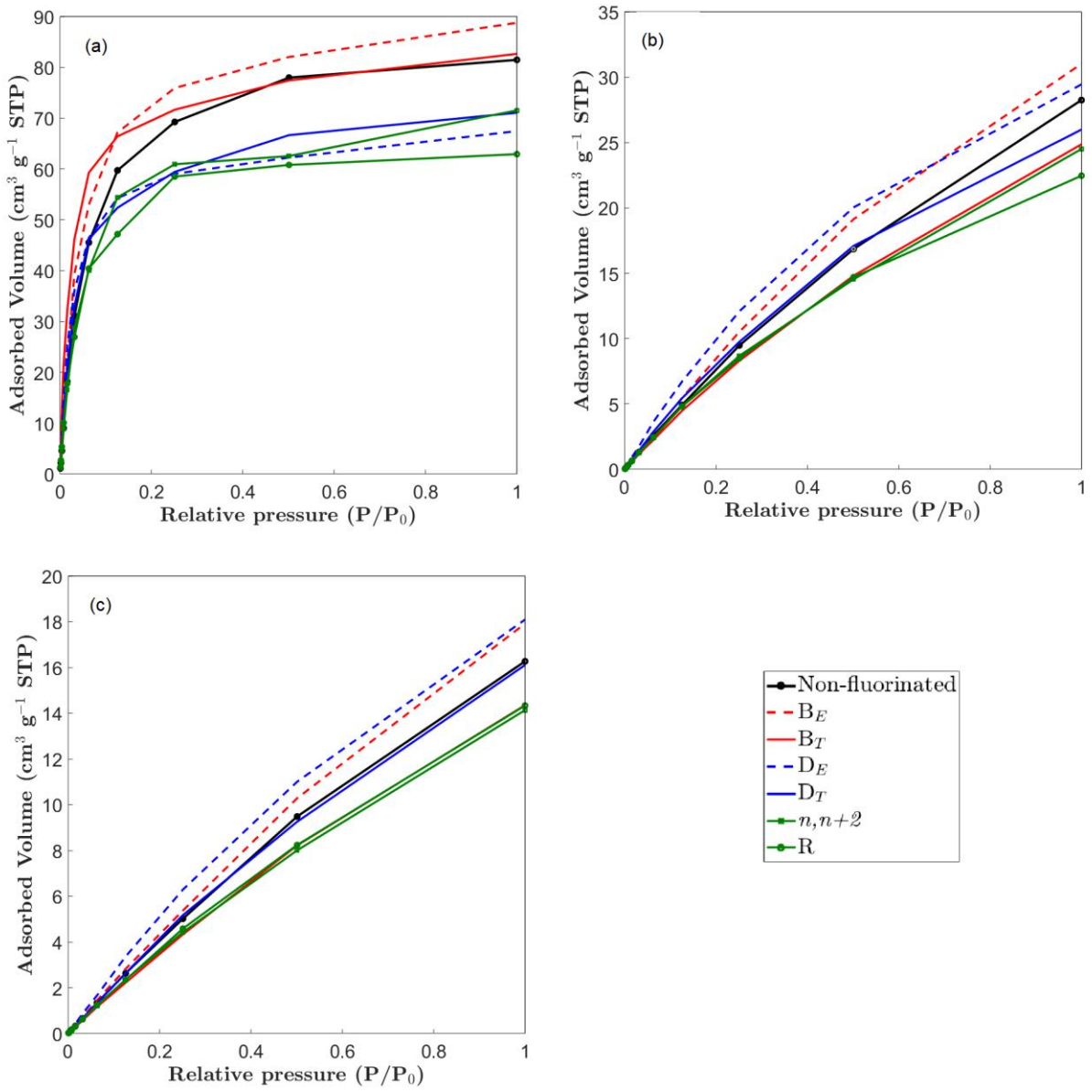

Figure 4.12 *CO_2 adsorption isotherms of all fluorinated analogues at (a) 196 K, (b) 273 K and (c) 298 K.*

What is seen is that some fluorination patterns lead to better adsorption compared to the non-fluorinated analogue, up to 10% better, whereas some fluorination patterns show a decrease of up to 23% in uptake. The D_T analogues shows the most increase of uptake at 196 K, whereas the R analogue shows the most decrease in uptake. At all three temperatures, the B_E analogue adsorbs CO_2 better than the non-fluorinated compound, while the D_T, R and $D_{n,n+2}$ analogues adsorbs worse. As the temperature decreases from 298 K to 196 K, the uptakes of the D_E, D_T, and R

analogues consistently decrease. On the other hand, the uptakes B_E, B_T and $D_{n,n+2}$ analogues do not change much with temperature. An exception is an increase in uptake at 196 K for the B_T analogue. At 196 K, the bipyridyl analogues generally show better adsorption than the dicarboxylic analogues, as expected according to Figure (4.3).

To further comprehend the observed adsorption of the fluorinated analogues, a correlation of micropores (or a related volume parameter such as the free volume calculated in MS) and the saturation amount (see Appendix VI) can be considered. Figure (4.13) shows a plot of uptakes of the various fluorinated compounds against the free volumes per unit cell. The free volume is the volume enclosed by a solvent-accessible surface area.

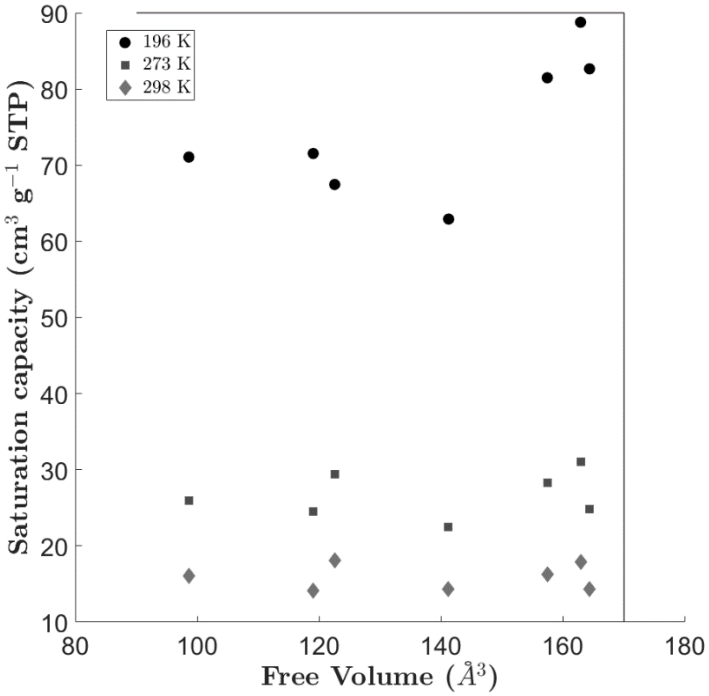

Figure 4.13 *A correlation of the adsorption saturation amounts against free volumes (calculated using MS with a probe radius of 1.65Å, the kinetic radius of CO_2) of various fluorinated analogues at 196 K, 273 K and 298 K.*

There is a weak linear correlation between the CO_2 uptake and the free volume, which improves from 298 K to 196 K. For some fluorination patterns, an increase in volume leads to an increase

in uptake, whereas for others it does not. To quantify the strength of linear association between .volume and uptake, Pearson's correlation coefficient, R, can be used. It attempts to draw a line of best fit through a dataset of two variables and then measure how far each data point in the data set is from this line of best fit. The R value quantifies the extent of an observed linear correlation. A high R value is a strong indication of a linear correlation. Table (4-3) shows the R coefficients at each temperature, with their associated p-values, calculated using 2016 Excel's statistical tools. A p-value measures by what extent the experimental data rejects the null hypothesis. It is the probability of an observation occurring by chance or error.[236] A statistical significance of 0.05 is typically defined, where p-values that are lower than 0.05 indicate strong evidence against the null hypothesis and p-values higher than 0.05 indicate strong evidence for the alternative hypothesis. For small sample sizes, p-values are looked up on statistical tables and reported as a range.

Table 4-3 *Pearson's correlation constants and Spearman's rank correlation at 196 K, 273 K and 298 K*

Temperature (K)	***Pearson's correlation, R***	***p-value***	***Spearman's rank correlation, ρ***	***p-value***
196	0.91	$p < 0.01$	0.86	$0.025 > p > 0.01$
273	0.55	$p > 0.10$	0.54	$p > 0.10$
298	0.55	$p > 0.10$	0.39	$p > 0.10$

At all temperatures, a positive linear correlation is observed. A very strong correlation at 196 K is observed, with an associated p-value that is smaller than 0.05. This suggests that an increase in free volume will lead to an increase in uptake. Furthermore, there is strong evidence that there is a linear correlation between free volume and uptake. In contrast, moderate correlation is observed at 273 K and 298 K. Moreover, high p-values indicate weak evidence that there is linear correlation in this case. That is, at these temperatures, there is high probability that there is no linear correlation between volume and uptake.

Another useful parameter to utilize is the Spearman's rank correlation, ρ, which quantifies the magnitude of the linear correlation and tests for a consistent change in a particular direction. A high ρ-value indicates that there is a strong correlation between the two variables of interest. Table (4-3) shows the ρ-values at each temperature, with their associated p-values, also calculated using

Excel. A high ρ-value at 196 K is seen, whereas low ρ-values are seen at 273 K and 298 K. A p-value that is smaller than 0.05 is also observed at 196 K and high p-values that are higher than 0.05 are seen for 273 K and 298 K. A strong linear correlation is suggested by the high ρ-value at 196 K. That is, at this temperature, the extent of change of the free volume will be accompanied by a proportionate change of the uptake. At 273 K and 298 K, the R values have already discredited any linear correlation between free volume uptake. The low ρ-value at these temperatures further supports this observation. It should be acknowledged that small sample sizes were used in the statistical analysis and therefore leads to suggestive and less conclusive results.

4.5 Quantum mechanical cluster calculations

4.5.1 CO_2 interaction energies with various fluorinated and non-fluorinated ligands

The CO_2-ligand cluster structures and interaction energies of CO_2 with the various ligands of different fluorination patterns are presented in Figure (4.14) and Table (4-4), respectively. Each cluster is made up of one CO_2 molecule and one ligand molecule. The conformations are considered in their neutral form. To ensure this for the dicarboxylate ligands, lithium atoms that coordinate to the carboxylate groups are used. Li^+ cations are commonly used to terminate carboxylate groups in models constructed to investigate adsorption in MOFs.[237–240] Of the low-energy conformations ABCluster generated, only structures that correspond to the lowest interaction energies are presented. The assumption here is that there is only one significant binding site. This does not provide a true and accurate picture of the energetic contributions to the enthalpy of adsorption, as well as the mechanism of adsorption. However, it provides a qualitative evaluation of the strength of the initial monomolecular adsorption of CO_2. This way, interaction strengths of each ligand with the CO_2 molecule can be compared to better understand the effects of fluorination.

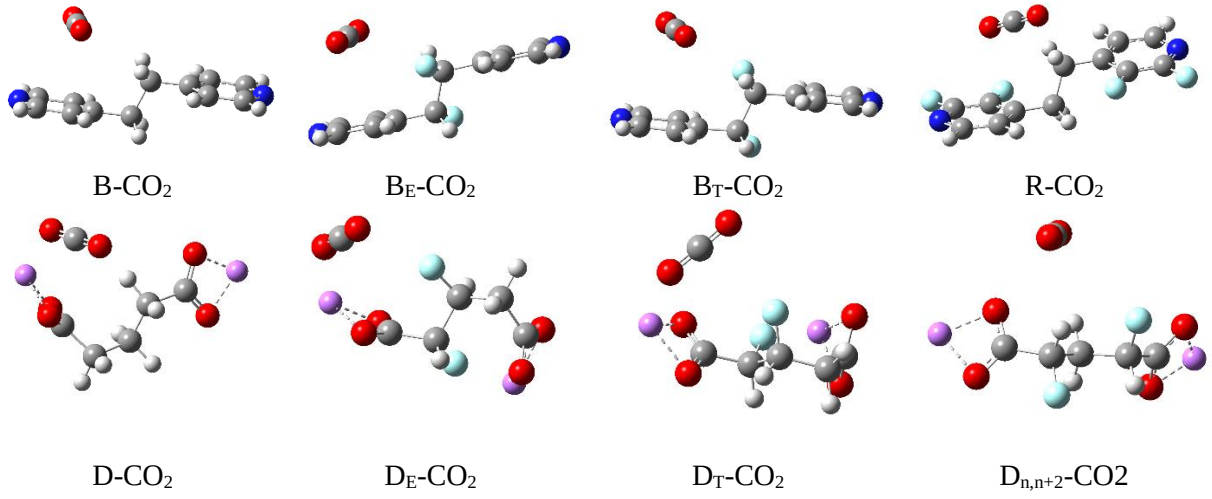

Figure 4.14 *Cluster structures of non-fluorinated ligands and various ligands of different fluorination patterns.*

Table 4-4 *PBEP86-D3(BJ)/Def2SVP CO_2-interaction energy (kcal mol^{-1}) with various ligands of different fluorination patterns*

Complex	***Interaction energy (kcal mol^{-1})***
B-CO_2	-1.67
B_E-CO_2	-3.00
B_T-CO_2	-3.19
D-CO_2	-9.88
D_E-CO_2	-11.03
D_T-CO_2	-11.09
R-CO_2	-2.22
$D_{n,n+2}$-CO2	-3.40

Upon *n,n+1* fluorination, an increase (in magnitude) in interaction energy is observed for both the bipyridyl and dicarboxylic ligand, with the dicarboxylic ligands showing stronger interactions with CO_2. The stronger interactions of the dicarboxylic ligands can be attributed to the terminal lithium atoms, which interact with the CO_2 molecule. A similar observation was made by Vogiatzis *et al.*,[240] where the interaction energy of benzene dicarboxylate with a CO_2 molecule was 1.6 kJ mol^{-1} (0.38 kcal mol^{-1}) smaller than benzene dicarboxylate with lithium ions. This slight increase in interaction energy persists when the bipyridyl ring is fluorinated. A slight decrease of interaction energy is observed upon *n,n+2* fluorination. With the type I isotherms observed in Figure (4.7), the strength of the interaction is expected to reflect the uptake of the gas, especially at low pressures and coverages where adsorbent-adsorbate interactions are more significant. At

low relative pressures, P/P_0 < ~0.1, the strength of the interaction energies of the ligand with the CO_2 molecule is reflected by the uptake at 196 K. This can be elucidated by zooming into the low-pressure region on the adsorption isotherm. Figure (4.15) shows the low-pressure region of an adsorption isotherm at 196 K.

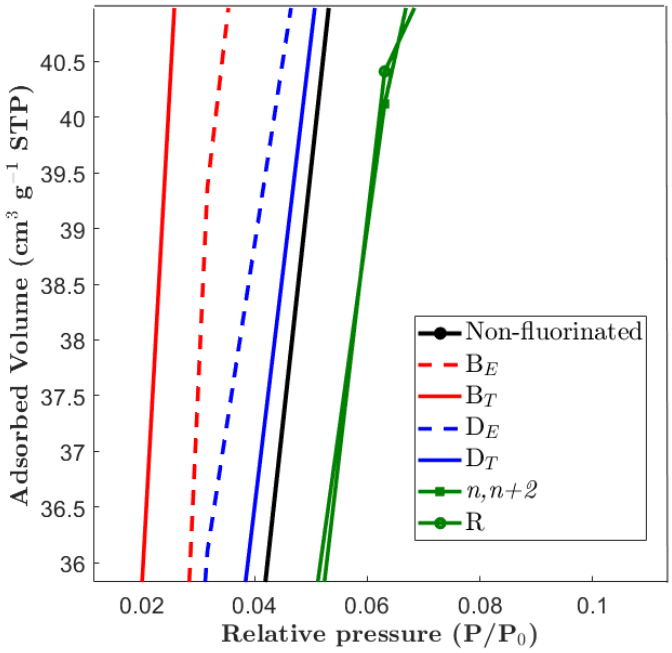

Figure 4.15 *Adsorbed gas volume at low relative pressure regions,* P/P_0 < ~*0.1.*

The R and $D_{n,n+2}$ analogues have lower uptakes than the non-fluorinated analogue at low pressures. This is consistent with the lowering of interaction energies upon fluorination. The *n,n+1* fluorinated analogues all adsorb better than the non-fluorinated ligands, and this is consistent with the larger interaction energies when they are compared to their non-fluorinated counterpart. The B_E and B_T analogues show the best adsorption at low-pressures. This is reflected in their interaction energies which doubled upon fluorination.

4.5.2 Energy decomposition of the interaction energy

A further energy decomposition of the interaction energy can provide insight into the types of interactions and therefore types of binding sites present on a pore surface. A decomposition of the

energetic contributions to the interaction energy was done using SAPT2+. The interaction energy decomposition comprises of electrostatic, exchange, induction and dispersion components, as outlined in Table (4-5). The total interaction energies of the cluster structures range from 2-11 kcal mol^{-1}, reinforcing physisorption as the type of adsorption that occurs. That is, the adsorption of gas molecules occurs via interactions such as the vdW interactions. On polar surfaces, multipolar interactions between CO_2 and the ligand become significant. The polar surface can interact with the large quadrupole moment of CO_2 gas. An inspection of the attractive electrostatic contributions can help elucidate polar interactions between the ligand and the gas molecule. Since the forces that bring about physisorption are predominantly dispersion and short-range repulsive forces (the exchange energy), a closer look at these individual components can elucidate their role in adsorption.

Table 4-5 *Energy decomposition of CO_2-ligand interaction energies. Molecular dipole moments of ligands are also included*

Complex (dipole moment)	*Electrostatic (kcal mol^{-1})*	*Exchange (kcal mol^{-1})*	*Induction (kcal mol^{-1})*	*Dispersion (kcal mol^{-1})*	*Total interaction (kcal mol^{-1})*
B-CO_2 (0.03)	-1.17	4.39	-0.54	-5.06	-2.39
B_E-CO_2 (0.03)	-2.75	4.02	-0.53	-4.78	-4.04
B_T-CO_2 (0.02)	-2.84	3.94	-0.53	-4.81	-4.25
D-CO_2 (0.18)	-11.06	11.20	-5.37	-4.15,	-9.38
D_E-CO_2 (0.15)	-9.94	8.96	-5.77	-3.44	-10.19
D_T-CO_2 (0.14)	-8.67	7.26	-5.58	-3.10	-10.09
R- CO_2 (0.02)	-1.78	2.51	-0.51	-2.96	-2.73
$D_{n,n+2}$- CO_2 (0.15)	-10.67	9.99	-5.59	-2.77	-9.05

The induction component, which mirrors polarizability of the ligand, does not undergo significant changes upon fluorination for both the bipyridyl ligand and the dicarboxylic ligand. This can be attributed to the low polarizability of the fluorine atom as suggested by its small size. Furthermore, it emphasizes the moderate change, on steric and electronic grounds, that the substitution of hydrogen with fluorine brings about. Upon *n,n+1* fluorination, a significant increase in electrostatic interactions is observed for the bipyridyl ligands which can be attributed to the introduction of the more polar C-F bond in the fluorinated species. However, the dicarboxylic ligands do not show an increase in electrostatic interactions upon *n,n+1* fluorination, despite the presence of the more polar C-F bond. A decrease in the dispersion component is observed for all the fluorination patterns explored. The decrease in dispersion interactions is not consistent with the improvement of adsorption capacities observed upon *n,n+1* fluorination. The dicarboxylic ligands also show a decrease in dispersion interactions upon *n,n+1* fluorination, and this is consistent with the lower adsorption capacities observed at 196 K. Upon *n,n+2* and ring fluorination, the decrease of dispersion interactions is consistent with the adsorption capacities observed at all temperatures.

4.6 Summary

Various fluorination patterns of Cu-MOF were explored, and it was discovered that, upon fluorination, the cell volume changes. These contractions and expansions of the unit cell were as a consequence of the structural property changes introduced by the fluorine atom. The changing cell volumes, and the consequent changing pore free volumes, were then used to account for sorption capacities in MOFs. Since the fluorine atom is only slightly larger than the hydrogen atom, the substitution of hydrogen with can be considered as conservative with respect to steric interactions. However, significant changes in the structural properties were seen in some cases of fluorination, as reflected by the adsorption capacities.

The functional and forcefield used (PBE and COMPASS, respectively) to optimize the geometry of the experimental structure and predict adsorption isotherms, respectively, were validated by

performing a comparative study of experimental and simulated data. The predicted adsorption uptakes were found to be similar to the experimental uptakes. This validated the functional and forcefield that were used in order to predict adsorption uptakes of the various fluorinated MOF analogues. The discrepancies between experimental CO_2 q_{st} and simulated q_{st} gave insight into the difference between the synthesized and simulated framework structures. For example, the initial gradual increase of experimental q_{st} values highlighted the presence of heterogeneous pore surfaces, which is not sufficiently captured by the simulation. In addition, the simulated q_{st} values are over-estimated by the simulation, therefore, the strengths of the interaction energies would also be over-estimated.

Probable CO_2 binding sites were also identified from a mass density map of the Cu-MOF adsorption. These sites exist at or near walls. In the case of the non-fluorinated Cu-MOF, four probable binding sites were identified. Identifying binding sites in this way provides a starting point to perform more accurate periodic calculations. Explicit adsorbate molecules can be placed on the probable binding sites and the conformation and strength of the adsorbate-adsorbent interactions investigated. This was beyond the scope of this work. The potential energy field highlighted 'energetic hotspots' in the pore structure. It was established that the density hotspots matched the potential energy hotspots, which further supported the identification of probable binding sites. Furthermore, the energetic hotspots provided, to an extent, insight into the mechanism of the adsorption. Strong interactions towards the centre of the pore in the CO_2 adsorption highlighted the strength of adsorbate-adsorbate interactions.

Adsorption isotherms of the various fluorinated MOF analogues were predicted using the same functional and forcefield as for the non-fluorinated analogue. Some fluorinated analogues were seen to adsorb better than the non-fluorinated analogue, and others were seen to have lower uptakes. An attempt to account for the uptakes observed by considering solvent-accessible free volume showed that, at some temperatures, volume alone is not enough to explain them. At 196 K, a strong linear correlation of free volume and gas uptake was observed, suggesting that in this case, free volume could be used to explain uptakes. At higher temperatures (273 K and 298 K), accounting for the observed gas uptakes was not possible. Gas uptakes could not be explained

by free volume and interaction energies alone. Energetic contributions to the absorptivity of CO_2 towards the Cu-MOF and its fluorinated analogues were also investigated. Finite structures of the MOF comprising the isolated ligand and CO_2 molecule were adopted to quantify the strength of the interaction energies. At 196 K, interaction energies between the ligand and the CO_2 molecule were seen to explain uptakes at low-pressure regions ($P/P_0 < 0.1$). The *n,n+1* fluorination of the bipyridyl ligand resulted in an increase in interaction energy at low pressures. Similarly, *n,n+1* fluorination on the dicarboxylic ligands showed an increase in gas uptake.

A methodology was established, where an existing MOF structure was manipulated by computational substitution and MOF structures that might be amenable to synthesis were identified. Exploring the different fluorination patterns served as screening for fluorinated MOF structures with improved adsorption properties. The methodology established is just a segue to a more extensive study of generating hypothetical structures and computationally characterizing them. More accurate methods, and often more computationally expensive, can be explored, where a large number of hypothetical structures can be generated. Furthermore, a larger energy landscape can be explored. These methods include the Monte Carlo simulation annealing and the automated assembly of secondary building units (AASBU).[241,242]

5

Closing comments

With the help of QM methods, a thorough investigation of the *vicinal* fluorination motif on conformational control was done. It was found that the fluorine *gauche* effect is not dominant in controlling conformations of some MOF linkers. Rather, an interplay of interactions, including solute and steric interactions, influence the conformational stability on rotational profiles. It has been shown, however, that *vicinal* fluorination can play a role in the flexibility of the linkers used in MOFs, as it influences the force constants around the minima in the rotational profiles. The study has also highlighted the importance of the solvent on the relative energies of the linker conformations—this has a potential impact on the synthetic strategies of MOFs containing these linkers and it warrants further investigation.

Vicinal fluorination was employed as a structural motif in MOFs containing linkers that were studied in isolation. Different fluorination patterns were explored, in addition. It was established that the introduction of the polar C-F bond led to cell volume changes. It was proposed that cell volume changes might mirror local structural changes, such a volume change of a cavity. CO_2 adsorption isotherms were predicted and a good agreement between the experimental and simulated data was seen. This validated the exchange-correlation functional and the forcefield used. CO_2 adsorption isotherms of the fluorinated analogues were also predicted and an attempt to account for the observed gas uptake was done. It was shown that for lower temperatures, *vicinal* fluorination can lead to higher gas uptake. Moreover, the gas uptakes can be predicted when considering interaction energies with specific ligands. At higher temperatures, interaction energies and free volume cannot be used alone to account for the observed gas uptakes.

The use of potential density maps assisted in identifying probable binding sites. This is only a starting point for a more extensive and involved study that includes explicitly placing gas

molecules in the framework and calculating interaction energies. The role of interaction energies can then be elucidated by using a more accurate model. Supercells would have to be employed in such a study. Therefore, computational methods that are suitable for such a large number of atoms in a calculation, such as linear-scaling methods would have to used.[243–245]

Appendix

Appendix I *Relative energies (kcal mol^{-1}) of low-energy conformers in various solvents calculated using different DFT functionals and the 6-311+G(d,p) basis set*

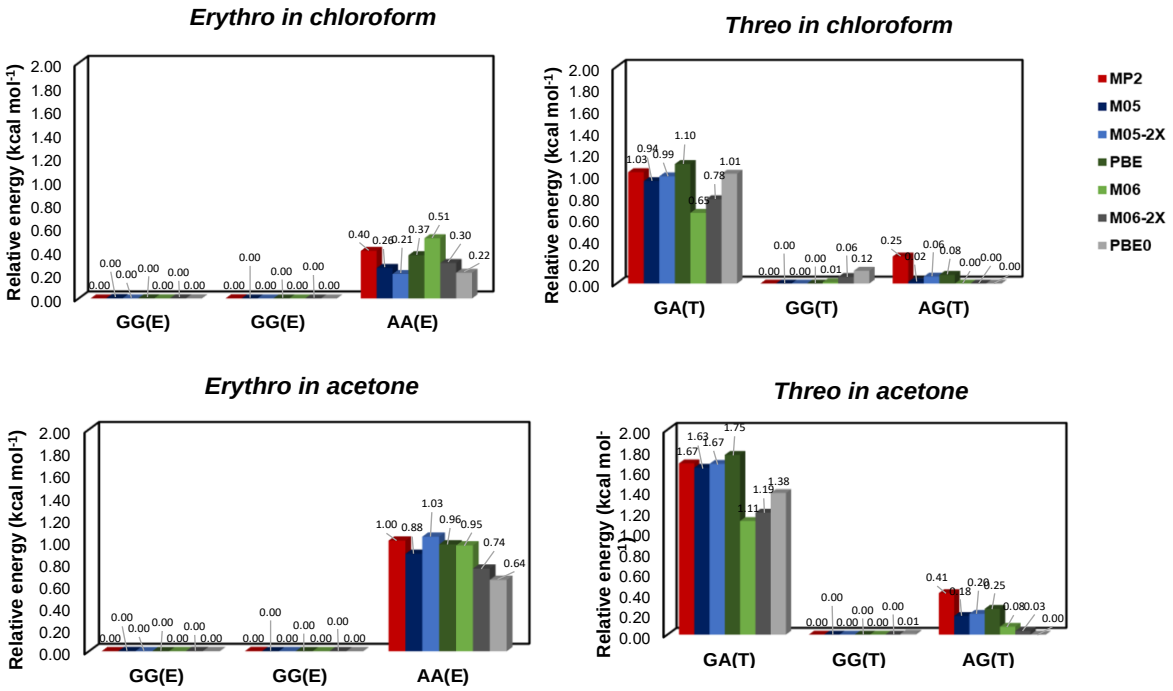

Appendix II *Mean absolute errors (kcal mol^{-1}) of various DFT functionals in different solvents, benchmarked against the MP2 method*

	M05	***M05-2X***	***M06***	***M06-2X***	***PBE***	***PBE0***
Water	0.06	0.04	0.15	0.18	0.05	0.18
Acetone	0.03	0.07	0.12	0.11	0.05	0.10
Chloroform	0.12	0.09	0.10	0.03	0.08	0.09
Vacuum	0.06	0.05	0.18	0.21	0.05	0.20
Average	0.07	0.06	0.14	0.13	0.05	0.14

Appendix III *Molecular dipole moments of 2,3-difluorobutane in water, acetone, chloroform and in vacuo calculated using different DFT functionals*

		MP2	**M05-2X**	**M05**	**PBE**
Water	**GG(E)**	4.91	4.75	4.61	4.54
	AA(E)	0.00	0.00	0.00	0.00
	GG(T)	5.17	5.02	-	4.94
	AG(T)	4.56	4.38	4.24	4.14
	GA(T)	0.91	0.88	0.93	1.00
Acetone	**GG(E)**	4.57	4.65	4.51	4.42
	AA(E)	0.00	0.01	0.00	0.00
	GG(T)	5.08	4.95	4.88	4.84
	AG(T)	4.44	4.24	4.13	4.02
	GA(T)	0.91	0.85	0.96	1.01
Chloroform	**GG(E)**	4.43	4.00	4.10	4.01
	AA(E)	0.00	0.00	0.00	0.00
	GG(T)	4.74	4.58	4.51	4.45
	AG(T)	4.01	3.78	3.70	3.58
	GA(T)	0.89	0.84	0.92	0.95
Vacuum	**GG(E)**	3.48	3.29	3.16	3.06
	AA(E)	0.00	0.00	0.00	0.00
	GG(T)	3.85	3.66	3.56	3.47
	AG(T)	3.10	2.91	2.78	2.67
	GA(T)	0.73	0.67	0.72	0.72

Appendix IV *Molecular dipole moments of the low-energy conformers of the isolated MOF linkers in different solvents calculated using PBE/6-311+G(d,p)*

		water	acetone	chloroform	vacuum
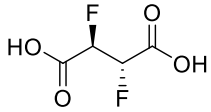	**GG(E)**	0.76	0.81	0.84	3.41
	GG(E)	0.76	0.81	0.83	0.78
	AA(E)	0.00	0.81	0.01	2.88
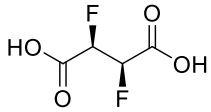	**GA(T)**	4.58	3.74	3.36	2.58
	GG(T)	5.09	4.52	4.40	1.23
	AG(T)	4.49	4.03	3.74	2.86
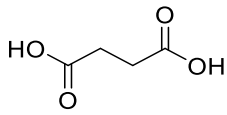	**G**	4.89	4.15	3.96	3.00
	G	3.06	4.14	1.04	0.76
	A	0.00	3.23	2.40	1.95
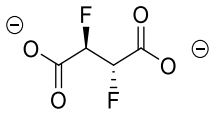	**GG(E)**	11.7	9.52	8.09	7.73
	GG(E)	8.21	6.21	7.67	3.51
	AA(E)	2.04	1.90	0.70	2.42
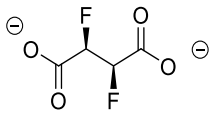	**GA(T)**	10.3	8.14	8.06	-[1]
	GG(T)	7.19	5.03	5.22	3.34
	AG(T)	1.58	1.35	0.72	3.70
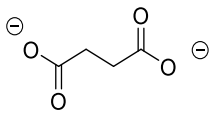	**G**	4.89	12.0	3.96	-
	G	6.50	12.0	5.45	-
	A	0.00	0.29	0.00	2.73
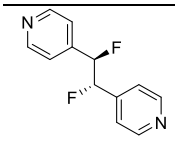	**GG(E)**	4.23	4.00	3.41	2.39
	GG(E)	4.25	4.00	3.42	2.39
	AA(E)	0.00	0.00	0.00	0.00
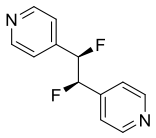	**GA(T)**	4.76	4.56	4.01	2.82
	GG(T)	0.68	0.50	0.40	0.21
	AG(T)	3.92	3.70	3.11	2.08
	G	6.43	6.13	5.44	3.95

[1] Molecular dipole moment is not available because the conformer is not available.

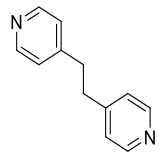	**G**	6.50	6.20	5.45	3.91
	A	0.00	0.02	0.00	0.00

Appendix V *Lattice parameters of the experimentally determined crystal structure, the optimized crystal structure and its various fluorinated analogues*

Cu-MOF Analogue	**Lattice constants (Å)**	**Lattice angles (°)**	**Cell volume (Å^3)**	**Cell density (g.cm^{-3})**
Experimental	a = 25.667(5) b = 13.076(3) c = 8.7250(17)	α = 90.00 β = 95.07 γ = 90.00	2916.80(10)	1.388
Optimized	a = 26.30 b = 13.11 c = 8.678	α = 90.00 β = 95.23 γ = 90.00	2978.75	1.274
B_E	a = 27.88 b = 13.05 c = 8.635	α = 90.00 β = 99.08 γ = 90.00	2961.37	1.363
B_T	a = 26.27 b = 13.09 c = 8.849	α = 90.00 β = 95.56 γ = 89.98	3027.89	1.333
D_E	a = 25.23 b = 13.61 c = 8.684	α = 90.00 β = 93.66 γ = 90.00	2976.09	1.465
D_T	a = 25.87 b = 13.01 c = 9.211	α = 90.00 β = 95.62 γ = 90.00	3083.65	1.386
R	a = 25.36 b = 13.37 c = 8.618	α = 90.00 β = 91.58 γ = 90.00	2920.72	1.463

$D_{n,n+2}$	a = 27.30	α = 90.00	2996.46	1.426
	b = 12.90	β = 97.13		
	c = 8.572	γ = 90.00		

Appendix VI *CO2 uptakes of fluorinated analogues at temperatures of 196 K, 273 K and 298 K*

Analogue	***Uptake at various temperatures (cm^3 g^{-1} STP)***	***Increase/decrease in percentage***
Experimental Cu-MOF	298 K: 12.6	-
	273 K: 26.3	-
	196 K: 70.0	-
Optimized Cu-MOF	298 K: 16.27	-
	273 K: 28.25	-
	196 K: 81.47	-
B_E	298 K: 17.92	9%
	273 K: 31.03	9%
	196 K: 88.77	8%
B_T	298 K: 14.35	-12%
	273 K:24.87	-12%
	196 K: 82.65	1%
D_E	298 K: 18.10	10%
	273 K: 29.45	4%
	196 K: 67.46	-17%
D_T	298 K: 16.11	-1%
	273 K: 25.99	-8%
	196 K: 71.06	-13%
R	298 K: 14.34	-12%
	273 K: 22.46	-20%
	196 K: 62.92	-23%
$D_{n,n+2}$	298 K: 14.14	-13%
	273 K: 24.51	-13%
	196 K: 71.53	-12%

References

1 C. Le Quéré, R. M. Andrew, J. G. Canadell, S. Sitch, J. I. Korsbakken, G. P. Peters, A. C. Manning, T. A. Boden, P. P. Tans, R. A. Houghton, R. F. Keeling, S. Alin, O. D. Andrews, P. Anthoni and L. Barbero, Global Carbon Budget 2016, *Earth Syst. Sci. Data*, 2016, **8133213431**, 605–649.

2 G. T. Feig, W. R. Joubert, A. E. Mudau and P. M. S. Monteiro, South African carbon observations: CO2 measurements for land, atmosphere and ocean, *S. Afr. J. Sci.*, 2017, **113**, 4–4.

3 B. Li, H.-M. Wen, W. Zhou and B. Chen, Porous Metal−Organic Frameworks for Gas Storage and Separation: What, How, and Why?, *J. Phys. Chem. Lett.*, 2014, **5**, 3468–3479.

4 J.-R. Li, R. J. Kuppler and H.-C. Zhou, Selective gas adsorption and separation in metal–organic frameworks, *Chem. Soc. Rev.*, 2009, **38**, 1477.

5 S. Keskin and S. Kızılel, Biomedical Applications of Metal Organic Frameworks, *Ind. Eng. Chem. Res*, 2011, **50**, 1799–1812.

6 A. H. Chughtai, N. Ahmad, H. A. Younus, A. Laypkov and F. Verpoort, Metal–organic frameworks: versatile heterogeneous catalysts for efficient catalytic organic transformations, *Chem. Soc. Rev.*, 2015, **44**, 6804–6849.

7 O. M. Yaghi, H. Li, M. Eddaoudi and M. O'Keeffe, Design and synthesis of an exceptionally stable and highly porous metal-organic framework, *Nature*, 1999, **402**, 276–279.

8 M. Alhamami, H. Doan and C.-H. Cheng, A Review on Breathing Behaviors of Metal-Organic-Frameworks (MOFs) for Gas Adsorption, *Materials (Basel).*, 2014, **7**, 3198–3250.

9 S. Kitagawa, R. Kitaura and S. Noro, Functional Porous Coordination Polymers, *Angew. Chemie Int. Ed.*, 2004, **43**, 2334–2375.

10 M. O'Keeffe and O. M. Yaghi, Deconstructing the Crystal Structures of Metal–Organic Frameworks and Related Materials into Their Underlying Nets, *Chem. Rev.*, 2012, **112**,

675–702.

11 K. D. Vogiatzis, A. Mavrandonakis, W. Klopper and G. E. Froudakis, Ab initio Study of the Interactions between CO_2 and N-Containing Organic Heterocycles, *ChemPhysChem*, 2009, **10**, 374–383.

12 Q. Li, W. Zhang, O. S. Miljanic, C.-H. Sue, Y.-L. Zhao, L. Liu, C. B. Knobler, J. F. Stoddart and O. M. Yaghi, Docking in Metal-Organic Frameworks, *Science*, 2009, **325**, 855–859.

13 R. Vaidhyanathan, S. S. Iremonger, G. K. H. Shimizu, P. G. Boyd, S. Alavi and T. K. Woo, Direct Observation and Quantification of CO2 Binding Within an Amine-Functionalized Nanoporous Solid, *Science*, 2010, **330**, 650–653.

14 J. J. Urban, Computational study of stereoelectronic effects in fluorinated alkylamines, *J. Phys. Org. Chem.*, 2005, **18**, 1061–1071.

15 G. Férey, Microporous Solids: From Organically Templated Inorganic Skeletons to Hybrid Frameworks...Ecumenism in Chemistry, *Chem. Mater*, 2001, **13**, 3084–3098.

16 C. Janiak, Engineering coordination polymers towards applications, *Dalt. Trans.*, 2003, **101**, 2781.

17 V. Hung Nguyen, N. Phuong Thuy Nguyen, T. Tuyet Nhung Nguyen, S. Mendiratta, C.-H. Lee, M. Usman, A. Stroppa, Y. Sun, H.-C. Zhou, J. Jelic, D. Denysenko, D. Volkmer, J.-J. Chen, Y.-T. Chen, D. Senthil Raja, Q. Xu, K. C-W Wu, Y. Yamauchi, C.-T. Huang, K.-T. Liao and C.-H. Lin, Metal-organic frameworks: structure, properties, methods of synthesis and characterization, *Russ. Chem. Rev.*, 2016, **85**, 280–307.

18 M. Wriedt, A. A. Yakovenko, G. J. Halder, A. V. Prosvirin, K. R. Dunbar and H.-C. Zhou, Reversible Switching from Antiferro- to Ferromagnetic Behavior by Solvent-Mediated, Thermally-Induced Phase Transitions in a Trimorphic MOF-Based Magnetic Sponge System, *J. Am. Chem. Soc.*, 2013, **135**, 4040–4050.

19 M. Zhang, Y.-P. Chen, M. Bosch, T. Gentle Iii, K. Wang, D. Feng, Z. U. Wang and H.-C. Zhou, Symmetry-Guided Synthesis of Highly Porous Metal–Organic Frameworks with Fluorite Topology, *Angew. Chemie Int. Ed.*, 2014, **53**, 815 –818.

20 M. Zhang, M. Bosch, T. Gentle Iii and H.-C. Zhou, Rational design of metal–organic frameworks with anticipated porosities and functionalities, *Cryst. Eng. Commun.*, 2014, **16**, 4069–4083.

21 M. Eddaoudi, J. Kim, N. Rosi, D. Vodak, J. Wachter, M. O'Keeffe and O. M. Yaghi, Systematic Design of Pore Size and Functionality in Isoreticular MOFs and Their Application in Methane Storage, *Science*, 2002, **295**, 469–472.

22 Shengqian Ma, Daofeng Sun, Michael Ambrogio, Jacqueline A. Fillinger, and Sean Parkin and Hong-Cai Zhou, Framework-Catenation Isomerism in Metal−Organic Frameworks and Its Impact on Hydrogen Uptake, *J. Am. Chem. Soc.*, 2007, **129**, 1858–1859.

23 I. A. Baburin, V. A. Blatov, L. Carlucci, G. Ciani and D. M. Proserpio, Interpenetrated Three-Dimensional Networks of Hydrogen-Bonded Organic Species: A Systematic Analysis of the Cambridge Structural Database, *Cryst. Growth Des.*, 2008, **8**, 519–539.

24 M. Zhang, Y.-P. Chen, M. Bosch, T. Gentle, K. Wang, D. Feng, Z. U. Wang and H.-C. Zhou, Symmetry-Guided Synthesis of Highly Porous Metal-Organic Frameworks with Fluorite Topology, *Angew. Chemie Int. Ed.*, 2014, **53**, 815–818.

25 G. K. H. Shimizu, Metal–organic frameworks: Model, make, measure, *Nat. Chem.*, 2010, **2**, 909–911.

26 F. Nouar, J. F. Eubank, T. Bousquet, L. Wojtas, M. J. Zaworotko and M. Eddaoudi, Supermolecular Building Blocks (SBBs) for the Design and Synthesis of Highly Porous Metal-Organic Frameworks, *J. Am. Chem. Soc.*, 2008, **130**, 1833–1835.

27 L.-Y. Chou, P. Hu, J. Zhuang, J. V. Morabito, K. C. Ng, Y.-C. Kao, S.-C. Wang, F.-K. Shieh, C.-H. Kuo and C.-K. Tsung, Formation of hollow and mesoporous structures in single-crystalline microcrystals of metal–organic frameworks via double-solvent mediated overgrowth, *Nanoscale*, 2015, **7**, 19408–19412.

28 J.-R. Li, J. Sculley and H.-C. Zhou, Metal-organic frameworks for separations., *Chem. Rev.*, 2012, **112**, 869–932.

29 J.-R. Li, J. Yu, W. Lu, L.-B. Sun, J. Sculley, P. B. Balbuena and H.-C. Zhou, Porous materials with pre-designed single-molecule traps for CO_2 selective adsorption., *Nat. Commun.*, 2013, **4**, 1538.

30 W. Wu, Z. Tian, S. Wang, C. Peng, H. Liu, S. Dai and D. Jiang, Design of Calix-Based Cages for CO_2 Capture, *Ind. Eng. Chem. Res.*, 2017, **56**, 4502–4507.

31 G. H. Clever, S. Tashiro and M. Shionoya, Inclusion of Anionic Guests inside a Molecular Cage with Palladium(II) Centers as Electrostatic Anchors, *Angew. Chemie*, 2009, **121**,

7144–7146.

32 Z. R. Herm, B. M. Wiers, J. A. Mason, J. M. van Baten, M. R. Hudson, P. Zajdel, C. M. Brown, N. Masciocchi, R. Krishna and J. R. Long, Separation of hexane isomers in a metal-organic framework with triangular channels., *Science*, 2013, **340**, 960–4.

33 X. Lin, I. Telepeni, A. J. Blake, A. Dailly, C. M. Brown, J. M. Simmons, M. Zoppi, G. S. Walker, K. M. Thomas, T. J. Mays, P. Hubberstey, N. R. Champness and M. Schröder, High capacity hydrogen adsorption in Cu(II) tetracarboxylate framework materials: the role of pore size, ligand functionalization, and exposed metal sites., *J. Am. Chem. Soc.*, 2009, **131**, 2159–71.

34 J. Park, D. Yuan, K. T. Pham, J.-R. Li, A. Yakovenko and H.-C. Zhou, Reversible alteration of CO2 adsorption upon photochemical or thermal treatment in a metal-organic framework., *J. Am. Chem. Soc.*, 2012, **134**, 99–102.

35 J. Park, J.-R. Li, Y.-P. Chen, J. Yu, A. A. Yakovenko, Z. U. Wang, L.-B. Sun, P. B. Balbuena and H.-C. Zhou, A versatile metal–organic framework for carbon dioxide capture and cooperative catalysis, *Chem. Commun.*, 2012, **48**, 9995.

36 J. Tian, L. V. Saraf, B. Schwenzer, S. M. Taylor, E. K. Brechin, J. Liu, S. J. Dalgarno and P. K. Thallapally, Selective Metal Cation Capture by Soft Anionic Metal–Organic Frameworks via Drastic Single-Crystal-to-Single-Crystal Transformations, *J. Am. Chem. Soc.*, 2012, **134**, 9581–9584.

37 C. R. Murdock, B. C. Hughes, Z. Lu and D. M. Jenkins, Approaches for synthesizing breathing MOFs by exploiting dimensional rigidity, *Coord. Chem. Rev.*, 2014, **258**–**259**, 119–136.

38 C. R. Murdock, N. W. McNutt, D. J. Keffer and D. M. Jenkins, Rotating Phenyl Rings as a Guest-Dependent Switch in Two-Dimensional Metal–Organic Frameworks, *J. Am. Chem. Soc.*, 2014, **136**, 671–678.

39 S. Horike and S. Kitagawa, in *Design of Multifunctional Porous MOFs*, 2011, pp. 3–18.

40 K. Zhang, R. P. Lively, C. Zhang, R. R. Chance, W. J. Koros, D. S. Sholl and S. Nair, Exploring the Framework Hydrophobicity and Flexibility of ZIF-8: From Biofuel Recovery to Hydrocarbon Separations, *J. Phys. Chem. Lett.*, 2013, **4**, 3618–3622.

41 S. Kitagawa and M. Kondo, Functional Micropore Chemistry of Crystalline Metal

Complex-Assembled Compounds, *Bull. Chem. Soc. Jpn.*, 1998, **71**, 1739–1753.

42 S. Kitagawa, R. Kitaura and S. Noro, Functional Porous Coordination Polymers, *Angew. Chemie Int. Ed.*, 2004, **43**, 2334–2375.

43 J. Seo, C. Bonneau, R. Matsuda, M. Takata and S. Kitagawa, Soft Secondary Building Unit: Dynamic Bond Rearrangement on Multinuclear Core of Porous Coordination Polymers in Gas Media, *J. Am. Chem. Soc.*, 2011, **133**, 9005–9013.

44 Z.-J. Lin, J. Lü and M. Hong, Metal–organic frameworks based on flexible ligands (FL-MOFs): structures and applications, *Chem. Soc. Rev.*, 2014, **43**, 5867–5895.

45 E. Coronado, M. Giménez-Marqués and G. Mínguez Espallargas, Combination of Magnetic Susceptibility and Electron Paramagnetic Resonance to Monitor the 1D to 2D Solid State Transformation in Flexible Metal–Organic Frameworks of Co(II) and Zn(II) with 1,4-Bis(triazol-1-ylmethyl)benzene, *Inorg. Chem.*, 2012, **51**, 4403–4410.

46 C. Serre, F. Millange, C. Thouvenot, M. Noguès, G. Marsolier, A. Daniel Louër and G. Férey, Very Large Breathing Effect in the First Nanoporous Chromium(III)-Based Solids: MIL-53 or CrIII(OH)·{O2C−C6H4−CO2}·{HO2C−C6H4−CO2H}x·H2Oy, *J. Am. Chem. Soc.*, 2002, **45**, 13519–13526.

47 S. Bourrelly, P. L. Llewellyn, C. Serre, F. Millange, A. Thierry Loiseau and Gérard Férey, Different Adsorption Behaviors of Methane and Carbon Dioxide in the Isotypic Nanoporous Metal Terephthalates MIL-53 and MIL-47, *J. Am. Chem. Soc.*, 2005, **127**, 13519–13521.

48 T. K. Trung, P. Trens, N. Tanchoux, S. Bourrelly, P. L. Llewellyn, S. Loera-Serna, C. Serre, T. Loiseau, F. Fajula and G. Férey, Hydrocarbon Adsorption in the Flexible Metal Organic Frameworks MIL-53(Al, Cr), *J. Am. Chem. Soc.*, 2008, **130**, 16926–16932.

49 Z. Wang and S. M. Cohen, Modulating Metal−Organic Frameworks To Breathe: A Postsynthetic Covalent Modification Approach, *J. Am. Chem. Soc.*, 2009, **131**, 16675–16677.

50 M. Kim, J. A. Boissonnault, P. V. Dau and S. M. Cohen, Metal-Organic Framework Regioisomers Based on Bifunctional Ligands, *Angew. Chemie Int. Ed.*, 2011, **50**, 12193–12196.

51 S. Henke, A. Schneemann, A. Wütscher and R. A. Fischer, Directing the Breathing Behavior of Pillared-Layered Metal–Organic Frameworks via a Systematic Library of

Functionalized Linkers Bearing Flexible Substituents, *J. Am. Chem. Soc.*, 2012, **134**, 9464–9474.

52 S. Hyun, J. H. Lee, G. Y. Jung, Y. K. Kim, T. K. Kim, S. Jeoung, S. K. Kwak, D. Moon and H. R. Moon, Exploration of Gate-Opening and Breathing Phenomena in a Tailored Flexible Metal–Organic Framework, *Inorg. Chem.*, 2016, **55**, 1920–1925.

53 S. Kitagawa and K. Uemura, Dynamic porous properties of coordination polymers inspired by hydrogen bonds, *Chem. Soc. Rev.*, 2005, **34**, 109.

54 L.-F. Ma, M.-L. Han, J.-H. Qin, L.-Y. Wang and M. Du, Mn II Coordination Polymers Based on Bi-, Tri-, and Tetranuclear and Polymeric Chain Building Units: Crystal Structures and Magnetic Properties, *Inorg. Chem.*, 2012, **51**, 9431–9442.

55 M. Dincă and J. R. Long, Hydrogen Storage in Microporous Metal-Organic Frameworks with Exposed Metal Sites, *Angew. Chemie Int. Ed.*, 2008, **47**, 6766–6779.

56 L. J. Murray, M. Dincă and J. R. Long, Hydrogen storage in metal–organic frameworks, *Chem. Soc. Rev.*, 2009, **38**, 1294.

57 D. M. D'Alessandro, B. Smit and J. R. Long, Carbon Dioxide Capture: Prospects for New Materials, *Angew. Chemie Int. Ed.*, 2010, **49**, 6058–6082.

58 M. P. Suh, H. J. Park, T. K. Prasad and D.-W. Lim, Hydrogen Storage in Metal–Organic Frameworks, *Chem. Rev.*, 2012, **112**, 782–835.

59 J. Sim, H. Yim, N. Ko, S. B. Choi, Y. Oh, H. J. Park, S. Park and J. Kim, Gas adsorption properties of highly porous metal–organic frameworks containing functionalized naphthalene dicarboxylate linkers, *Dalt. Trans.*, 2014, **43**, 18017–18024.

60 H. Li, M. Eddaoudi, T. L. Groy and O. M. Yaghi, Establishing Microporosity in Open Metal-Organic Frameworks: Gas Sorption Isotherms for Zn(BDC) (BDC) 1,4-Benzenedicarboxylate), *J. Am. Chem. Soc.*, 1998, **120**, 8571–8572.

61 J. K. Schnobrich, K. Koh, K. N. Sura and A. J. Matzger, A Framework for Predicting Surface Areas in Microporous Coordination Polymers, *Langmuir*, 2010, **26**, 5808–5814.

62 H. K. Chae, D. Y. Siberio-Pérez, J. Kim, Y. Go, M. Eddaoudi, A. J. Matzger, M. O'Keeffe and O. M. Yaghi, A route to high surface area, porosity and inclusion of large molecules in crystals, *Nature*, 2004, **427**, 523–527.

63 H. Deng, S. Grunder, K. E. Cordova, C. Valente, H. Furukawa, M. Hmadeh, F. Gándara, A.

C. Whalley, Z. Liu, S. Asahina, H. Kazumori, M. O'Keeffe, O. Terasaki, J. F. Stoddart and O. M. Yaghi, Large-pore apertures in a series of metal-organic frameworks., *Science*, 2012, **336**, 1018–23.

64 S. Choi, T. Watanabe, T.-H. Bae, D. S. Sholl and C. W. Jones, Modification of the Mg/DOBDC MOF with Amines to Enhance CO_2 Adsorption from Ultradilute Gases, *J. Phys. Chem. Lett.*, 2012, **3**, 1136–1141.

65 R. Vaidhyanathan, S. S. Iremonger, K. W. Dawson and G. K. H. Shimizu, An amine-functionalized metal organic framework for preferential CO2 adsorption at low pressures, *Chem. Commun.*, 2009, **35**, 5230.

66 S. Yang, J. Sun, A. J. Ramirez-Cuesta, S. K. Callear, W. I. F. David, D. P. Anderson, R. Newby, A. J. Blake, J. E. Parker, C. C. Tang and M. Schröder, Selectivity and direct visualization of carbon dioxide and sulfur dioxide in a decorated porous host, *Nat. Chem.*, 2012, **4**, 887–894.

67 J. An, S. J. Geib and N. L. Rosi, High and selective CO2 uptake in a cobalt adeninate metal-organic framework exhibiting pyrimidine- and amino-decorated pores., *J. Am. Chem. Soc.*, 2010, **132**, 38–9.

68 Z. Chen, S. Xiang, H. D. Arman, J. U. Mondal, P. Li, D. Zhao and B. Chen, Three-dimensional pillar-layered copper(II) metal-organic framework with immobilized functional OH groups on pore surfaces for highly selective CO_2/CH_4 and C_2H_2/CH_4 gas sorption at room tempera, *Inorg. Chem.*, 2011, **50**, 3442–6.

69 B. Zheng, J. Bai, J. Duan, L. Wojtas and M. J. Zaworotko, Enhanced CO_2 binding affinity of a high-uptake rht-type metal-organic framework decorated with acylamide groups., *J. Am. Chem. Soc.*, 2011, **133**, 748–51.

70 M. Lin Foo, S. Horike, T. Fukushima, Y. Hijikata, Y. Kubota, M. Takata, S. Kitagawa, O. M. Yaghi, F. Bonino and K. P. Lillerud, Ligand-based solid solution approach to stabilisation of sulphonic acid groups in porous coordination polymer $Zr_6O_4(OH)_4(BDC)_6$ (UiO-66), *Dalt. Trans.*, 2012, **41**, 13791.

71 H. Furukawa, K. E. Cordova, M. O'Keeffe and O. M. Yaghi, The Chemistry and Applications of Metal-Organic Frameworks, *Science*, 2013, **341**, 1230444–1230444.

72 S. S. Iremonger, R. Vaidhyanathan, R. K. Mah and G. K. H. Shimizu, $Zn_7O_2(RCOO)_{10}$

clusters and nitro aromatic linkers in a porous metal-organic framework., *Inorg. Chem.*, 2013, **52**, 4124–6.

73 Y.-S. Bae, J. Liu, C. E. Wilmer, H. Sun, A. N. Dickey, M. B. Kim, A. I. Benin, R. R. Willis, D. Barpaga, M. D. LeVan and R. Q. Snurr, The effect of pyridine modification of Ni–DOBDC on CO_2 capture under humid conditions, *Chem. Commun.*, 2014, **50**, 3296.

74 P. Chowdhury, C. Bikkina and S. Gumma, Gas Adsorption Properties of the Chromium-Based Metal Organic Framework MIL-101, *J. Phys. Chem. C*, 2009, **113**, 6616–6621.

75 M. Dincă, A. Dailly, Y. Liu, C. M. Brown, D. A. Neumann and J. R. Long, Hydrogen Storage in a Microporous Metal−Organic Framework with Exposed Mn2+ Coordination Sites, *J. Am. Chem. Soc.*, 2006, **128**, 16876–16883.

76 M. Dincă, W. S. Han, Y. Liu, A. Dailly, C. M. Brown and J. R. Long, Observation of Cu2+–H2 Interactions in a Fully Desolvated Sodalite-Type Metal–Organic Framework, *Angew. Chemie Int. Ed.*, 2007, **46**, 1419–1422.

77 V. K. Peterson, Y. Liu, C. M. Brown and C. J. Kepert, Neutron Powder Diffraction Study of D2 Sorption in Cu3(1,3,5-benzenetricarboxylate)2, *J. Am. Chem. Soc.*, 2006, **128**, 15578–15579.

78 D.-S. Zhang, Z. Chang, Y.-F. Li, Z.-Y. Jiang, Z.-H. Xuan, Y.-H. Zhang, J.-R. Li, Q. Chen, T.-L. Hu and X.-H. Bu, Fluorous Metal-Organic Frameworks with Enhanced Stability and High H_2/CO_2 Storage Capacities, *Sci. Rep.*, 2013, **3**, 3312.

79 C. Yang, X. Wang and M. A. Omary, Crystallographic Observation of Dynamic Gas Adsorption Sites and Thermal Expansion in a Breathable Fluorous Metal-Organic Framework, *Angew. Chemie Int. Ed.*, 2009, **48**, 2500–2505.

80 Z. Hulvey, E. H. L. Falcao, J. Eckert and A. K. Cheetham, Enhanced H2 adsorption enthalpy in the low-surface area, partially fluorinated coordination polymer $Zn_5(triazole)_6(tetrafluoroterephthalate)_2(H_2O)_2 \cdot 4H_2O$, *J. Mater. Chem.*, 2009, **19**, 4307.

81 I. T. Horváth, D. P. Curran and J. A. Gladysz, in *Handbook of Fluorous Chemistry*, Wiley-VCH Verlag GmbH & Co. KGaA, Weinheim, FRG, 2005, pp. 1–4.

82 P. T. Nyffeler, S. G. Durón, M. D. Burkart, S. P. Vincent and C.-H. Wong, Selectfluor: Mechanistic Insight and Applications, *Angew. Chemie Int. Ed.*, 2005, **44**, 192–212.

83 M. Pagliaro and R. Ciriminna, New fluorinated functional materials, *J. Mater. Chem.*, 2005,

15, 4981.

84 H.-J. Böhm, D. Banner, S. Bendels, M. Kansy, B. Kuhn, K. Müller, U. Obst-Sander and M. Stahl, Fluorine in Medicinal Chemistry, *ChemBioChem*, 2004, **5**, 637–643.

85 K. Müller, C. Faeh and F. Diederich, Fluorine in Pharmaceuticals: Looking Beyond Intuition, *Science*, 2007, **317**, 1881=1886.

86 D. O'Hagan, R. L. Abel, M. D. Drake, D. J. Fox, A. K. Ignatz, D. M. Kwiat, K. M. Schaal, P. R. Virkler, T. S. Keith, D. O'Hagan, J. Schneider, F. Diederich, M. Kansy and K. Müller, Understanding organofluorine chemistry. An introduction to the C–F bond, *Chem. Soc. Rev.*, 2008, **37**, 308–319.

87 L. Hunter, The C–F bond as a conformational tool in organic and biological chemistry, *Beilstein J. Org. Chem.*, 2010, **6**, 38.

88 C. R. S. Briggs, M. J. Allen, D. O'Hagan, D. J. Tozer, A. M. Z. Slawin, A. E. Goeta and J. A. K. Howard, The observation of a large gauche preference when 2-fluoroethylamine and 2-fluoroethanol become protonated, *Org. Biomol. Chem.*, 2004, **2**, 732.

89 D. O'Hagan, A. Bondi and S. K. Holmgren, Understanding organofluorine chemistry. An introduction to the C–F bond, *Chem. Soc. Rev.*, 2008, **37**, 308–319.

90 K. B. Wiberg, M. A. Murcko, K. E. Laidig and P. J. MacDougall, Origin of the Gauche Effect in substituted ethanes and ethenes, *J. Phys. Chem.*, 1990, **94**, 6956–6959.

91 L. Goodman, A. Hongbing Gu and V. Pophristic, Gauche Effect in 1,2-Difluoroethane. Hyperconjugation, Bent Bonds, Steric Repulsion, *J. Phys. Chem. A*, 2005, **5**, 1223–1229.

92 P. Pachfule, C. Dey, T. Panda, K. Vanka and R. Banerjee, Structural Diversity in Partially Fluorinated Metal Organic Frameworks (F-MOFs) Composed of Divalent Transition Metals, 1,10-Phenanthroline, and Fluorinated Carboxylic Acid, *Cryst. Growth Des.*, 2010, **10**, 1351–1363.

93 M. Jang, T. Yamaguchi, K. Ohara, M. Kawano and M. Fujita, Fluorous Pores in Coordination Networks, *Chem. - An Asian J.*, 2009, **4**, 1524–1526.

94 Q. A. Huchet, B. Kuhn, B. R. Wagner, N. A. Kratochwil, H. Fischer, M. Kansy, D. Zimmerli, E. M. Carreira and K. Mü, Fluorination Patterning: A Study of Structural Motifs That Impact Physicochemical Properties of Relevance to Drug Discovery, *J. Med. Chem.*, 2015, **58**, 9041–9060.

95 Y. P. Rey, L. E. Zimmer, C. Sparr, E.-M. Tanzer, W. B. Schweizer, H. M. Senn, S. Lakhdar and R. Gilmour, Molecular Design Exploiting a Fluorine *gauche* Effect as a Stereoelectronic Trigger, *European J. Org. Chem.*, 2014, **2014**, 1202–1211.

96 S. Kirkpatrick, C. D. Gelatt and M. P. Vecchi, Optimization by Simulated Annealing, *Science*, 1983, **220**, 671–680.

97 J. Pannetier, J. Bassas-Alsina, J. Rodriguez-Carvajal and V. Caignaert, Prediction of crystal structures from crystal chemistry rules by simulated annealing, *Nature*, 1990, **346**, 343–345.

98 J. R. Holden, Z. Du and H. L. Ammon, Prediction of possible crystal structures for C-, H-, N-, O-, and F-containing organic compounds, *J. Comput. Chem.*, 1993, **14**, 422–437.

99 C. Mellot Draznieks, J. M. Newsam, A. M. Gorman, C. M. Freeman and G. Férey, De Novo Prediction of Inorganic Structures Developed through Automated Assembly of Secondary Building Units (AASBU Method), *Angew. Chemie Int. Ed.*, 2000, **39**, 2270–2275.

100 A. Jain, P. Ong, G. Hautier, W. Chen, W. D. Richards, S. Dacek, S. Cholia, D. Gunter, D. Skinner, G. Ceder, K. A. Persson and S. P. Ong, Commentary: The Materials Project: A materials genome approach to accelerating materials innovation, *Cit. APL Mater.*, 2013, **1**, 11002.

101 G. Borboudakis, T. Stergiannakos, M. Frysali, E. Klontzas, I. Tsamardinos and G. E. Froudakis, Chemically intuited, large-scale screening of MOFs by machine learning techniques, *npj Comput. Mater.*, 2017, **3**, 40.

102 T. Düren, F. Millange, G. Férey, A. Krista S. Walton and R. Q. Snurr, Calculating Geometric Surface Areas as a Characterization Tool for Metal−Organic Frameworks, *J. Phys. Chem. C*, 2007, **111**, 15350–15356.

103 A. Shrake and J. A. Rupley, Environment and exposure to solvent of protein atoms. Lysozyme and insulin, *J. Mol. Biol.*, 1973, **79**, 351–371.

104 L. Sarkisov and A. Harrison, Computational structure characterisation tools in application to ordered and disordered porous materials, *Mol. Simul.*, 2011, **37**, 1248–1257.

105 T. F. Willems, C. H. Rycroft, M. Kazi, J. C. Meza and M. Haranczyk, Algorithms and tools for high-throughput geometry-based analysis of crystalline porous materials, *Microporous Mesoporous Mater.*, 2012, **149**, 134–141.

106 M. Fuentes-Cabrera, D. M. Nicholson, B. G. Sumpter and M. Widom, Electronic structure and properties of isoreticular metal-organic frameworks: The case of M-IRMOF1 (M=Zn, Cd, Be, Mg, and Ca), *J. Chem. Phys.*, 2005, **123**, 124713.

107 A. Samanta, T. Furuta and J. Li, Theoretical assessment of the elastic constants and hydrogen storage capacity of some metal-organic framework materials, *J. Chem. Phys.*, 2006, **125**, 084714.

108 A. U. Ortiz, A. Boutin, A. H. Fuchs and F.-X. Coudert, Metal–organic frameworks with wine-rack motif: What determines their flexibility and elastic properties?, *J. Chem. Phys.*, 2013, **138**, 174703.

109 F.-X. Coudert, Responsive Metal–Organic Frameworks and Framework Materials: Under Pressure, Taking the Heat, in the Spotlight, with Friends, *Chem. Mater.*, 2015, **27**, 1905–1916.

110 A. L. Goodwin, D. A. Keen and M. G. Tucker, Large negative linear compressibility of $Ag_3[Co(CN)_6]$., *Proc. Natl. Acad. Sci. U. S. A.*, 2008, **105**, 18708–13.

111 Alain H. Fuchs and A. K. Cheetham, Adsorption of Guest Molecules in Zeolitic Materials: Computational Aspects, *J. Phys. Chem. B*, 2001, **105**, 7375–7383.

112 L. Sarkisov and A. Harrison, Computational structure characterisation tools in application to ordered and disordered porous materials, *Mol. Simul.*, 2011, **37**, 1248–1257.

113 A. L. Myers* and P. A. Monson, Adsorption in Porous Materials at High Pressure: Theory and Experiment, *Langmuir*, 2002, **18**, 10261–10273.

114 A. K. Rappé, C. J. Casewit, K. S. Colwell, W. A. Goddard and W. M. Skiff, UFF, a full periodic table force field for molecular mechanics and molecular dynamics simulations, *J. Am. Chem. Soc.*, 1992, **114**, 10024–10035.

115 S. L. Mayo, B. D. Olafson and W. A. Goddard, DREIDING: a generic force field for molecular simulations, *J. Phys. Chem.*, 1990, **94**, 8897–8909.

116 R. S. Mulliken, Electronic Population Analysis on LCAO–MO Molecular Wave Functions. I, *J. Chem. Phys.*, 1955, **23**, 1833–1840.

117 F. L. Hirshfeld, Bonded-atom fragments for describing molecular charge densities, *Theor. Chim. Acta*, 1977, **44**, 129–138.

118 R. F. W. Bader, *Atoms in molecules : a quantum theory*, Clarendon Press, 1990.

119 M. A. Addicoat, N. Vankova, I. F. Akter and T. Heine, Extension of the Universal Force Field to Metal–Organic Frameworks, *J. Chem. Theory Comput.*, 2014, **10**, 880–891.

120 S. Bureekaew, S. Amirjalayer, M. Tafipolsky, C. Spickermann, T. K. Roy and R. Schmid, MOF-FF - A flexible first-principles derived force field for metal-organic frameworks, *Phys. status solidi*, 2013, **250**, 1128–1141.

121 J. K. Bristow, D. Tiana and A. Walsh, Transferable Force Field for Metal–Organic Frameworks from First-Principles: BTW-FF, *J. Chem. Theory Comput.*, 2014, **10**, 4644–4652.

122 H. Wu, Y. S. Chua, V. Krungleviciute, M. Tyagi, P. Chen, T. Yildirim and W. Zhou, Unusual and Highly Tunable Missing-Linker Defects in Zirconium Metal–Organic Framework UiO-66 and Their Important Effects on Gas Adsorption, *J. Am. Chem. Soc.*, 2013, **135**, 10525–10532.

123 F. Vermoortele, B. Bueken, G. Le Bars, B. Van de Voorde, M. Vandichel, K. Houthoofd, A. Vimont, M. Daturi, M. Waroquier, V. Van Speybroeck, C. Kirschhock and D. E. De Vos, Synthesis Modulation as a Tool To Increase the Catalytic Activity of Metal–Organic Frameworks: The Unique Case of UiO-66(Zr), *J. Am. Chem. Soc.*, 2013, **135**, 11465–11468.

124 C. Chizallet, S. Lazare, D. Bazer-Bachi, F. Bonnier, V. Lecocq, E. Soyer, A.-A. Quoineaud and N. Bats, Catalysis of Transesterification by a Nonfunctionalized Metal−Organic Framework: Acido-Basicity at the External Surface of ZIF-8 Probed by FTIR and *ab Initio* Calculations, *J. Am. Chem. Soc.*, 2010, **132**, 12365–12377.

125 P. Ghosh, Y. J. Colón and R. Q. Snurr, Water adsorption in UiO-66: the importance of defects, *Chem. Commun.*, 2014, **50**, 11329–11331.

126 B. Zheng, M. Sant, P. Demontis and G. B. Suffritti, Force Field for Molecular Dynamics Computations in Flexible ZIF-8 Framework, *J. Phys. Chem. C*, 2012, **116**, 933–938.

127 C. E. Wilmer, K. C. Kim and R. Q. Snurr, An Extended Charge Equilibration Method, *J. Phys. Chem. Lett.*, 2012, **3**, 2506–2511.

128 Y. G. Chung, J. Camp, M. Haranczyk, B. J. Sikora, W. Bury, V. Krungleviciute, T. Yildirim, O. K. Farha, D. S. Sholl and R. Q. Snurr, Computation-Ready, Experimental Metal–Organic Frameworks: A Tool To Enable High-Throughput Screening of Nanoporous Crystals, *Chem. Mater.*, 2014, **26**, 6185–6192.

129 C. J. Cramer, *Essentials of Computational Chemistry: Theories and Models.*, Wiley New York, New York, 2002.

130 W. Koch and M. C. Holthausen, *A Chemist's Guide to Density Functional Theory*, Wiley-VCH Verlag GmbH, Weinheim, FRG, 2001.

131 F. Jensen, *Introduction to Computational Chemistry*, Wiley, 2007, vol. 2.

132 D. B. Cook, *Handbook of computational quantum chemistry*, Dover Publications, Oxford, 2005.

133 D. J. Griffiths, *Introduction to quantum mechanics*, Pearson Prentice Hall, New Jersey, 2005.

134 M. Born and R. Oppenheimer, Zur Quantentheorie der Molekeln, *Ann. Phys.*, 1927, **389**, 457–484.

135 J. Leszczynski, A. Kaczmarek-Kedziera, T. Puzyn, M. G. Papadopoulos, H. Reis and M. K. Shukla, Eds., *Handbook of Computational Chemistry*, Springer International Publishing, Cham, 2017.

136 C. J. Cramer, in *Essentials of Computational Chemistry: Theories and Models*, Second edi., 2004, p. 120.

137 D. J. Griffiths, in *Introduction to quantum mechanics*, New Jersey, 2005, pp. 177–190.

138 C. J. Cramer, in *Essential of Computational Chemistry: Theories and Models*, 2004, pp. 124–126.

139 D. R. Hartree, The Wave Mechanics of an Atom with a Non-Coulomb Central Field. Part I. Theory and Methods, *Math. Proc. Cambridge Philos. Soc.*, 1928, **24**, 89.

140 V. Fock, Näherungsmethode zur Lösung des quantenmechanischen Mehrkörperproblems, *Zeitschrift für Phys.*, 1930, **61**, 126–148.

141 H. Margenau and G. M. Murphy, *The mathematics of physics and chemistry*, Van Nostrand-Reinhold, New Jersey, 1956.

142 R. Barret, M. Berry, T. F. Chan, J. Demmel, J. Donato, J. Dongarra, V. Eijkhout, R. Pozo, C. Romine and H. van der Vonst, *Templates for the Solution of Linear Systems: Building Blocks for Iterative Methods*, Society for Industrial and Applied Mathematics (SIAM, 3600 Market Street, Floor 6, Philadelphia, PA 19104), 1994.

143 A. L. Hickey and C. N. Rowley, Benchmarking quantum chemical methods for the

calculation of molecular dipole moments and polarizabilities., *J. Phys. Chem. A*, 2014, **118**, 3678–87.

144 L. Goerigk and S. Grimme, A thorough benchmark of density functional methods for general main group thermochemistry, kinetics, and noncovalent interactions, *Phys. Chem. Chem. Phys.*, 2011, **13**, 6670.

145 A. Mahmood and R. L. Longo, Structural and relative energy assessments of DFT functionals and the MP2 method to describe the gas phase methylation of nitronates: $[R^1R^2CNO_2]^-$ + CH_3I, *Phys. Chem. Chem. Phys.*, 2016, **18**, 17062–17070.

146 A. P. Scott and L. Radom, Harmonic Vibrational Frequencies: An Evaluation of Hartree-Fock, Møller-Plesset, Quadratic Configuration Interaction, Density Functional Theory, and Semiempirical Scale Factors, *J. Phys. Chem.*, 1996, **100**, 16502–16513.

147 R. a Friesner, Ab initio quantum chemistry: methodology and applications., *Proc. Natl. Acad. Sci. U. S. A.*, 2005, **102**, 6648–6653.

148 C. J. Cramer, in *Essential of Computational Chemistry: Theories and Models*, Wiley, 2010, p. 250.

149 E. Fermi, Un metodo statistico per la determinazione di alcune proprietà dell'atomo, *Rend. Accad. Lincei*, 1927, **6**, 602–607.

150 L. H. Thomas, The calculation of atomic fields, *Math. Proc. Cambridge Philos. Soc.*, 1927, **23**, 542.

151 P. Hohenberg and W. Kohn, Inhomogeneous Electron Gas, *Phys. Rev.*, 1964, **136**, B864–B871.

152 W. Kohn and L. J. Sham, Self-Consistent Equations Including Exchange and Correlation Effects, *Phys. Rev.*, 1965, **140**, A1133–A1138.

153 R. G. Parr and W. Yang, *Density-functional theory of atoms and molecules*, Oxford University Press, 1989.

154 J. P. Perdew and K. Schmidt, in *AIP Conference Proceedings*, AIP, 2001, vol. 577, pp. 1–20.

155 J. P. Perdew, A. Ruzsinszky, J. Tao, V. N. Staroverov, G. E. Scuseria and G. I. Csonka, Prescription for the design and selection of density functional approximations: More constraint satisfaction with fewer fits, *J. Chem. Phys.*, 2005, **123**, 062201.

156 M. . Thorpe and L. Tichý, *Properties and Applications of Amorphous Materials*, Springer Science & Business Media, Illustrated., 2012.

157 L. F. Cabeza, *Advances in thermal energy storage systems : methods and applications*, 2014.

158 V. P. Gupta, *Principles and applications of quantum chemistry*, 2015.

159 J. P. Perdew, K. Burke and M. Ernzerhof, Generalized Gradient Approximation Made Simple, *Phys. Rev. Lett.*, 1996, **77**, 3865–3868.

160 A. D. Becke, Density-functional exchange-energy approximation with correct asymptotic behavior., *Phys. Rev. A, Gen. Phys.*, 1988, **38**, 3098–3100.

161 C. Lee, W. Yang and R. G. Parr, Development of the Colle-Salvetti correlation-energy formula into a functional of the electron density, *Phys. Rev. B*, 1988, **37**, 785–789.

162 J. Tao, J. P. Perdew, V. N. Staroverov and G. E. Scuseria, Climbing the Density Functional Ladder: Nonempirical Meta-Generalized Gradient Approximation Designed for Molecules and Solids, *Phys. Rev. Lett*, 2003, **91**, 146401–146405.

163 W. J. Hehre, R. F. Stewart and J. A. Pople, Self-Consistent Molecular-Orbital Methods. I. Use of Gaussian Expansions of Slater-Type Atomic Orbitals, *J. Chem. Phys.*, 1969, **51**, 2657–2664.

164 M. M. Francl, W. J. Pietro, W. J. Hehre, J. S. Binkley, M. S. Gordon, D. J. DeFrees and J. A. Pople, Self-consistent molecular orbital methods. XXIII. A polarization-type basis set for second-row elements, *J. Chem. Phys.*, 1982, **77**, 3654–3665.

165 Y. M. Galperin, *Introduction to Modern Solid State Physics*, Oslo, 2011.

166 C. Kittel, *Introduction to Solid State Physics EIGHTH EDITION*, John Wiley & Sons, Inc, Berkeley, 7th edn., 1996.

167 J. Ihm, A. Zunger and M. L. Cohen, Momentum-space formalism for the total energy of solids, *J. Phys. C Solid State Phys.*, 1979, **12**, 4409–4422.

168 B. Delley, An all-electron numerical method for solving the local density functional for polyatomic molecules, *J. Chem. Phys.*, 1990, **92**, 508–517.

169 K. Cho, T. A. Arias, J. D. Joannopoulos and P. K. Lam, Wavelets in electronic structure calculations, *Phys. Rev. Lett.*, 1993, **71**, 1808–1811.

170 S. Miertuš, E. Scrocco and J. Tomasi, Electrostatic interaction of a solute with a continuum.

A direct utilizaion of AB initio molecular potentials for the prevision of solvent effects, *Chem. Phys.*, 1981, **55**, 117–129.

171 A. Marenich, C. J. Cramer and D. G. Truhlar, Universal solvation model based on solute electron density and on a continuum model of the solvent defined by the bulk dielectric constant and atomic surface tensions., *J. Phys. Chem. B*, 2009, **113**, 6378–96.

172 T. Ercanli and D. B. Boyd, Evaluation of Computational Chemistry Methods: Crystallographic and Cheminformatics Analysis of Aminothiazole Methoximes, *J. Chem. Inf. Model.*, 2004, **45**, 591–601.

173 S. J. Fox, S. Gourdain, A. Coulthurst, C. Fox, I. Kuprov, J. W. Essex, C.-K. Skylaris and B. Linclau, A Computational Study of Vicinal Fluorination in 2,3-Difluorobutane: Implications for Conformational Control in Alkane Chains, *Chem. - A Eur. J.*, 2015, **21**, 1682–1691.

174 D. J. Frisch, M. J.; Trucks, G. W.; Schlegel, H. B.; Scuseria, G. E.; Robb, M. A.; Cheeseman, J. R.; Scalmani, G.; Barone, V.; Mennucci, B.; Petersson, G. A.; Nakatsuji, H.; Caricato, M.; Li, X.; Hratchian, H. P.; Izmaylov, A. F.; Bloino, J.; Zheng, G.; Sonnenb, 2009.

175 F. Weinhold, C. R. Landis and E. D. Glendening, What is NBO analysis and how is it useful?, *Int. Rev. Phys. Chem.*, 2016, **35**, 399–440.

176 Y. Zhao and D. G. Truhlar, A new local density functional for main-group thermochemistry, transition metal bonding, thermochemical kinetics, and noncovalent interactions, *J. Chem. Phys.*, 2006, **125**, 194101.

177 D. Nazarian, P. Ganesh and D. S. Sholl, Benchmarking density functional theory predictions of framework structures and properties in a chemically diverse test set of metal–organic frameworks, *J. Mater. Chem. A*, 2015, **3**, 22432–22440.

178 C. Reichardt and T. Welton, *Solvents and Solvent Effects in Organic Chemistry*, Wiley-VCH, 2011.

179 Y. Mo, Rotational barriers in alkanes, *Wiley Interdiscip. Rev. Comput. Mol. Sci.*, 2011, **1**, 164–171.

180 D. Radomirovic and I. Kovacic, Deflection and potential energy of linear and nonlinear springs: approximate expressions in terms of generalized coordinates, *Eur. J. Phys.*, 2013,

34, 537–546.

181 K. Manna, T. Zhang, F. X. Greene and W. Lin, Bipyridine- and Phenanthroline-Based Metal–Organic Frameworks for Highly Efficient and Tandem Catalytic Organic Transformations via Directed C–H Activation, *J. Am. Chem. Soc.*, 2015, **137**, 2665–2673.

182 A. Schneemann, V. Bon, I. Schwedler, I. Senkovska, S. Kaskel and R. A. Fischer, Flexible metal–organic frameworks, *Chem. Soc. Rev.*, 2014, **43**, 6062–6096.

183 I. Hong Hwang, J. Mi Bae, W.-S. Kim, Y. Dan Jo, C. Kim, Y. Kim, S.-J. Kim and S. Huh, Bifunctional 3D Cu-MOFs containing glutarates and bipyridyl ligands: selective CO_2 sorption and heterogeneous catalysis, *Dalt. Trans.*, 2012, **41**, 12759.

184 A. K. Cheetham, T. D. Bennett, F.-X. Coudert and A. L. Goodwin, Defects and disorder in metal organic frameworks, *Dalt. Trans.*, 2016, **45**, 4113–4126.

185 R. Smith, I. J. Vitórica-Yrezábal, A. Hill and L. Brammer, Arene guest selectivity and pore flexibility in a metal-organic framework with semi-fluorinated channel walls., *Philos. Trans. A. Math. Phys. Eng. Sci.*, 2017, **375**, 20160031.

186 X. Li, Y.-B. Zhang, M. Shi and P.-Z. Li, (4,4)- and (6,3)-2-D luminescent lanthanide(III) metal-organic frameworks constructed from tetrafluorosuccinate and 1,10-phenanthroline, *Inorg. Chem. Commun.*, 2008, **11**, 869–872.

187 I. Luz, A. Loiudice, D. T. Sun, W. L. Queen and R. Buonsanti, Understanding the Formation Mechanism of Metal Nanocrystal@MOF-74 Hybrids, *Chem. Mater.*, 2016, **28**, 3839–3849.

188 H. Ji, S. Hwang, K. Kim, C. Kim and N. C. Jeong, Direct in Situ Conversion of Metals into Metal−Organic Frameworks: A Strategy for the Rapid Growth of MOF Films on Metal Substrates, *J. Am. Chem. Soc.*, 2016, **8**, 32414–32420.

189 A. Karmakar, L. M. D. R. S. Martins, S. Hazra, M. F. C. Guedes da Silva and A. J. L. Pombeiro, Metal–Organic Frameworks with Pyridyl-Based Isophthalic Acid and Their Catalytic Applications in Microwave Assisted Peroxidative Oxidation of Alcohols and Henry Reaction, *Cryst. Growth Des.*, 2016, **16**, 1837–1849.

190 J. K. Bristow, K. T. Butler, K. L. Svane, J. D. Gale and A. Walsh, Chemical bonding at the metal-organic framework/metal oxide interface: simulated epitaxial growth of MOF-5 on rutile TiO_2, *J. Mater. Chem. A*, 2017, **5**, 6226–6232.

191 E. G. Lewars, in *Computational Chemistry*, Springer Netherlands, Dordrecht, 2011, pp. 9–

43.

192 S. Schlund, R. Müller, C. Graβmann and B. Engels, Conformational analysis of arginine in gas phase—A strategy for scanning the potential energy surface effectively, *J. Comput. Chem.*, 2008, **29**, 407–415.

193 H. Nowell, S. L. Price and IUCr, Validation of a search technique for crystal structure prediction of flexible molecules by application to piracetam, *Acta Crystallogr. Sect. B Struct. Sci.*, 2005, **61**, 558–568.

194 D. Ouyang and S. C. Smith, *Computational Pharmaceutics: Application of Molecular Modeling in Drug Delivery*, John Wiley & Sons, 2015.

195 D. O'Hagan, H. S. Rzepa, M. Schüler and A. M. Slawin, The vicinal difluoro motif: The synthesis and conformation of erythro- and threo- diastereoisomers of 1,2-difluorodiphenylethanes, 2,3-difluorosuccinic acids and their derivatives, *Beilstein J. Org. Chem.*, 2006, **2**, 19.

196 D. P. White, J. C. Anthony and A. O. Oyefeso, Computational Measurement of Steric Effects: the Size of Organic Substituents Computed by Ligand Repulsive Energies, *J. Org. Chem.*, 1999, **64**, 7707–7716.

197 J. Bowser, *Advances in Organometallic Chemistry*, Academic Press, New York, 1994.

198 T. R. Cundari, *Computational Organometallic Chemistry*, CRC Press, New York, 2001.

199 F. Jensen, Describing Anions by Density Functional Theory: Fractional Electron Affinity, *J. Chem. Theory Comput.*, 2010, **6**, 2726–2735.

200 L. R. MacGillivray and C. M. Lukehart, Metal-organic framework materials, *Chem. Soc. Rev.*, 2003, **32**, 276.

201 S. Grimme, Do Special Noncovalent π–π Stacking Interactions Really Exist?, *Angew. Chemie Int. Ed.*, 2008, **47**, 3430–3434.

202 D. O'Hagan, H. S. Rzepa, M. Schüler and A. M. Slawin, The vicinal difluoro motif: The synthesis and conformation of erythro- and threo- diastereoisomers of 1,2-difluorodiphenylethanes, 2,3-difluorosuccinic acids and their derivatives, *Beilstein J. Org. Chem.*, 2006, **2**, 19.

203 A. L. Parrill and K. B. Lipkowitz, in *Reviews in Computational Chemistry*, John Wiley & Sons, 2016.

204 C. Cappelli, S. Corni and J. Tomasi, Solvent Effects on trans/gauche Conformational Equilibria of Substituted Chloroethanes: a Polarizable Continuum Model Study, *J. Phys. Chem. A*, 2001, **105**, 10807–10815.

205 A. U. Ortiz, A. Boutin, A. H. Fuchs and F.-X. Coudert, Anisotropic Elastic Properties of Flexible Metal–Organic Frameworks: How Soft are Soft Porous Crystals?, *Phys. Rev. Lett*, 2012, **109**, 195502.

206 Y. J. Colón and R. Q. Snurr, High-throughput computational screening of metal–organic frameworks, *Chem. Soc. Rev.*, 2014, **43**, 5735–5749.

207 J. Zhang and M. Dolg, ABCluster: the artificial bee colony algorithm for cluster global optimization., *Phys. Chem. Chem. Phys.*, 2015, **17**, 24173–81.

208 D. Karaboga, *An idea based on honey bee swarm for numerical optimization*, 2005.

209 S. Kozuch and J. M. L. Martin, Spin-component-scaled double hybrids: An extensive search for the best fifth-rung functionals blending DFT and perturbation theory, *J. Comput. Chem.*, 2013, **34**, 2327–2344.

210 L. Goerigk, A. Hansen, C. Bauer, S. Ehrlich, A. Najibi and S. Grimme, A look at the density functional theory zoo with the advanced GMTKN55 database for general main group thermochemistry, kinetics and noncovalent interactions., *Phys. Chem. Chem. Phys.*, 2017, **19**, 32184–32215.

211 J. B. Foresman and Ae. Frisch, *Exploring chemistry with electronic structure methods*, 1996.

212 B. Jeziorski, R. Moszynski and K. Szalewicz, Perturbation Theory Approach to Intermolecular Potential Energy Surfaces of van der Waals Complexes, *Chem. Rev.*, 1994, **94**, 1887–1930.

213 S. J. Clark, M. D. Segall, C. J. Pickard, P. J. Hasnip, M. I. J. Probert, K. Refson and M. C. Payne, First principles methods using CASTEP, *Zeitschrift für Krist. - Cryst. Mater.*, 2005, **220**, 567–570.

214 A. Tkatchenko and M. Scheffler, Accurate Molecular Van Der Waals Interactions from Ground-State Electron Density and Free-Atom Reference Data, *Phys. Rev. Lett.*, 2009, **102**, 073005.

215 K. Lejaeghere, V. Van Speybroeck, G. Van Oost and S. Cottenier, Error estimates for solid-

state density-functional theory predictions: an overview by means of the ground-state elemental crystals, *Error Estim. solid-state density-functional theory Predict. an Overv. by means ground-state Elem. Cryst.*, 2012, **39**, 1.

216 T. V. And and P. A. Monson, Monte Carlo Simulation Studies of Heats of Adsorption in Heterogeneous Solids, *Langmuir*, 1996, **12**, 5425–5432.

217 T. J. H. Vlugt, E. García-Pérez, D. Dubbeldam, S. Ban and S. Calero, Computing the Heat of Adsorption using Molecular Simulations: The Effect of Strong Coulombic Interactions, *J. Chem. Theory Comput.*, 2008, **4**, 1107–1118.

218 S. Noro and T. Nakamura, Fluorine-functionalized metal–organic frameworks and porous coordination polymers, *NPG Asia Mater.*, 2017, **9**, e433.

219 I. Kufareva and R. Abagyan, Methods of protein structure comparison., *Methods Mol. Biol.*, 2012, **857**, 231–57.

220 D. Lupyan, *Simulation Interactions Diagram Report*, 2013.

221 C. F. Macrae, P. R. Edgington, P. McCabe, E. Pidcock, G. P. Shields, R. Taylor, M. Towler, J. van de Streek and IUCr, *Mercury* : visualization and analysis of crystal structures, *J. Appl. Crystallogr.*, 2006, **39**, 453–457.

222 D. O'hagan, Y. Wang, M. Skibinski and A. M. Z. Slawin, Influence of the difluoromethylene group (CF2) on the conformation and properties of selected organic compounds*, *Pure Appl. Chem*, 2012, **84**, 1587–1595.

223 S. (Seymour) Lowell, *Characterization of porous solids and powders : surface area, pore size, and density*, Kluwer Academic Publishers, 2004.

224 B. A. Wells, Z. Liang, M. Marshall and A. L. Chaffee, Energy Procedia Modeling Gas Adsorption in Metal Organic Frameworks, *Energy Procedia*, 2008, **1**, 1273–1280.

225 K. Sumida, D. L. Rogow, J. A. Mason, T. M. McDonald, E. D. Bloch, Z. R. Herm, T.-H. Bae and J. R. Long, Carbon Dioxide Capture in Metal–Organic Frameworks, *Chem. Rev.*, 2012, **112**, 724–781.

226 M. Murialdo, N. P. Stadie, C. C. Ahn and B. Fultz, Observation and Investigation of Increasing Isosteric Heat of Adsorption of Ethane on Zeolite-Templated Carbon, *J. Phys. Chem. C*, 2014, **119**, 944–950.

227 W. Rudzinski, S.-L. Lee, C.-C. Sanders Yan and T. Panczyk, A Fractal Approach to

Adsorption on Heterogeneous Solid Surfaces. 1. The Relationship between Geometric and Energetic Surface Heterogeneities, *J. Phys. Chem. A*, 2001, **105**, 10847–10856.

228 N. K. Kanellopoulos, in *Recent Advances in Gas Separation by Microporous Ceramic Membranes*, Elsevier, 2000, pp. 242–244.

229 W. Liang, R. Babarao and D. M. D'Alessandro, Microwave-Assisted Solvothermal Synthesis and Optical Properties of Tagged MIL-140A Metal–Organic Frameworks, *Inorg. Chem.*, 2013, **52**, 12878–12880.

230 Colin D. Wood, Bien Tan, Abbie Trewin, Hongjun Niu, Darren Bradshaw, Matthew J. Rosseinsky, Yaroslav Z. Khimyak, Neil L. Campbell, Ralph Kirk, A. Ev Stöckel and A. I. Cooper, Hydrogen Storage in Microporous Hypercrosslinked Organic Polymer Networks, *Chem. Mater*, 2007, **19**, 2034–2048.

231 C. D. Wood, B. Tan, A. Trewin, F. Su, M. J. Rosseinsky, D. Bradshaw, Y. Sun, L. Zhou and A. I. Cooper, Microporous Organic Polymers for Methane Storage, *Adv. Mater.*, 2008, **20**, 1916–1921.

232 C. Graham, J. Pierrus and R. E. Raab, Measurement of the electric quadrupole moments of CO_2 , CO and N_2, *Mol. Phys.*, 1989, **67**, 939–955.

233 S. J. (Sidney J. Gregg and K. S. W. Sing, *Adsorption, surface area and porosity.*, Academic Press, London, 1967.

234 D. Ongari, P. G. Boyd, S. Barthel, M. Witman, M. Haranczyk and B. Smit, Accurate Characterization of the Pore Volume in Microporous Crystalline Materials, *Langmuir*, 2017, **33**, 14529–14538.

235 N. Mehio, S. Dai and D. Jiang, Quantum Mechanical Basis for Kinetic Diameters of Small Gaseous Molecules, *J. Phys. Chem. A*, 2014, **118**, 1150–1154.

236 D. Vyas, A. Balakrishnan and A. Vyas, The Value of the P Value., *Am. J. Robot. Surg.*, 2015, **2**, 53–56.

237 O. Hübner, A. Glöss, M. Fichtner and K. Wim, On the Interaction of Dihydrogen with Aromatic Systems†, *J. Phys. Chem. A*, 2004, **108**, 3019–3023.

238 E. Ganz, T. Sagara and J. Klassen, Computational study of hydrogen binding by metal-organic framework-5 Computational study of hydrogen binding by metal-organic framework-5 The katoite hydrogarnet Si-free $Ca_3Al_2([OH]_4)_3$: A periodic Hartree-Fock and

B3-LYP study Computational study of hydrogen binding by metal-organic framework-5, *Artic. J. Chem. Phys.*, 2005, **121**, 1005.

239 A. Mavrandonakis and W. Klopper, Comment on “Kinetics and Mechanistic Model for Hydrogen Spillover on Bridged Metal-Organic Frameworks”, *J. Phys. Chem. C*, 2008, **112**, 3152–3154.

240 K. D. Vogiatzis, W. Klopper and J. Friedrich, Non-covalent Interactions of CO_2 with Functional Groups of Metal–Organic Frameworks from a CCSD(T) Scheme Applicable to Large Systems, *J. Chem. Theory Comput.*, 2015, **11**, 1574–1584.

241 S. Nandi, S. Haldar, D. Chakraborty and R. Vaidhyanathan, Strategically designed azolyl-carboxylate MOFs for potential humid CO_2 capture, *J. Mater. Chem. A*, 2017, **5**, 535–543.

242 M. Wahiduzzaman, S. Wang, B. J. Sikora, C. Serre and G. Maurin, Computational structure determination of novel metal–organic frameworks, *Chem. Commun.*, 2018, **54**, 10812–10815.

243 E. Artacho, D. Sánchez-Portal, P. Ordejón, A. García and J. M. Soler, Linear-Scaling ab-initio Calculations for Large and Complex Systems, *Phys. status solidi*, 1999, **215**, 809–817.

244 A. A. Mostofi, P. D. Haynes, C.-K. Skylaris and M. C. Payne, ONETEP: linear-scaling density-functional theory with plane-waves, *Mol. Simul.*, 2007, **33**, 551–555.

245 S. Mohr, L. E. Ratcliff, L. Genovese, D. Caliste, P. Boulanger, S. Goedecker and T. Deutsch, Accurate and efficient linear scaling DFT calculations with universal applicability, *Phys. Chem. Chem. Phys.*, 2015, **17**, 31360–31370.